A Quantitative Assessment of the Performance of a Planar Germanium Detector for PET Imaging

Thesis submitted in accordance with the requirements of the
University of Liverpool for the degree of
Doctor in Philosophy

by

David Christopher Oxley

Oliver Lodge Laboratory

June 2010

To Alison, Tony and Sarah

or

Mum, Dad and the Chief!

If growing up were easy Feivel, would it take so long?

"Papa Mousekewitz", An American Tale, 1987

If you can keep your head, while all around you are losing their's then perhaps you haven't realised the seriousness of the situation.

David Brent, The Office, 2005

Good judgement comes from experience. Experience comes from bad judgment.
Voltaire

Acknowledgements

I would like to formally acknowledge the EPSRC for funding my research. Acknowledgements also to the University of Liverpool Physics Department for supporting it academically. Thanks to the two Heads of Department who have served us all during my stay: Professor Paul Nolan and Professor Ronan McGrath.

Moving slowly into personal thanks I would like to acknowledge my supervisors Dr. Andrew Boston and Prof. Paul Nolan but also Dr. Helen Boston who takes on a supervisory role for all of us in the Nuclear Instrumentation group. I'd like to thank them for their time, effort and patience; for the opportunity, the guidance and support; for the help, comments and discussions, but also drinks and Christmas meals which would make the reformed Ebenezer Scrooge himself think he was a stingy Christmas host.

I want to formally thank all the Nuclear Physics group staff for all of their unofficial efforts with particular mention to Prof. Rodi Herzberg for the mock viva and Dr. Dave Joss for the chat in Costa. A further special mention to the computer support team John Cresswell, Janet Sampson and Mark Norman for their assistance.

Now as I begin to get emotional, thanks to all my family for always supporting me in everything I have ever done. To my Grandparents on both sides (of the Pennines that is) for lunches, dinners and a seemingly endless supply of biscuit tins. Also a special shout to Uncle John for taking me to see the Leeds.

I want to thank my parents, Alison and Tony, and my sister Sarah for everything they have given me in life. Thank you for love, care and support and for providing me with everything I have ever needed (and to be fair a good few things that I just wanted). Out of all these 200 pages, it is the following words that mean the most: thank you and I love you!

Thanks to the second floor, everyone of you. I want to thank the postdoc/student members of the group for their leadership, guidance and support. I would love to say that in darker moments of this whole ordeal I motivated myself by dreaming of Nature publications, 100k salaries, invited talks and BA gold cards - but it would be an utter lie. In times of trouble it was not Mother Mary, but the whole lot of you that kept me going,

whispering words of wisdom like "ll be alright". Whether it was not wanting to let down those who led me, or wanting to appear strong for those in lower years, it was everyone and all of you who kept me strong enough to do this. Thank you!
I want to thank my flatmates Will, Craig, Matt and Marcus. I want thank Matt for the infamous antics and apologise for separating him and his closest friend, but I will have to take the Xbox with me when I leave. Special Danke! to Marcus "The" Scheck for reading this document (all of it!) and for our drunken emotional pep-talks.
I want to give a warm hearted mention to my friends back home: Lutz, Schubbe und Uebi and also Lisa und Marie. Alles Gute fuer die Zukunft an euch alle!
I want to thank Carl Unsworth for his help with the setup and Martin Jones for not punching me during our discussion over Jermaine Beckford's integrity. I want to thank Laura Harkness for Japanese cocktails and making me smile, when I least wanted to. I want to thank Alex Grint for pizzas and films. Time for sitting on a sofa stuffing ourselves with 20 inch pizzas watching Al Pacino shout at people may become limited, nevertheless I promise to find the time again one day - here's to swings and kids, my friend! Thanks to Ren Cooper for teaching me everything in the beginning, thanks to Matt Dimmock for screeching at me whenever I doubted myself. Thanks to Dave "Google" Scraggs for being my wartime consigliere and for keeping our trip to Australia interesting and finally thanks to Lisa for one of the best birthday cakes ever! I am also indebted to Sarah Rigby for acting as somewhat of an agony aunt during the early months of my PhD. Not an easy job I am sure, so thanks! Thanks to my colleagues in the departure lounge Peter, Paul and Andy also to Philippos, Masood, Heidi, Eddie, Jon, Liam, Rob, Liliana, Sam, Fay, John, Anthony and anyone and everyone that I may have forgotten.

Now let's wrap things up with one last quote for you all to go and look up:
"I don't think ever in my life that so many people were so directly responsible for my being so very, very happy."

Abstract

Positron Emission Tomography or PET is a medical imaging tool used in clinical diagnostics, treatment monitoring and developmental drug testing to assess the biological activity of an organ. This study evaluates the abilities of a small animal PET system, which utilises high-purity planar germanium detectors. A Monte-Carlo simulation of the presented apparatus was first experimentally validated, by comparing efficiency measurements across a range of energies (80 keV - 1408 keV). Excellent agreement was demonstrated between the model and the experimental readings. The simulation was then employed to expand image reconstruction techniques, enhancing imaging efficiency by a factor of ten. Individual uncertainties in PET data were systematically introduced to the simulation to quantify their impact on image quality. Particular attention was placed on physical ambiguities e. g. the positron range or the γ-ray acolinearity and distortions introduced by the detector e. g. position resolution or the correct ordering of many interactions. To order these events, a γ-ray tracking routine is presented, which correctly determines the γ-ray sequence in $\sim$80% of its attempts. A selection of increasingly complex phantoms has been modelled to produce achievable, experimental targets for future measurements. The second half of the study further developed pulse shape analysis routines through a high precision characterisation of the position sensitive charge response. A database of these responses was exploited to reduce position resolution down to 1 mm^3 for single site interactions. A mean position error in three dimensions was calculated at 0.78(1) mm. Additionally, this pulse shape database was engaged to quantify the sensitivity of the detector towards multiple interactions within a segment. A method is discussed to recognise interactions separated by 7 mm or more. This technique was implemented on experimental, uncollimated data, where multiple interactions within a segment were identified and deconvolved.

Contents

List of Figures

List of Tables

Chapter 1

Introduction

This thesis focuses on quantifying the impact of *high-purity germanium* (*HPGe*) detectors on the small animal *Positron Emission Tomography* (*PET*) imaging field. In PET, semiconductor detectors have become a very promising alternative to scintillation counters as they offer both competitive spatial and superior energy resolution. This document shall evaluate the potential and limitations of a prototype germanium-based PET system.

1.1 Nuclear Medical Imaging

Functional imaging modalities in nuclear medicine study the well-being of an organ by assessing its biological activity. Functional imaging is often combined with anatomical imaging types such as *Computed Tomography* (*CT*) and *Magnetic Resonance Imaging* (*MRI*), which map physical properties of tissue e. g. density. The majority of clinical nuclear medical imaging comprises two imaging scans: PET and *Single Photon Emission Computed Tomography* (*SPECT*) [Sas07]. Both administer an imaging subject with a radioactive tracer, whose subsequent decay products can be detected to locate the emission point. In PET, scintillation-based detector elements have been most commonly utilised for this purpose. These detectors are conventionally coupled to *PhotoMultiplier Tubes* (*PMT*s) for signal processing. The physical size of the photomultiplier tubes has imposed a limit on the spatial resolution of a detector element, which restricts the image resolution

achievable in a reconstruction. In clinical PET, this limit is ~5 mm [Tar03]. In the drug development research field, there is a need for the ability to acquire functional images of small animals. The ~5 mm image resolution limit is insufficient for small animal imaging and the field has turned to devoted small animal systems and investigating alternative radiation detection devices [Tai05]. One option, currently the focus of much attention and the subject of this work, is to introduce semiconductor detectors to this scenario.

1.2 The SmartPET Project

Semiconductor detectors have historically been employed in the spectroscopic study of the products of exotic nuclei since the 1970s [Lee03]. As a result of advancements in their technology over the last decade, a multitude of research projects have arisen, investigating alternative applications for these devices [Yan01, Wat06, Bos07a, Mih07]. The major reason for this is the high spatial resolution obtainable when combining segmented detectors (Section 3.4.6) with digital electronics (Section 4.2.1) and *Pulse Shape Analysis* (*PSA*, Section 3.4.7) [Krö96, Vet00] routines. The enhanced position resolution allows a high resolution map of a source distribution to be produced. Such capabilities are advantageous in clinical diagnostics and treatment planning/monitoring, but also in any situation where radiation may require localising (e.g. nuclear safety monitoring [Rig06] and international security [Far07]).

SmartPET (*SMall Animal Reconstructed Tomography PET*) [Bos07a] is a prototype, small animal, imaging project which uses segmented, planar, high-purity germanium detectors coupled with digital electronics and pulse shape analysis to acquire PET data. Funded by the Medical Research Council (MRC), the system was a collaborative study in which the University of Liverpool Nuclear Medical Imaging group was to liaise with STFC (then CCLRC) Daresbury, UK. The programme also aimed to demonstrate the principle of collimator-less SPECT imaging. Many publications [Gil06, Mat06, Tur06, Bos07a, Bos07b, Coo07a, Coo07b, Coo08, Coo09] have emanated from this research and proof of principle - in terms of PET imaging - was exhibited for point sources [Mat06]

and distributed sources [Coo09].

1.3 Research Aims

Having developed the necessary software tools [Mat06, Tur06] and successfully achieved some early goals of the project [Coo07b, Coo09], it was important to evaluate the limitations of the system. Experimentally, these had been approached in [Coo07b] when the imaging of a Jaszczak phantom[JAS] (see Section 5.7 for phantom description) was attempted. One of the main difficulties in the measurement of the phantom was the statistical restrictions on the image reconstruction (discussed in Section 5.3.3). Overcoming this issue, is a first aim of this work. Understanding further difficulties in this experiment was another primary objective. Comparing simulated data and experimental measurements opened up an additional route to a reconstructed image, offering further insight into experimentally encountered constraints. This concept was expanded to cover a systematic inclusion of all parameters which influence the quality of a reconstructed image, thus allowing their effects to be studied and quantified in isolation. Furthermore, increasingly complex phantom geometries were simulated, including all distortions on image quality, to establish a realistic target to be reproduced experimentally.
The second half of this thesis aims to expand the analysis of the pulse shapes induced by charge migration (*Pulse Shape Analysis* or *PSA*)and hence improve the position resolution reached with the SmartPET detector. This can be achieved by accurately characterising its position sensitive charge response and generating a look-up table (pulse shape database) to calculate the most likely position of a γ-ray interaction. Additionally, the database shall be applied to identifying and separating multiple γ-ray interactions within one detector element. Therefore, the fundamental research aims in this project are to:

- overcome statistical limitations in imaging by using higher data fractions
- quantify the contributions from individual uncertainties on PET image quality,

- define, in simulation, realistic, experimental imaging targets (phantoms) for future measurements,
- improve position resolution in the SmartPET detector by performing a characterisation analysis and improving the PSA algorithms,
- implement the characterisation results to identify and deconvolve multiple interactions within a detector segment based on the signal response.

Chapter 2

The Physics of Positron Emission Tomography

Positron Emission Tomography (PET) is a diagnostic technique which noninvasively probes the distribution of a radiopharmaceutical within an imaging subject. A positron (e^+) emitting isotope is radiochemically processed to accumulate in the organ of interest where the positrons are released according to the half-life of the nuclide. PET exploits the γ rays resulting from a positron-electron annihilation to reconstruct a spatial and temporal map or *image* of the source distribution. Knowledge of the well-being and activity of the organ is thus inferred [Web98]. This chapter shall discuss the physics of PET along with its role in clinical medicine and, in particular, small animal research.

2.1 Nuclear Medical Imaging

Nuclear medical imaging is a term describing nonintrusive studies of the distribution of a radioactive *tracer* within an organism. Generally, nuclear medicine covers two imaging modalities: PET and SPECT (Single Photon Emission Computed Tomography). Both PET and SPECT share the principle of registering the products of a nuclear decay to obtain the location of a radiopharmaceutical. SPECT isotopes emit a single photon which is conventionally detected using a thallium-doped sodium iodide (NaI(Tl)) *Gamma*

Camera [Ang58]. The Gamma Camera (sometimes referred to as the Anger Camera) relies on a mechanical collimator, mounted to the NaI(Tl) detector, to reliably ascertain the direction of the γ ray. PET studies detect two photons from a positron-electron annihilation (Section 2.4) in coincidence. PET systems are more efficient than SPECT systems as they exploit the coincident detection of both γ rays to bypass the need for mechanical collimation. Figure 2.1 is a schematic illustration of the fundamentals of PET. The positron is emitted from a radioactive nucleus via β^+ decay (Section 2.2) and thermalises in a series of scatter reactions (Section 2.3) before it annihilates with a nearby electron. The produced back-to-back 511 keV photons are detected in radiation sensors, surrounding the imaging subject, to define a line containing the annihilation site. Reconstructing these lines (Section 2.7) produces a spatial map of the distribution of the tracer [Web98]. The physical processes summarised above shall be discussed in further detail in the following sections.

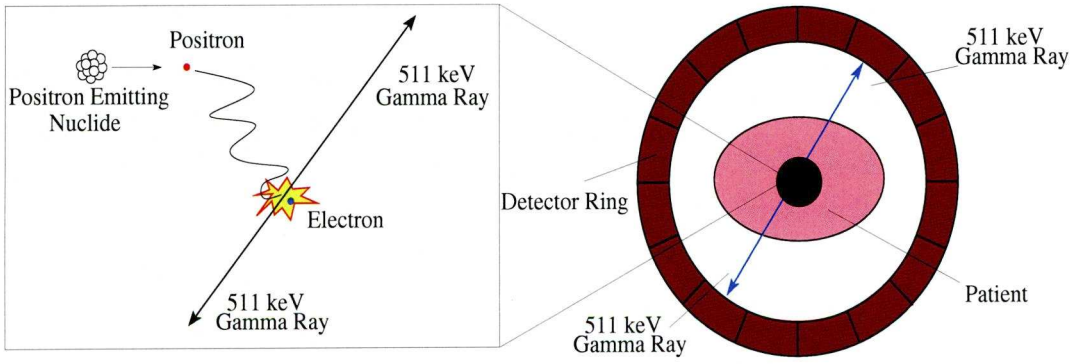

Figure 2.1: A schematic diagram of the physical stages of PET imaging. The positron is emitted from a proton-rich nucleus. After thermalisation, it annihilates with an electron to produce two back-to-back 511 keV photons. Their coincident detection defines a line of response containing the annihilation site.

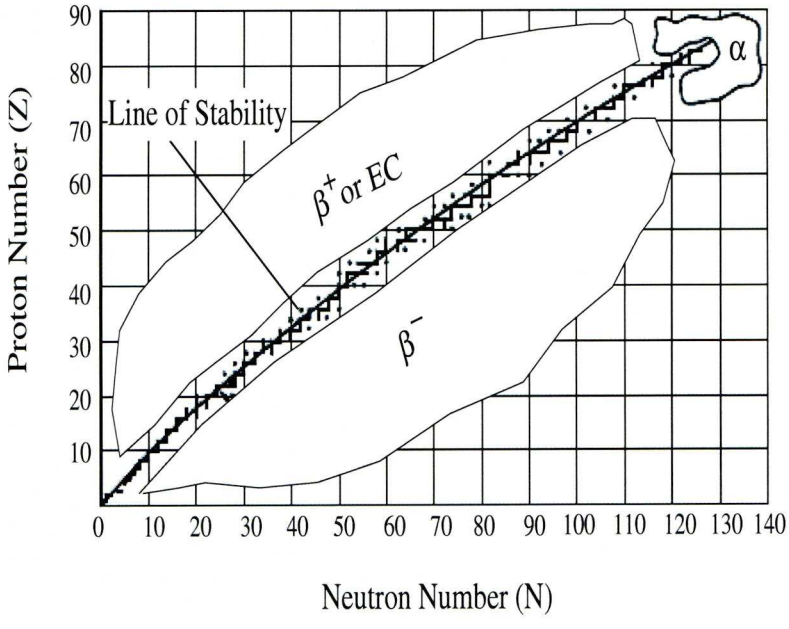

Figure 2.2: An adaptation of the Segre-Chart reproduced from [Doe93]. Stable nuclei are illustrated by solid black squares. Regions of the chart where nuclei are susceptible to β decay are indicated.

2.2 Beta Decay

In nuclei with a large proton/neutron imbalance, β *decay* is a nuclear transition carried by the *weak nuclear force* which optimises the N/Z ratio to bring the nucleus closer to the line of stability [Lil01]. Figure 2.2 is an interpretation of the *Segre-Chart* and displays nuclei as a function of their number of protons (Z) vs. their number of neutrons (N). The regions of the nuclear landscape susceptible to β decay are indicated in the figure as adapted from [Doe93] and [Lil01].

Two variations of β decay exist: β^- and β^+. In β^- decay a neutron (n) is converted into a proton (p), an electron (e^-) and an anti-neutrino($\bar{\nu_e}$); β^+ decay transforms a proton into a neutron, a positron and a neutrino (ν_e). The β^- and β^+ decay processes are described by the Equations (2.1) and (2.2) respectively as given below:

$$n \rightarrow p + e^- + \bar{\nu}_e \tag{2.1}$$

$$p \rightarrow n + e^+ + \nu_e. \tag{2.2}$$

When converting a proton into a neutron, β^+ decay often competes with *Electron Capture (EC)*. In this reaction, a tightly bound electron (most likely from the K-shell) interacts with a proton in the nucleus to produce a neutron and a neutrino. An example of an isotope where these processes compete is ^{22}Na. The decay scheme for this isotope is presented in Figure 2.3. ^{22}Na is frequently used in laboratory research, due to its relatively long half-life ($t_{1/2} \approx 2.5\,y$). Like any other isotopes with a β^+ reaction channel, it can serve as a source of positrons for PET.

The most significant difference between the β-decay modes and α- or γ-decay modes is the continuous range of energies assigned to the light reaction products. It was this observation which first prompted the proposition of the neutrino by Pauli [Pau30]. His hypothesis stated that, if the constant amount of released energy was being shared with

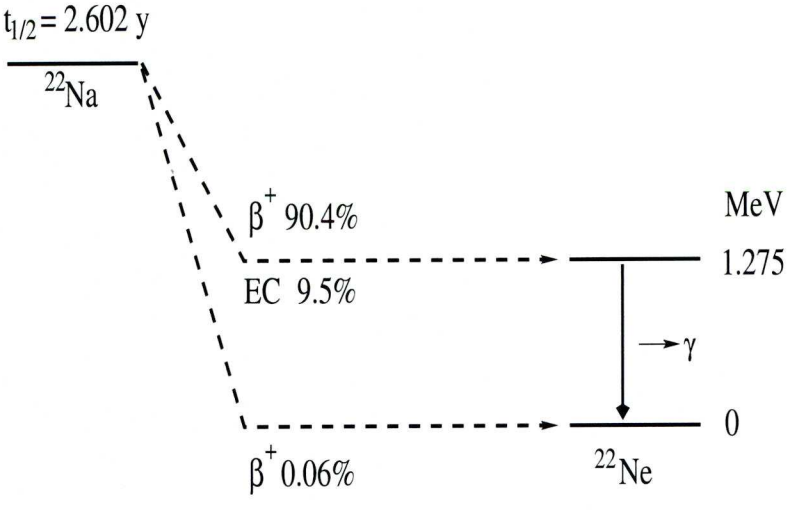

Figure 2.3: The decay scheme for the proton rich ^{22}Na isotope experimentally utilised as a positron source for PET. The competition between the β^+ and EC reaction channels is highlighted.

a second (not counting the nucleus), undetected particle (the neutrino), the continuous range of kinetic energies, in the detected charged particle (e^- / e^+), could be explained. Although it is not the subject of this text to discuss this phenomenon, it is of significance in Section 5.6.2. Figure 2.4 illustrates the energy spectrum of electrons emitted from ^{210}Bi as published in [Eva55]. The continuous range of energies of the charged leptons, along with the asymmetric shape characteristic of β decay, is observed. The shape originates from kinetic energy being shared between the lepton/anti-lepton. The *β end point* (β_{End}) energy corresponds to the maximum available energy being carried by the electron (positron). In this eventuality, the anti-neutrino (neutrino) leaves the reaction with practically zero kinetic energy. The distribution in Figure 2.4 was reproduced in simulation in Section 5.6.2.

2.3 Positron Scattering

Immediately after emission in tissue, the positron has a low probability of annihilating with an electron (2% [Har04]). The most likely process is that of *thermalisation*, in

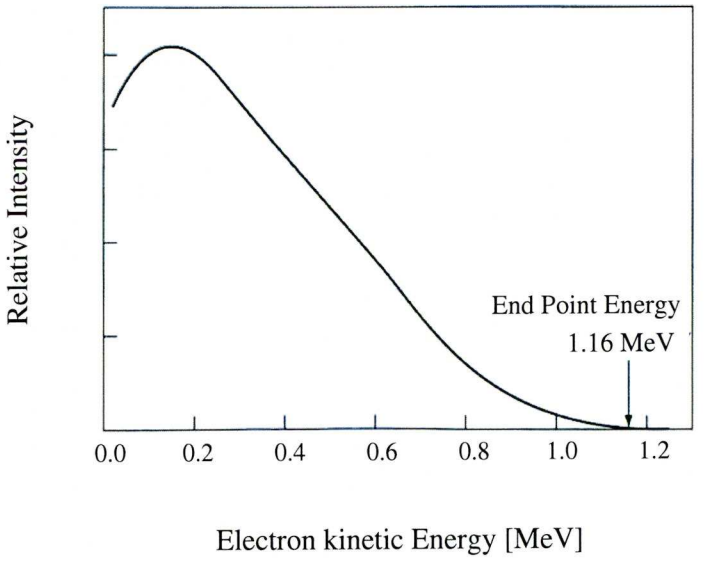

Figure 2.4: An electron energy spectrum resulting from β decay in ^{210}Bi in [Eva55].

which the positron loses kinetic energy through collisions with bound electrons in the molecules/atoms of its environment until it reaches thermal energy. This is analogous to collisions undergone by electrons as they decelerate, however, the procedure is significantly slower for positrons [Har04]. The linear distance travelled by the positron before thermalisation is referred to as the *positron range*. Typical values for this parameter range from tenths of a millimetre to a few millimetres depending on the PET isotope in question. This quantity is a limiting factor in PET imaging, as the acquired data represent the annihilation site rather than the emission point. This shall be studied in detail in Section 5.6.2.

2.4 Positron Annihilation

In many explanations of PET, the positron and electron are considered to *annihilate* instantaneously following the thermalisation of the positron. This simplistic view is not entirely accurate. In fact, there are two strongly competing exit channels: the *direct annihilation* and the *formation of positronium* [Cha01, Har04, Chi07]. According to [Chi08], a direct annihilation occurs in 70% of cases. Positronium is formed in the remaining 30% of annihilations.

2.4.1 Direct Annihilation

Direct positron-electron annihilation may proceed via a number of routes, where emissions of anything 0-4 γ rays have been recorded [Cha01]. The most dominant process emits two γ rays. The cross section of this exit channel was derived in [Dir30] and, for the energy range discussed in this document, can be simplified as

$$\sigma_{2\gamma} = 4\pi r_0^2 c/v, \tag{2.3}$$

where r_0 is the classical radius of the electron, and v is the velocity of the positron relative to an electron, assumed to be stationary. Direct annihilation processes where < 2 γ rays are produced must exchange the unemitted energy with a nucleus. Higher order photon

emission has a much reduced cross section. The cross section for three photon decay ($\sigma_{3\gamma}$) was observed to be a factor of 370 less than $\sigma_{2\gamma}$ in [0re49]. Four photon annihilation is rarer still with an approximate cross section of $1.5\text{x}10^{-6}$ relative to the two photon channel [Ada94].

2.4.2 Positronium Formation

Competing with the direct annihilation is the formation of positronium (Ps). Positronium is a quasi-particle consisting of a positron and an electron [Cha01]. Positronium can exist in a *singlet* state (S=0) or a *triplet* state (S=1). Positronium in the singlet state is referred to as *para-positronium* or *para-Ps* whereas *ortho-positronium* or *ortho-Ps* are conventional terms addressing the S=1 state.

The spin state (S) has large implications for the decay scheme of the positronium. Namely the para-Ps only decays into even numbers of photons, while the ortho-Ps may only decay into odd numbers of photons. The para-Ps are produced in only 25% of positronium formation [Chi08]. The ortho-Ps has a half-life orders of magnitude longer than the para-Ps, with values quoted as 142 ns and 125 ps respectively in [Har04].

2.5 Photon Production

In summary, although multiple decay and annihilation channels exist for the positron/positronium, conventional, clinical PET utilises the two-photon channel to identify a source distribution. From this point on, only the two-photon decay shall be considered as studies of the more complex cases and/or the positronium are more of academic interest than clinical use. In this case, the rest masses of the positron and electron (m_e=511 keV) are converted into energy and carried by two photons[1]. Due to conservation of momentum, the near-zero momentum going into the reaction must be maintained, therefore the γ rays are emitted *back-to-back* at approximately 180° to each other. As the initial momentum was not exactly zero, an angular offset is introduced. This *acolinearity*

[1] In this context, the binding energy of a potential positronium (6.8 eV) shall be neglected.

will impose a fundamental limit on the resolution of a PET image and is quantified by

$$\theta = \sqrt{\frac{E_{\text{kin}}}{m_e c^2}}, \tag{2.4}$$

as a function of kinetic energy (E_{kin}) and mass of the positron and electron (m_e). For the commonly utilised PET isotope ^{18}F, the acolinearity is quoted as 0.47 ° in [Mog95]. The resultant impact on a reconstructed image is quoted as 0.56 mm given a detector separation of 20 cm in [Hal03]. This fundamental limitation may be negligible in comparison to other factors e.g. positron range, aperture resolution depending on the specific isotope and system design.

2.6 Line Of Response Definition

In PET, the patient or imaging subject is surrounded by radiation sensors, to detect the back-to-back photons created by the positron-electron annihilation. The most common designs employ either a ring geometry (see Figure 2.5) or a dual-head geometry (Figure 5.1). Providing both γ rays interact with detector elements within a fixed time window, a *Line Of Response* (*LOR*) can be defined connecting the two interaction points. PET images are reconstructed on the assumption that the annihilation site is a point along the line of response. Intense regions of lines of response overlap and are therefore indicative of concentrated radioisotope distribution. In experimental data, the annihilation site is not necessarily an element of the LOR and they must be categorised into the following groups [Web98]:

2.6.1 True Coincidences

A schematic diagram of a *true coincidence* is depicted in Figure 2.5(a). In this scenario, the two interaction points originate from a common positron-electron annihilation site. The line integral defined by the two points correctly contains the last location of the positron. These LORs need to be maximised for ideal imaging conditions.

2.6.2 Scatter Coincidences

Figure 2.5(b) is a graphic representation of a *scattered LOR*. Although both γ rays originate from the same annihilation site, one γ ray has been deflected from its path by a Compton scatter reaction (Section 3.1.2). The LOR defined by the two interaction points no longer indicates the genuine annihilation site. Unless a correction is applied, a LOR of this nature will introduce artifacts and blurring to the reconstructed image. The fraction of scattered events will depend on the size and density of the imaging subject. Scattered events can be rejected or corrected for based upon the energy deposited by the γ rays and - in clinical imaging - the results of a CT image. Detectors with good energy resolution are an advantage in this case - this shall be discussed further in Section 5.6.3.

2.6.3 Random Coincidences

As displayed in Figure 2.5(c), a *random coincidence* occurs when γ rays from two separate positron-electron annihilations interact in the radiation detectors within the coincidence time window. The LOR defined, connecting the two points, does not contain a genuine interaction site. The rate of random coincidences N_{Random} is described by

$$N_{\text{Random}} = 2\tau N_i N_j, \tag{2.5}$$

where τ is the width of the coincidence timing window and N_i and N_j are rates at which single photons interact in detector element i and j respectively [Web98].

2.7 Image Reconstruction

The aforementioned lines of response are acquired and stored during a PET scan. The process by which these LORs are mathematically transformed into a two- or three-dimensional image is referred to as *image reconstruction*. The techniques for PET image reconstruction have evolved from *Computed Tomography* or *CT* algorithms. In both imaging modalities, the mathematical property of the data representing a projection along a line, l, through

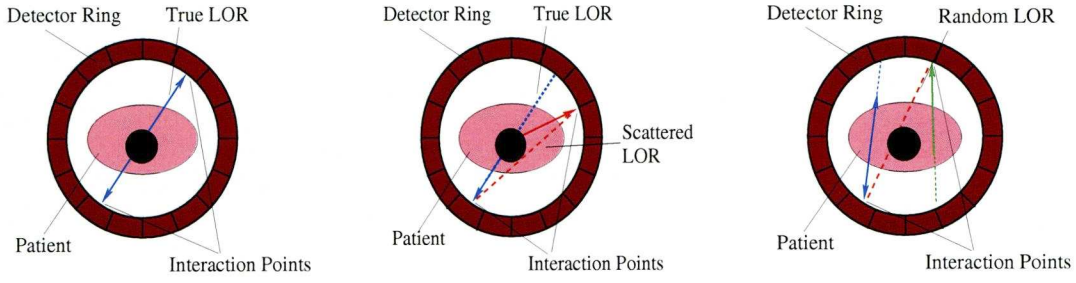

(a) True Coincidence (b) Scatter Coincidence (c) Random Coincidence

Figure 2.5: Three different categories of lines of response: (a) a true coincidence connects the interaction points along a line which contains the annihilation site; (b) in a scattered coincidence at least one γ ray has been deflected from its original path by Compton scattering in the imaging subject; (c) a random coincidence contains two γ rays from independent positron annihilations.

the imaging subject is shared. In CT, the photon source is located outside of the imaging subject, CT is thus known as a *transmission scan.* Transmission scans conventionally image the linear attenuation coefficient as a function of two-dimensional position $\mu(x,y)$. Emission scans, e.g. PET or SPECT, reconstruct the localised activity of a radioisotope $A(x,y)$.

During the scan, a two-dimensional map of activity (i. e. the activity in a slice through the patient) is transformed into a set of line integrals by acquiring lines of response. A complete set of parallel line integrals, spanning the boundaries of the imaging subject, is defined as a *projection.* To regain full, two-dimensional knowledge of the activity map, projections must be acquired for a range of angles [Gas78]: the more angles, the closer the reconstructed activity map $A'(x,y)$ will resemble the true object $A(x,y)$. This relation between several one-dimensional projections and one, two-dimensional, object shall now be discussed mathematically.

When two detector elements a and b register a pair of γ rays produced by a positron-electron annihilation, they define a line of response L_{ab}. Mathematically, the frequency with which L_{ab} is detected in a PET data set is a Poisson value, whose mean $< p_{ab} >$ can

be expressed as

$$< p_{ab} >= \tau_{acq} \int_{FOV} dr f(r) \psi_{ab}(r), \tag{2.6}$$

where $\int_{FOV}$ denotes that projections are acquired across the whole *field of view* (FOV) i. e. the full range of the scanner. In Equation (2.6) τ_{acq} represents the acquisition time and $f(r)$ is a time-independent tracer distribution. $\psi_{\mathrm{ab}}(r)$ is a sensitivity function which corrects for scatter coincidences and random coincidences. For pre-corrected data, this term is unity and Equation 2.6 becomes

$$< p_{ab} >= \tau \int_{L_{ab}} dr f(r) \tag{2.7}$$

along the line L_{ab}. This expression corresponds to the basic mathematical definition of the line integral.

A schematic representation of a slice through a patient is presented in Figure 2.7. A region of increased radiopharmaceutical accumulation is highlighted. Two projections of equally spaced line integrals are displayed in the figure at θ_1 (red) and θ_2 (blue). The frequency of LORs detected in the projections as a function of radial position r ($\mathrm{p}_\theta(r)$) are plotted above the respective projections. If these projections, $p_\theta(r)$, are sampled for a full angular range of $0\,^\circ < \theta < 180\,^\circ$ [2], sufficient information is acquired to reconstruct $A'(x, y)$ from the projection data. The projection data can be stored in a simple list of lines of response, but it is often detailed as a two-dimensional histogram $p(\theta, r)$, a *sinogram*. Figure 2.6(a) displays three point sources of activity each located at different coordinates within $A(x, y)$. The theoretically generated sinogram for this hypothetical object is presented in Figure 2.6(b). Colour was used to relate a point to its sinusoidal function and does not reflect a difference in activity. The figure has been reproduced from [Mat06].

[2] It shall be noted that the angular increments must be equal.

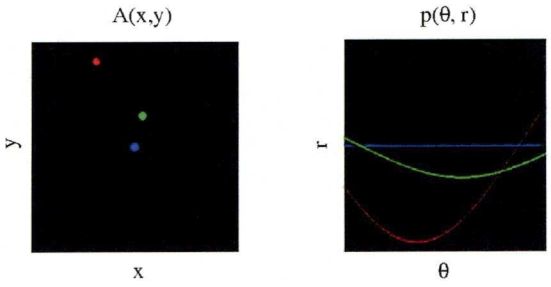

(a) (b)

Figure 2.6: (a) Three point sources of activity in the matrix $A(x, y)$; (b) the corresponding sinogram of $A(x, y)$, $p(\theta, r)$.

The mathematical transformation from a two-dimensional image into a finite number of one-dimensional projections was studied long before tomography was contemplated as a medical tool. [Rad17] derived an equation for this operation referred to as the *Radon Transform*

$$p(\theta, r) = \int_l A(x, y)dl. \tag{2.8}$$

As these line integrals are acquired experimentally in tomographic imaging, the reversal of the Radon Transform is the foundation that many image reconstruction algorithms are based upon. Three approaches to retrieve the two-dimensional map from the array of one-dimensional projections shall be discussed.

2.7.1 Central Slice Theorem

One method of performing the inverse Radon Transform is to apply the *Central Slice Theorem* or *CST* [Bar04]. The theorem relates the two-dimensional Fourier transform of the object $A(x, y)$, $\mathbf{A}(\nu_\mathbf{X}, \nu_\mathbf{Y})$ to the one-dimensional Fourier transform of the sinogram $\mathbf{P}(\nu_\mathbf{\Theta}, \nu_\mathbf{R})$. In the spatial domain, the experimentally acquired sinogram $p(\theta, r)$ is a convolution of the true object $A(x, y)$ and the uncertainties introduced by the system $S(x, y)$

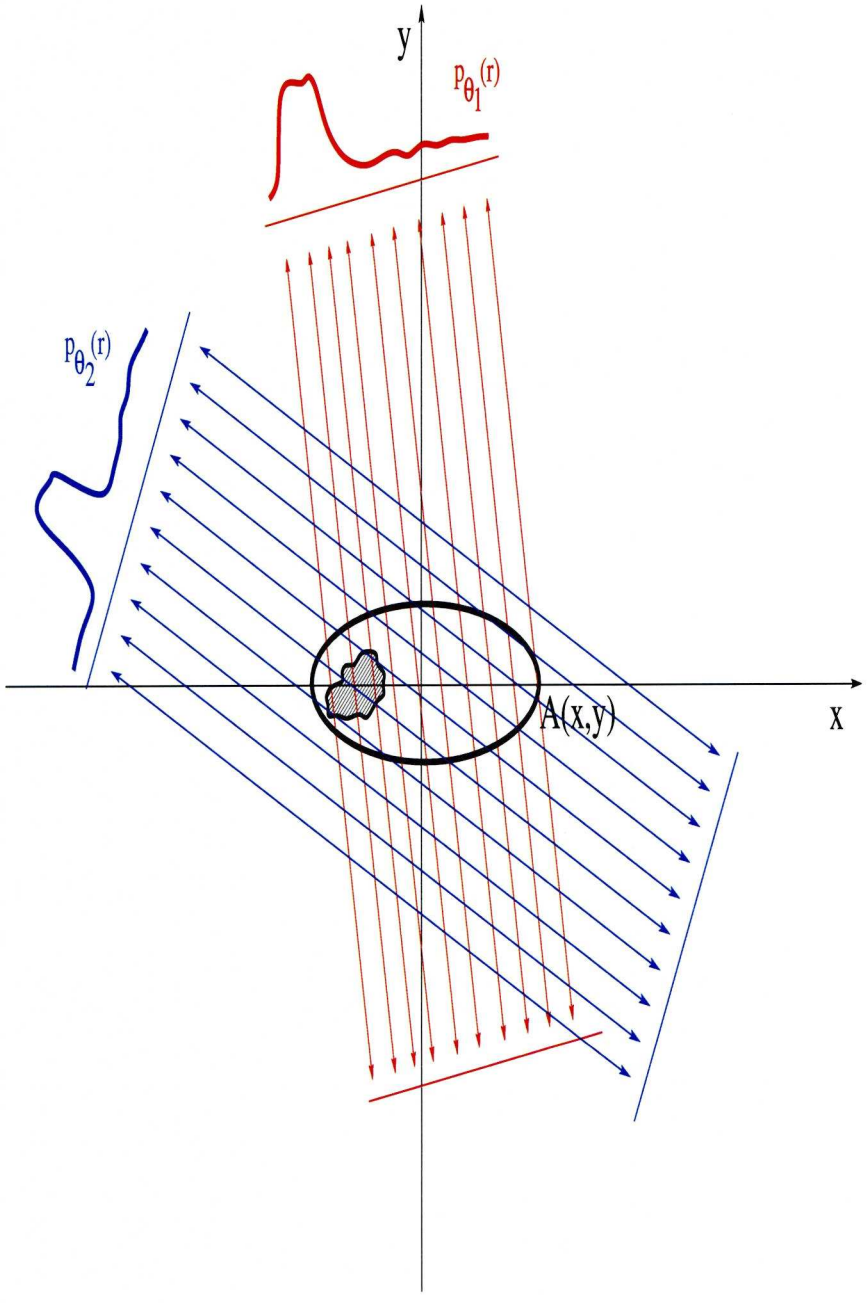

Figure 2.7: A schematic diagram of two sets of line integrals or *projections* acquired at different angles θ_1 (red) and θ_2 (blue). Obtaining such positions at a complete set of angles $0\,^\circ < \theta < 180\,^\circ$ provides sufficient data to reconstruct an image of the object $A(x, y)$.

[3],

$$p(\theta, r) = A(x, y) \otimes S(x, y). \tag{2.9}$$

However, in Fourier space, this deconvolution will be reduced to a multiplication [Ste83] and

$$\mathbf{P}(\nu_{\Theta}, \nu_{\mathbf{R}}) = \mathbf{A}(\nu_{\mathbf{X}}, \nu_{\mathbf{Y}})\ \mathbf{S}(\nu_{\mathbf{X}}, \nu_{\mathbf{Y}}) \tag{2.10}$$

will hold. With detailed understanding of the system response $S(x, y)$, knowledge of the true object $A(x, y)$ can be regained. Direct Fourier reconstruction algorithms operate using this method.

2.7.2 Back Projection

One of the fundamentally simplest means of producing a reconstructed two-dimensional map $A'(x, y)$ is to *back project* the acquired line integrals into *image space.* The straight line r at an angle θ can be expressed in Cartesian coordinates as

$$r = x\cos\theta + \mathrm{y}\sin\theta. \tag{2.11}$$

This allows the sinogram p(θ,r) to be expressed as

$$p(\theta, x\cos\theta + \mathrm{y}\sin\theta) \tag{2.12}$$

and a back projection of p(θ,r)

$$A_{BP}(x, y) = \int_0^{\pi} p(\theta, x\,cos\theta + y\,sin\theta)d\theta \tag{2.13}$$

to be defined.

Due to the nature of producing a point from the overlap of multiple lines, the *simple back projection* function, expressed in Equation (2.13), results in the image being convoluted with a $1/r$ blurring component in the spatial domain. As discussed in Section 2.7.1, convolutions can be removed in the frequency domain. The two-dimensional, inverse Fourier transform of $\mathbf{A}(\nu_{\mathbf{X}}, \nu_{\mathbf{Y}})$ is applied to obtain $A(x, y)$:

[3]Here, the system refers to all sources of error in the data acquisition process (see Chapter 5).

$$A(x,y) = \int_{-\infty}^{\infty}\int_{-\infty}^{\infty} \mathbf{A}(\nu_{\mathbf{X}},\nu_{\mathbf{Y}})\, e^{-j2\pi x\nu_X}\, e^{-j2\pi y\nu_Y} d\nu_X d\nu_Y, \tag{2.14}$$

which can be simplified using Equation 2.9 to

$$A(x,y) = \int_{0}^{2\pi} d\theta \int_{-\infty}^{\infty} \nu_F \mathbf{P}(\nu_{\mathbf{\Theta}},\nu_{\mathbf{R}})\, e^{-j2\pi\nu(x\cos\theta+y\sin\theta)} d\nu, \tag{2.15}$$

the integral over all angles of the one-dimensional, inverse Fourier transform of the projection data (the sinogram). ν_F is the filtering factor to remove the $1/r$ blurring and shall be discussed shortly. Equation 2.15 reduces to

$$A_{FBP}(x,y) = \int_{0}^{\pi} d\theta\, p'(\theta, x\cos\theta + y\sin\theta), \tag{2.16}$$

where $p'(\theta,r)$ is the filtered sinogram. This is the equation describing *filtered back-projection* (*FBP*). Key, here, is that by employing the CST in combination with back-projecting, only one-dimensional, inverse Fourier transforms are handled. This reduces computational time requirements and eases algorithm implementation.

A range of filtering functions can be represented by ν_F. This work utilises a *RAMP filter* defined as

$$\nu_{RAMP} = \frac{|\nu|}{\nu_{Nyquist}}, \tag{2.17}$$

where $\nu_{Nyquist}$ is the *Nyquist frequency* i.e. half the sample rate.

2.7.3 Iterative Reconstruction

Iterative image reconstruction addresses the issue of obtaining the two-dimensional map from a range of its one-dimensional projections from an entirely different perspective. Such algorithms are founded on the principal of making an initial assumption about the activity distribution $A(x,y)$. This assumption is *forward projected* to produce its line integrals $q(\theta,r)$. These are compared with the experimentally measured line integrals, $p(\theta,r)$ to obtain a correction factor, by which the assumption is modified. These steps are referred to as an *iteration* and are repeated until satisfactory convergence between estimated forward projection and acquired LORs is reached. The concept of maximising agreement between

data and estimated image is responsible for the term *Maximum-Likelihood Estimation-Maximisation* or (*ML-EM*), which acts as the basis for many iterative algorithms.
Consider two large data arrays: the first, which represents all possible LORs $i = 1, 2, 3, ...I$, and the second, containing all pixels of image space $j = 1, 2, 3, ...J$. As the radioactive decay process and detection of γ rays remains statistical, the entries inside both arrays are Poisson distributed and oscillate around an equal mean which denotes the true activity $A(x, y)$ [She82]. The i^{th} entry of matrix m, m_{i}, shall define the number of detections in LOR i, while n_j depicts the activity in pixel j. Introducing a value k to delineate the iteration number, then $\{q_i^k\}$ is the forward projection of $\{n_j^k\}$ which is compared with $\{m_i\}$ to calculate $\{n_j^{k+1}\}$. Mathematically the iterative reconstruction algorithm is described by

$$n_j^{k+1} = \frac{n_j^k}{\sum_{i=1}^{I} a_{ij}} \sum_{i=1}^{I} a_{ij} \frac{m_i}{q_i^k} \quad \text{with} \quad \mathrm{q_i^k} = \sum_{\mathrm{j=1}}^{\mathrm{J}} \mathrm{a_{ij} n_j^k}, \tag{2.18}$$

where n_j^k is the reconstructed activity in pixel j after the k^{th} iteration, q_i^k is the expected number of counts in an LOR i, m_i is the experimental measurement collected along LOR i as published in [Rea01]. The quantity a is crucial in this approach and termed the *system matrix*. As the name suggests the system matrix is a mathematical representation of the mechanical system itself and contains the probability of a decay in voxel j being detected along LOR i for all combinations of j and i. The matrix can be simplistic and based solely on geometry (e.g. $a_{ij} = 1$ for $\mathrm{j} \in \mathrm{i}$ and $a_{ij} = 0$ for $\mathrm{j} \notin \mathrm{i}$), but can be expanded with extensive Monte-Carlo simulations to involve such phenomena as the positron range, detector resolution and scattering within both the subject and the detector. Iterative algorithms are very dependant on an agreement between the characteristics of the PET scanner and their reflection in the system matrix [Rea07]. In principle, there is no limit to the detail incorporated in the system matrix and its development and effect on image quality is a very active research field.
Although, generally, the performance of iterative algorithms is superior to analytical methods such as FBP, the iterative algorithm [Mat06] has not been employed in the majority of this work. One reason is the ability of the algorithm to produce very high quality images

and overcome many physical and experimental constraints. However, these constraints are the subject of large sections of this document - removing their effect on image quality would be counter productive. Similar arguments against using an ML-EM algorithm for comparative studies are given in [Lio93]. Logistically, the FBP algorithm [Mat06] (and FBP algorithms in general) is much less computer intensive. The number of reconstructions in this work required a fast reconstruction algorithm. This also influenced the preference of the FBP method.

2.8 Small Animal PET

Nuclear medical imaging is an essential tool in both clinical diagnostics and medical research as it offers an insight to many aspects of a subject's behaviour including transport processes, metabolism, excretion, and signalling between organs [Che01]. Extrapolating a link between humans and animals has also served as a vital route to understanding the causes of, and developing cures for, diseases. For many years, PET has been employed to image large animals e.g. dogs, pigs and non-human primates [Che01]. Until recently, the desire to image *small animals*, e.g. mice, rats etc., has remained unfulfilled as the performance of nuclear medical scanners was unsatisfactory [Web04]. With advancements in detector hardware, these restrictions were surpassed and PET and SPECT systems solely devoted to small animal research studies were designed and constructed. In PET, two of the first such systems were the microPET [Cha99] and the HIDAC-PET camera [Jea99]. Following these systems, many more small animal PET cameras emerged including the Hamamatsu SHR 7700 [Wat97], TierPET [Web99], YAPPET [dGu99] and explore VISTA [Wan06] [4]. Small animal imaging demonstrates several advantages over human imaging in the field of clinical research. Firstly, the non-invasive, non-disruptive and non-destructive technique allows the same test subject to be imaged several times. As there is no need for the subject to be sacrificed after the study, it can act as its own control [Che01]. Therefore a result is much more powerful as variation between subjects is minimised. Furthermore,

[4] For a full review of small animal scanners, the reader is referred to [Lew02, Mye02, Sch03, Web04].

the size and breeding cycle of small animals, such as rodents, helps to reduce costs. As laboratory animals, scientists are also granted the freedom to deliberately infect small animals with certain diseases whereas in human studies the researcher must obviously hope for a suited volunteer. At time of writing it was also ethically permitted to perform genetic modification to these species to produce a subject, tailored to the necessary study e.g. the immunodeficient mouse or nude mouse. These factors have accelerated the pace at which a result can be obtained [Che01] and led to great progress in the field of genetics, pathology, metabolism, oncology and neuroscience [Che01, Lew02, Row03].

2.8.1 Semiconductors in Small Animal PET

With encouraging advances also made in semiconductor detector development in recent years, many research groups have focused their attention to designing a semiconductor-based PET camera. This is a very young research field with the earliest documents published around the turn of the millennium [Cha02, Kas02]. The majority of the semiconductor PET literature concerns itself with either cadmium telluride (CdTe) or Cadmium Zinc Telluride (CZT) e.g. [Ish07]. The high atomic number and density provide the materials with a sufficiently high stopping power to efficiently absorb at 511 keV photons. An alternative is to stack multiple layers of silicon such as was performed in the SiliPET project [dDo06]. This document is devoted to the use of high-purity germanium in PET - the detector of choice in spectroscopic nuclear physics for many decades. A full review of the role of germanium and semiconductors in small animal imaging is provided in Chapter 7 of this document. However, it shall be mentioned here, for completeness that, the superior energy resolution of semiconductors allows more accurate scatter rejections/corrections and simultaneous multimodality PET/SPECT imaging. The ability to operate within a magnetic field is also a great strength of these devices as it allows PET to be coupled to magnetic resonance imaging systems. The literature indicates that semiconductors are playing an increasingly significant role in PET imaging which should not be ignored [Tai05]. The fundamental physics of semiconductor devices are discussed in the following chapter.

Chapter 3

Principles of Radiation Detection

Radiation detection relies on the conversion of energy into a measurable signal, most commonly produced by electric charge. This chapter presents the processes by which this transformation occurs and how spectroscopic information is extracted from the charge response registered in a semiconductor detector. These interactions shall be discussed in the context of High-Purity Germanium (HPGe) detectors. All specific references to energy will assume an interaction in germanium, unless specified otherwise.

3.1 Photon Interactions with Matter

Gamma rays (γ) can interact with matter by several mechanisms. Often a combination of these processes will take place in succession. The likelihood of an electromagnetic interaction occurring is dependent on the energy carried by the γ ray and the atomic number (Z) of the material through which it travels (e.g. $Z = 32$ for germanium). The most common interactions for photons in an energy range of 10 keV - 6 MeV are *photoelectric absorption*, *Compton scattering* and *pair production*. These interactions are displayed schematically in Figure 3.1.

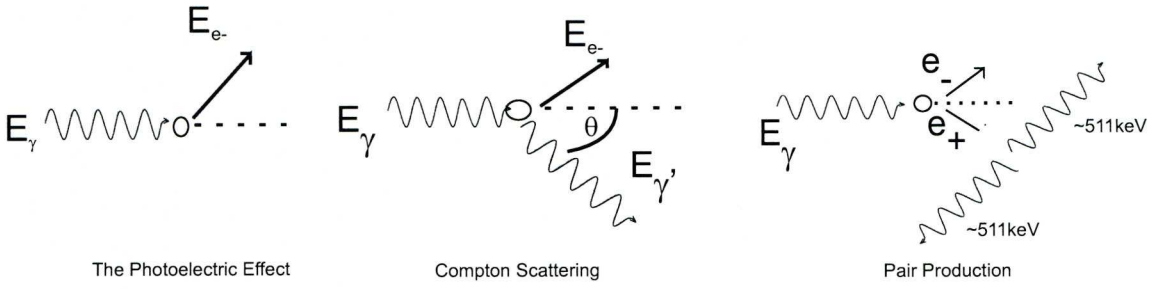

Figure 3.1: Schematic diagrams of the three discussed interactions of γ-radiation with matter. On the left is a diagram of the photoelectric effect, in the centre a representation of Compton scattering while the final figure depicts pair-production.

3.1.1 The Photoelectric Effect

The photoelectric effect, or photoelectric absorption, is the dominant interaction method at low photon energies (10 keV - 200 keV)[Ewa64]. In this process, an incident γ ray transfers its full energy E_γ to an electron tightly bound to an atomic nucleus. The energy deposited provides the electron with kinetic energy (E_e), ejecting it from its shell (most commonly the K shell) leaving a vacancy in its place. The ejected electron is referred to as a *photoelectron*. E_e is defined by

$$E_e = E_\gamma - E_b \tag{3.1}$$

where E_b is the binding energy of the electron. This vacancy will be filled by a bound electron from a higher shell (most commonly the L shell). The difference in energy between the two states is often released as an *X-ray*, however an emission of an *Auger electron* is also possible. The X-ray is characteristic of the energy difference between the shells in the interaction medium. Detection of this X-ray can be utilised for identification purposes in X-ray fluorescence spectroscopy [Jen99].

The probability of photoelectric absorption transpiring has been shown to depend on both the energy of the γ ray and the atomic number (Z) of the absorption medium. Although no equality has been derived for this expression, it can be described by

$$\sigma_{Photoelectric} \sim \frac{Z^n}{E_\gamma^{3.5}} \tag{3.2}$$

where n lies between 4 and 5 [Kno99].

3.1.2 Compton Scattering

Compton scattering dominates for interactions from ~200 keV - ~2 MeV [Ewa64]. In this process, the photon imparts a fraction of its energy to a weakly bound atomic electron. This electron is released as a *recoil electron* or *Compton electron*, while the incident photon continues, scattered from its original direction by an angle θ. The angle θ and the remaining γ-ray energy E'_γ are related by Equation (3.3), where m_0c^2 is 511 $\frac{keV}{c^2}$, the mass of an electron at rest,

$$E'_\gamma = \frac{E_\gamma}{1 + \frac{E_\gamma}{m_0c^2}(1 - cos\theta)}. \tag{3.3}$$

The cross-section of Compton scattering ($\sigma_{Compton}$) occurring is linearly dependent upon the atomic number (Z) of the scattering material due to the number of potential scattering targets increasing with Z [Kno99]. The solid angle distribution $\frac{d\sigma}{d\Omega}$ of scattered γ rays, as a function of energy, is described by the differential Compton scattering cross-section or Klein-Nishina formula [Kle29]

$$\frac{d\sigma}{d\Omega} = Zr_0^2 \left(\frac{1}{1 + \alpha(1 - cos\theta)}\right)^2 \left(\frac{1 + cos^2\theta}{2}\right) \left(1 + \frac{\alpha^2(1 - cos\theta)}{(1 + cos^2\theta)[1 + \alpha(1 - cos\theta)]}\right) \tag{3.4}$$

where $\alpha = E_\gamma \,/\, m_0c^2$ and r_0 is the classical electron radius $2.818 \,\mathrm{x}\, 10^{-15}$ m. The equation assumes γ rays are incident on a single electron.

A graphic representation of this equation at various incident γ-ray energies is depicted in Figure 3.2. The figure presents the angular distribution for a γ ray entering from the

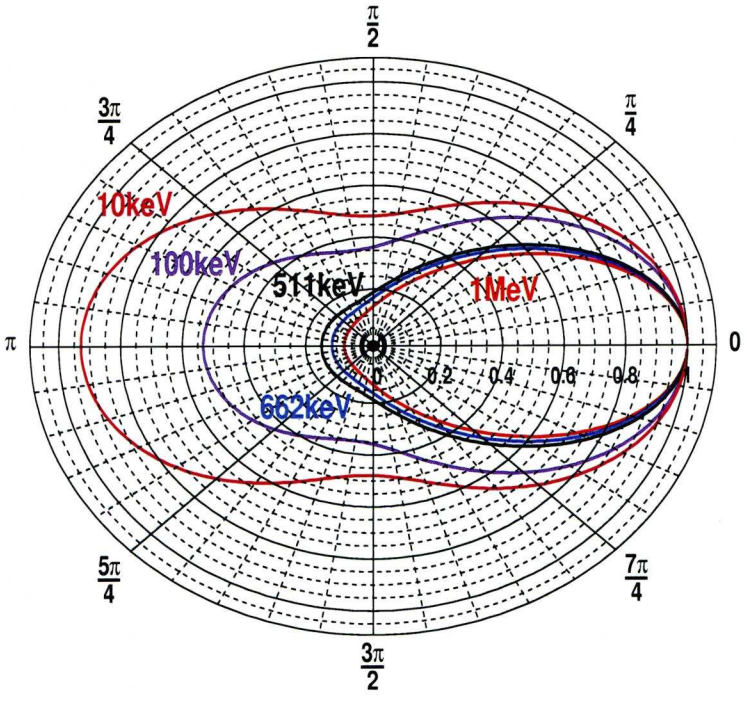

Figure 3.2: A plot of the solid angle distribution of scattered photons for various incident photon energies. The figure illustrates the increased likelihood of forward scattering with higher energies. The figure has been reproduced from [Kle29].

left of the figure and scattering off an electron in the centre. The increased probability of high energy γ rays maintaining their original direction and that of lower energy γ rays scattering more uniformly, is illustrated.

3.1.3 Pair Production

When $E_\gamma > 1.022\,\text{MeV}$ it is possible for the energy of the incident photon to be converted into mass, in the form of an electron (e^-) and positron (e^+) pair. However, the process remains unlikely below 2 MeV. In this mechanism, the incident γ ray is absorbed completely within the Coulomb field of the atomic nucleus, where the charged lepton pair is produced. Energy is conserved according to

$$E_\gamma = T_{e^+} + m_{e^+}c^2 + T_{e^-} + m_{e^-}c^2, \tag{3.5}$$

where T_{e^+} and T_{e^-} are the kinetic energies of the positron and electron respectively, while $m_{e^+}c^2$ and $m_{e^-}c^2$ refer to their respective rest masses. For $E_\gamma = 1.022\,\text{MeV}$, $T_{e^+} + T_{e^-} = 0$. Therefore, 1.022 MeV defines a threshold at which pair production is possible. In this scenario, both the electron and positron are created at rest. If the incident γ ray undergoes pair production in excess of this threshold, the remaining energy is transferred to the electron-positron pair as kinetic energy. After undergoing multiple elastic collisions the kinetic energy of the positron will be reduced to thermal energy. This process is referred to as *thermalisation* (Section 2.3). After thermalisation the positron will annihilate with a nearby electron. The distance travelled before annihilation is referred to as the *positron range*. During the annihilation process, the total energy (kinetic and rest mass) of the e^+ and e^- is attributed to photons sharing the energy available. Most commonly (~80% of annihilations [Kac04, Chi07]) two 511 keV photons are produced. In order to conserve momentum these are released at an angle of 180° to each other as the total momentum going into the reaction is ~0. These photons are referred to as *back-to-back* photons. The scenarios where the annihilation can either result in the emission of more than two photons or non-equally shared momenta at an angle not equal to 180° do exist and were discussed, in further detail, in Section 2.4.

3.1.4 Photon Attenuation

The total photon interaction probability (σ_{total}) is defined as the sum of the probabilities for each individual γ-ray interaction process. For the interactions discussed in the previous sections, this means:

$$\sigma_{Total} = \sigma_{Photoelectric} + \sigma_{Compton} + \sigma_{Pairproduction} \tag{3.6}$$

The probability of an interaction per unit length or the *linear attenuation coefficient* (μ), equates to the product of the number of atoms the γ ray encounters, (N), and σ_{Total}. μ is measured in units of cm^{-1}. For a given material,

$$\mu = N\sigma_{total} = (\frac{N_{Av}\rho}{A})\sigma_{total} \tag{3.7}$$

where N_{Av} is Avogadro's number ($6.022 \times 10^{23} \text{mol}^{-1}$), ρ is the density of the material and A is the atomic mass of the material. μ quantifies the fraction of γ rays which pass through matter of thickness x, unattenuated by an interaction. This exponential relationship is described by

$$\frac{I(x)}{I_0} = e^{-\mu x}, \tag{3.8}$$

where $I(x)$ is the photon intensity after passing through thickness x and I_0 is the initial photon intensity.

3.2 Semiconductor Detectors

Solid state detectors are of interest for nuclear [Del99], astrophysical [Bog00] and medical [Vet04] applications. Being several orders of magnitude denser than their gas based counterparts, they have higher stopping powers and thus higher efficiencies. Solid state detectors can be separated into two categories: scintillators and semiconductors. Scintillators operate via the conversion of energy into light, which is subsequently processed into an electric signal most commonly via a PhotoMultiplier Tube (PMT). In a semiconductor, charge carriers are created, whose migration through an electric field produces a time and position dependent electric signal (Section 3.3.3). Due to their superior energy resolution (Section 3.4.1), semiconductors are utilised in measurements where high spectroscopic precision is necessary. The ability to manufacture these devices in large volumes allows high fractions of solid angle coverage, making semiconductors one of the standard detector types in both nuclear and particle physics experiments. Great advancements have been made in semiconductor development in recent years [Lee03], increasing their availability for physics applications. Firstly, the ability to divide semiconductors into multiple zones by *segmentation* of either one, or both, of the charge collecting electrodes (or *contacts*) has improved position resolution without significantly compromising a detector's active area. This improved position resolution has allowed more precise spectroscopic studies in nuclear physics [Sim06] and also lead to investigations into the feasibility of semiconduc-

tors in medical physics [Bos07a]. Furthermore, the coupling of multiple detector readout channels to fast digital electronics has enabled the extraction of time dependent charge signals which allow enhancement of position resolution beyond the granularity of the segments [Krö96, Vet00]. Following one, or several, of the γ-ray interactions discussed above, the resultant charge carriers are exploited to obtain an electrical signal. The details of these steps shall be discussed within the following section.

3.2.1 Solid State Materials

Electric conduction is the migration of electrons through a material. This occurs when an electron is promoted from the *valence band* (E_V) into the *conduction band* (E_C). The vacancy created by the electron's absence is referred to as a *hole* (h). It is the separation between these two bands or *band gap* (E_g), which defines the ease with which electrons are promoted and charge is conducted. Based upon their ability to conduct (electric conductivity, σ) or their resistivity ($\rho = 1/\sigma$), solid state materials are categorised into three groups: *conductors*, *insulators* and *semiconductors* [Par04]. The magnitude of E_g, in combination with the extent to which the two bands are occupied by electrons and holes, defines a material's conductivity. In a conductor, two scenarios exist: firstly the conduction band and valence band can lie sufficiently close in energy that E_g can be bridged by electrons with thermal energies. This also requires a partial occupancy in both bands allowing charge to migrate to vacant energy levels. A second possibility is for the the two bands to overlap. In both situations, the charge flows naturally as the movement of charge through bands occurs easily, resulting in an electric current.

In an insulator, the valence band is fully occupied while the conduction band is empty. The two bands are typically separated by E_g $\sim$9 eV [Sze02]. This large energy gap prevents charge flow between bands, prohibiting the material from conducting electrons. A semiconductor can be considered an intermediate stage between an insulator and a conductor. In a semiconductor, E_g $\sim$1 eV at room temperature and only a small fraction of thermal electrons will have sufficient energy to bridge the band gap, while a thermal or electromagnetic energy deposit provides sufficient energy to excite an electron into the

conduction band and produce a current [Par04]. It is this property which allows a semiconductor to function well as a radiation sensor. This thesis will focus on semiconductors fabricated from members of the fourth chemical element group (Group IV). In solid state physics, these are crystallographic structures built of four-valent atoms.

3.2.2 Doping

So far, conduction has been considered as the promotion of N electrons to the conduction band and the creation of N vacancies or *holes* in the valence band. Therefore, the number of charge carriers of each polarity will equate according to

$$n = p = n_i, \tag{3.9}$$

where n is the number of electrons per unit volume, p is the number of holes per unit volume and n_i is referred to as the *intrinsic charge carrier concentration.* In a semiconductor device, this scenario is not necessarily desirable as one may choose to have a semiconductor where either the hole current or electron current dominates. For this purpose, the crystal lattice can be *doped* with *impurities* to control the charge carrier concentration. Dopants are added by introducing atoms from Group III or Group V into the crystallographic structure [Sze02, Par04]. An impurity atom introduced from Group III (*acceptor*) will add a hole to the valence band, as its tetravalent electron shell structure is not able to bind with all four electrons in the crystal. Contrary to the excitation of an electron into the conduction band, a hole has been created without producing an electron. When a Group-V atom (*donor*) is introduced, an additional electron is made available in the conduction band without generating a hole in the valence band. Semiconductors which have been doped with Group-III elements to increase hole concentration are referred to as *p-type* crystals. The reverse case are *n-type* crystals. When a semiconductor is doped, Equation (3.9) is invalidated and the semiconductor is referred to as an *extrinsic* semiconductor [1]. The carrier concentration must now be described by

$$n \,\mathrm{x}\, \mathrm{p} = \mathrm{n_i^2}. \tag{3.10}$$

[1] A semiconductor which has not had dopants introduced is termed an *intrinsic* semiconductor.

These additional holes or electrons provide an energy band close to the valence or conduction bands respectively, permitting occupancy within the band gap E_g. It can be assumed that all introduced dopants will be fully ionised as sufficient thermal energy exists within the crystal for this to occur. Therefore, the number of charge carriers can be described by the approximations

$$n \simeq N_D \tag{3.11}$$

and

$$p \simeq N_A \tag{3.12}$$

where N_D is the donor concentration and N_A is the acceptor concentration. A schematic diagram of the semiconductors energy levels is given in Figure 3.3(a).

3.2.3 P-N junction

When a p-type semiconductor is placed in good thermodynamic contact with an n-type semiconductor, the two regions of different dopant type interact as displayed schematically in Figure 3.3(b). The steep charge concentration gradients exert a force on the respective charge carriers. Analogous to a high pressure gas in an open space, the charge carriers will diffuse into regions of weaker concentration. The force responsible for this is therefore entitled the *diffusion force* (F_{diff}) [Par04]. F_{diff} will force the electrons towards the p-type region and the holes towards the n-type region of the semiconductor. As the acceptors (N_A^-) and donors (N_D^+) are a fixed part of the crystal lattice, they remain stationary while the hole or electron which they introduced is free to diffuse.

The stationary acceptors and donors form regions of opposing charge within both the p- and n-type regions. Both zones now consist of a region of neutral charge and a region, close to the junction, where the net charge is non-zero (*space-charge*). This process of charge diffusion and the subsequent accumulation of space-charge on a microscopic level are illustrated schematically in Figure 3.4.

The space-charge regions form the *depletion region* of the semiconductor as it is close to free of mobile charge carriers. Inside the depletion region, the unbalanced ions produce an electric potential (*built-in potential* (V_0)), resulting in an electric field between the two

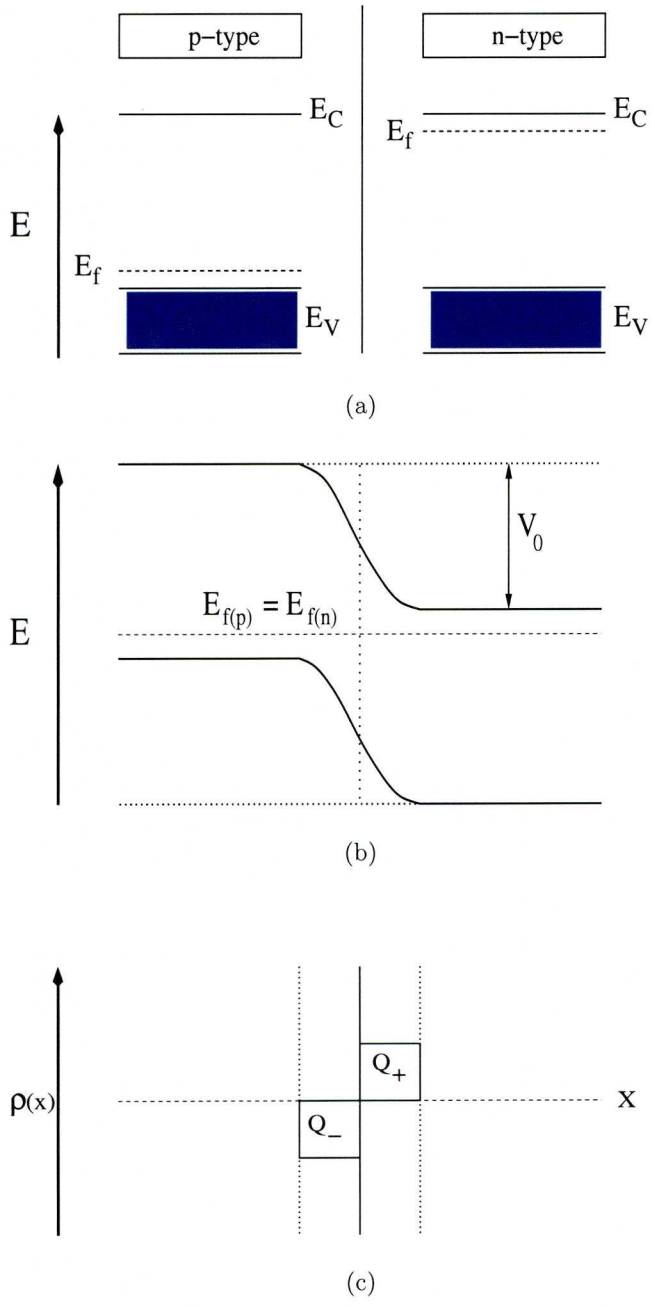

Figure 3.3: The figures above are schematic diagrams of the three key stages in constructing a p-n junction. Figure 3.3(a) shows the two oppositely doped regions separated from each other. E_f is the level of the Fermi energy. Figure 3.3(b) illustrates the two regions in thermodynamic contact and the merging of the two Fermi energies. Figure 3.3(c) represents the subsequent build-up of space-charge.

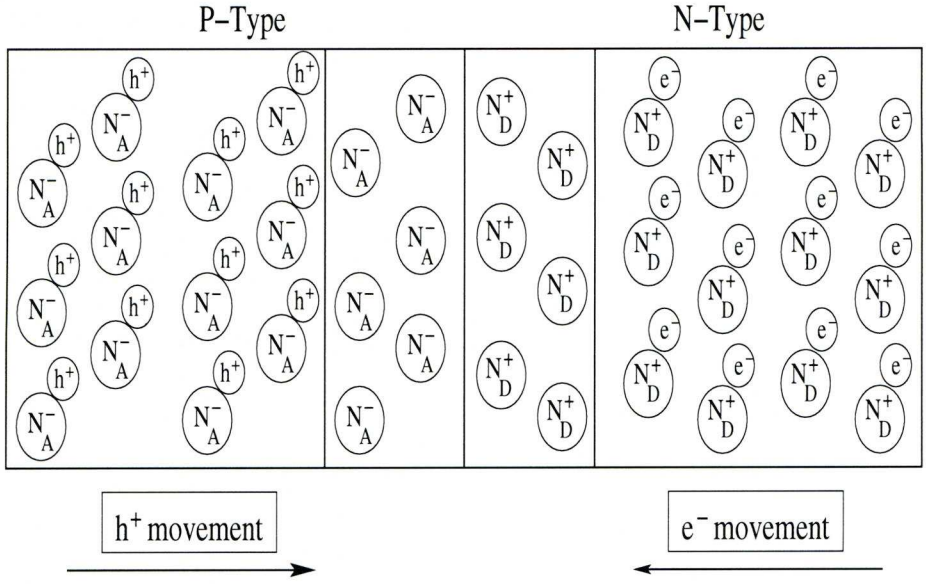

Figure 3.4: An illustration of how the charge is spread throughout a junction between p- and n-type regions of dopant concentration. The outer regions remain charge neutral yet positive space-charge accumulates within the n-type region due to the migration of holes. The reverse scenario is true for the p-type region.

regions of opposing polarity. The electric field exerts an additional force, the *drift force* (F_{drift}) on the charge carriers, opposing F_{diff} described by

$$F_{drift} = qE, \tag{3.13}$$

where q is the charge of either a hole or electron and E is the magnitude of the electric field. With time, a state of charge carrier equilibrium is reached where the two forces F_{diff} and F_{drift} are in balance. The net current flow (J_{total}) within the depletion region must remain zero, however, both the drift current (J_{drift}) and the diffusion current (J_{diff}) are non-zero.

$$J_{total} = 0 \tag{3.14}$$

$$J_{total} = J_{drift} + J_{diff}. \tag{3.15}$$

In order to further understand the depletion region, the simplification of a one dimensional case shall be made. The width of the depletion region or *depletion width* (W_d) is defined

by

$$W_d = x_p + x_n, \tag{3.16}$$

where x_p is the width of the p^+ region and x_n is the width of the n^- region. Throughout this depletion region, overall charge neutrality must hold, as each electron results from the ionisation of an atom and the creation of a hole. Therefore the total number of charge carriers on either side of the p-n junction must equate:

$$N_A x_p = N_D x_n. \tag{3.17}$$

Although the boundaries of the depletion region are not abrupt, their width is negligible in comparison to the depletion width W_d [Par04]. This allows the definition of boundary conditions in order to solve Poisson's equation in a one dimensional case,

$$\frac{d^2V}{dx^2} = -\frac{\rho(x)}{\epsilon}, \tag{3.18}$$

where $\rho(x)$ is the charge density as a function of x-dimensional position and $\epsilon = \epsilon_0\epsilon_r$ is the dielectric constant for the material in question. Solving Equation (3.18) produces

$$\frac{d^2V}{dx^2} = +\frac{qN_A}{\epsilon} \quad \text{for} \quad -\mathrm{x_p} \leq \mathrm{x} \leq 0 \tag{3.19}$$

for the p-type region and

$$\frac{d^2V}{dx^2} = -\frac{qN_D}{\epsilon} \quad \text{for} \quad 0 \leq \mathrm{x} \leq \mathrm{x_n} \tag{3.20}$$

for the n-type region. For a p-n junction to operate as a γ-ray detector, it is necessary for W_d to extend across the full volume of the crystal [Par04]. This is achieved by applying an external potential bias across the junction, introducing an additional electric field. This electric field can either hinder (reverse bias) or facilitate (forward bias) drift current flow (J_{drift}). Figure 3.5 illustrates the current flow as a function of applied voltage. The electric field generated by the bias will sum with the already existing field(s) produced by space-charge. The reverse bias will intensify F_{diff} drawing more charge carriers from

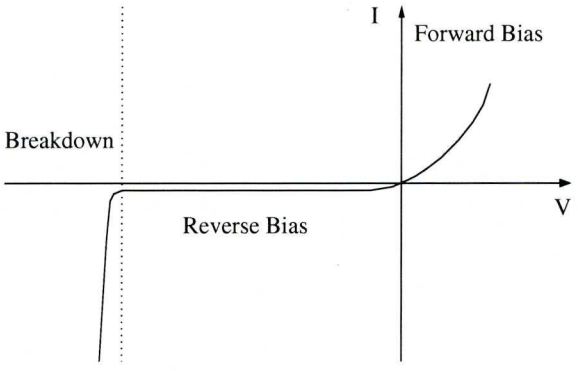

Figure 3.5: The figure illustrates the relationship between current flow and applied bias voltage across the p-n junction.

the neutral regions of the doped crystal into regions of space-charge, hence widening the depletion region.

The depletion width (W_d) is calculated by

$$W_d = \sqrt{\frac{2\epsilon(V_0 - V)}{q}(\frac{N_A + N_D}{N_A N_D})}, \tag{3.21}$$

where ϵ is the dielectric constant and V_0 is the built in potential.

In semiconductor applications, the voltage at which the depletion width extends across all of the crystal is referred to as the *depletion voltage*. For a p-n junction to function as a radiation sensitive device, bias is applied above the depletion voltage to the *operation voltage*.

Both the depletion and operation voltage will depend on crystal geometry. The operation voltage can surpass the depletion voltage by several 100 to 1000 Volts. This additional bias voltage is applied for a multitude of reasons. It ensures the drift velocity of the charge carriers (Section 3.3.4) is saturated and maintains a strong, uniform electric field in all regions of the detector. The strong electric field also reduces the risk of charge carrier recombination (Section 3.3.2), maximising charge collection efficiency.

3.3 High Purity Germanium Detectors

Due to its inherent chemical properties discussed in this section, germanium crystals function well as a radiation detector. The steps leading to the readout of an electric signal shall also be covered herein.

3.3.1 Physical Properties of Germanium

Germanium is an element from the fourth group (Group IV) of the periodic table with an atomic number (Z) of 32. Germanium's density ($5.323\,\mathrm{g/cm^3}$) and atomic weight ($72.64\,\mathrm{g/mol}$) are responsible for its reasonable stopping power and efficiency as a γ-ray detector. In comparison to other detector types, germanium, as a semiconductor, finds its place in an intermediate stage between inefficient gas detectors and highly efficient scintillators. However, semiconductors provide superior energy resolution to both gas detectors and scintillation counters, due to the ease of charge liberation and direct charge collection attributed to their low band gap and conducting properties. Germanium, especially, is the unrivalled material of choice for the spectroscopic measurement of γ rays. Various physical and chemical properties are quoted in Table 3.1. Germanium has a Face Centred Cubic (FCC) lattice crystal structure. This means that germanium atoms are arranged in a cubic base with an additional germanium atom positioned at the centre of the six faces. Therefore, the continuously repeated unit cell contains four atoms. The FCC structure is displayed schematically in Figure 3.6(a), while Figures 3.6(b), 3.6(c) and 3.6(d) illustrate the various lattice planes and their *Miller* indices quoted below. When discussing semiconductor materials, it is of interest to examine the conduction and valence band (E_C and E_V) structure. A schematic diagram of germanium's band structure is given in Figure 3.7. This *energy-momentum* or *E-k* diagram displays the energy of a particle in the valence and conduction bands of germanium as a function of its carried momentum [Kno99]. The band gap of forbidden energies is also shown in the shaded area of the figure. Figure 3.7 also illustrates the transition which promotes an electron from the valence band into the conduction band. This transition shall be made from the absolute maximum of the

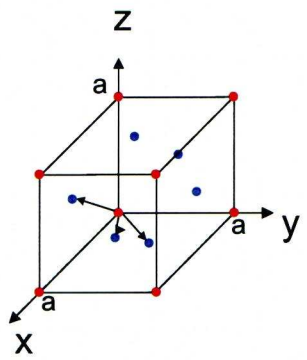

(a) Face Centred Cubic Lattice

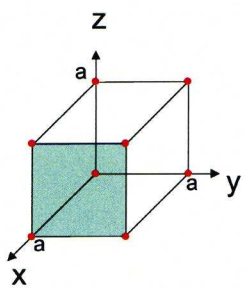

(b) <100>

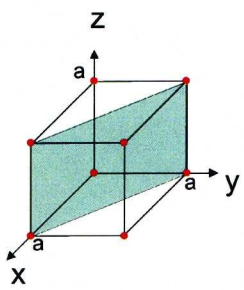

(c) <110>

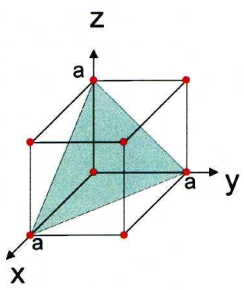

(d) <111>

Figure 3.6: Figure 3.6(a) depicts the structure of a face centred cubic lattice such as germanium. The red discs indicate the atoms separated by the lattice constant a, while the blue discs indicate the additional atoms characteristic of the FCC structure. Figures 3.6(b),3.6(c) and 3.6(d) show the <100>, <110> and <111> lattice plane, highlighted by the blue shading, respectively.

Atomic Number (Z)	32
Atomic Weight (A)	72.6 g/mol
Density	5.32 g/cm^3
Dielectric Constant (ϵ_r)	16.2
Intrinsic Carrier Concentration	2.0 x 10^{13} cm^{-3}
Intrinsic Resistivity	47 Ωcm
Energy Gap (300 K)	0.67 eV
Energy Gap (0 K)	0.77 eV
Ionisation Energy E_{pair}	2.96 eV
Electron Mobility (300 K)	3900 cm^{2}V/s
Hole Mobility (300 K)	1900 cm^{2}V/s
Lattice Constant (a)	556.75 pm

Table 3.1: Electrical and chemical properties of germanium.

valence band to the absolute minimum of the conduction band. The $E-k$ diagram shows how this is not a vertical transition but also requires a change in momentum. Semiconductors with this attribute are referred to as indirect semiconductors. The momentum necessary for this transition is taken from a *phonon*. The phonon is a quasi-particle which carries the vibrations of the crystallographic lattice structure. It has been demonstrated, in both experimental and theoretical work, that the absolute minima of the conduction band for germanium lie along the <111> axis [Sho50, Car66].

3.3.2 Charge Carrier Production

Electrons created by the physical procedures described in Section 3.1 will interact with the crystal, either by the ionisation of surrounding atoms or by emitting *Bremsstrahlung*. Although Bremsstrahlung only becomes dominant above ~2 MeV it shall be mentioned here for completeness. The total energy deposited by an electron in matter per unit length

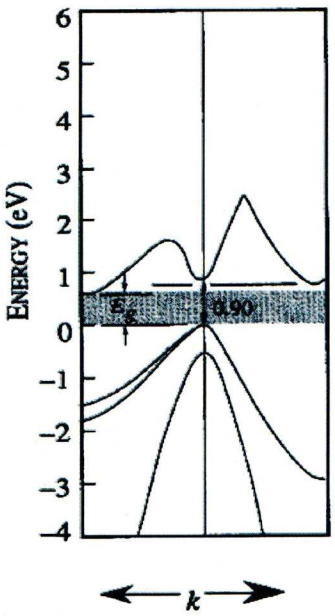

Figure 3.7: A schematic diagram of the energy of the particles situated within the valence and conduction bands of germanium as a function of their momentum. The band gap of forbidden energies for germanium is indicated in the shaded grey area [Kno99].

is described by

$$\left(\frac{dE}{dx}_{total}\right) = \left(\frac{dE}{dx}_{ionisation}\right) + \left(\frac{dE}{dx}_{bremsstrahlung}\right). \tag{3.22}$$

A photoelectron released in the crystal will lose its energy by the generation of electron-hole pairs. The number of pairs created (N_{pair}) is dependent on the energy deposited by the γ ray, E_γ, and the energy required to liberate an electron-hole pair from the crystal structure (E_{pair})

$$N_{pair} = \frac{E_\gamma}{E_{pair}}. \tag{3.23}$$

Equation (3.23) or more directly the ionisation energy E_{pair} is responsible for the spectroscopic performance of a material. For germanium E_{pair} is $\simeq 3\,\text{eV}$ [Peh68] while for a

typical scintillation detector, such as thallium doped-sodium iodide (NaI(Tl)), is 2 orders of magnitude higher at $\simeq$300 eV [Lee03]. The greater number of charge carriers ultimately results in more accurate representation of the deposited energy.

The statistical variation (ΔN_{pair}) on the number of generated charge carriers (N_{pair}) is, therefore, the first fundamental limitation to the achievable energy resolution of any semiconductor radiation detection device. Due to these properties, germanium is an ideal detector choice for spectroscopic applications in nuclear physics.

As the generation of an electron-hole pair is a probabilistic and repetitive occurrence, Poisson statistics were first chosen to quantify the uncertainty ΔN_{pair}. However, [Fan47] demonstrated that a modified Poisson distribution must be utilised as the probability of producing an electron-hole pair is not independent of previous charge liberation. A correction factor termed the *Fano factor (F)* was thus introduced. Inclusion of the Fano factor allows ΔN_{pair} to be calculated using

$$W_D = \Delta N_{pair} = \sqrt{F N_{pair}} = \sqrt{F \frac{E_\gamma}{E_{pair}}}. \tag{3.24}$$

In germanium, the Fano factor is $\sim$0.06 [Pap04] while in NaI(Tl) Poisson statistics apply and F $\sim$ 1.0. In addition to the statistical fluctuation in the number of generated charge carriers discussed above (W_D), the uncertainty in a measured energy is influenced by two further factors. For optimum spectroscopic performance, the amount of charge liberated by the γ-ray interaction must be fully collected on the detector contacts. Any charge carriers which become trapped in defects within the crystal structure [Sim49] or recombine [Hal52, Sho52] will introduce additional uncertainties [Kno99]. *Charge trapping* and *charge recombination* are combined as the error due to incomplete charge collection and termed (W_X). The final contribution arises from the error caused by electronic noise in the system (W_E). The energy resolution or full width at half maximum (FWHM) of a peak in a γ-ray spectrum is fundamentally limited to the quadrature sum of these contributing factors and is defined by

$$FWHM = W_T = \sqrt{W_D^2 + W_X^2 + W_E^2}. \tag{3.25}$$

These terms have been quantified as a function of energy for a standard coaxial detector and are presented graphically in Figure 3.8 as reproduced from [Kno99]. The figure displays how the summed contribution from all three sources scales linearly with increasing γ-ray energy. The influence of noise upon the energy resolution remains constant with increasing deposited γ-ray energy, while the effect from charge trapping is linearly proportional to the deposited energy due to the increase in the number of charge carriers.

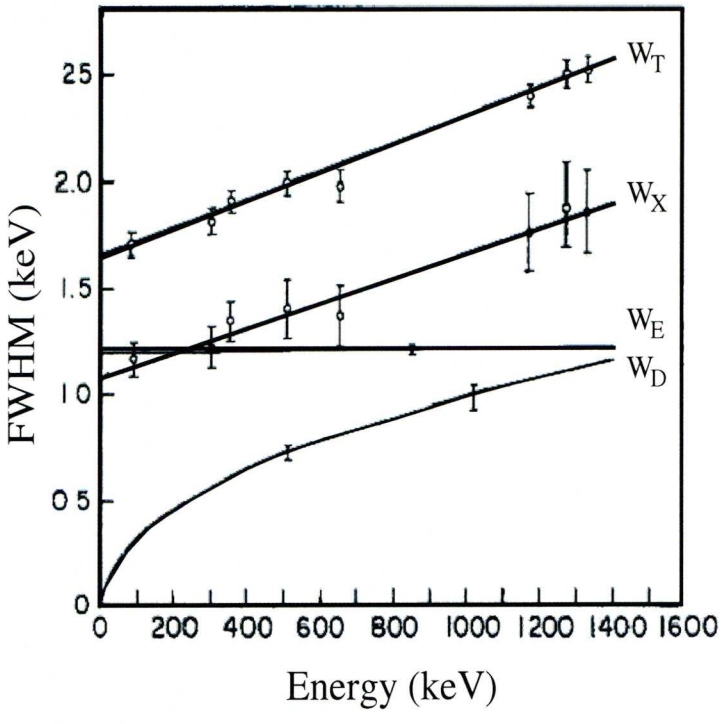

Figure 3.8: A graphic representation of the various contributing factors to the energy resolution for a coaxial germanium detector and their sum W_T. W_D is the statistical uncertainty on the charge carriers produced per eV of deposited energy, W_X is the uncertainty due to incomplete charge collection and W_E is the influence of electronic noise [Kno99].

3.3.3 Signal Generation in Germanium

In a germanium detector, the electric field across the depletion region draws the liberated charge carriers towards the contact of opposing polarity. Their motion within the electric field $\vec{E}$ induces a time-dependent current ($i(t)$) upon the detector electrodes. By measurement of $i(t)$, quantitative information is gained regarding the number of charge carriers created (N_{pair}), thus establishing a relation between the energy deposited by the γ-ray and the measured signal. [Sho38] and [Ram39] published that $i(t)$ is a function of the amount of liberated charge present (q), the electric field ($\vec{E}$) strength, the position- and time-dependent drift velocity of the charge carriers ($\vec{v}_d$) and the electric potential ψ. $i(t)$ is thus described by

$$i(t) = q\frac{\vec{E}(x,t)\vec{v}_d(x,t)}{\psi}. \tag{3.26}$$

While Equation (3.26) holds for single electrode devices, it is complicated by detector segmentation, as charge is induced and collected on separate electrodes. The concept of a non-physical weighting potential and a corresponding weighting field was introduced to aid this calculation for mulitelectrode detectors [He00].

The weighting potential describes the electrostatic coupling between a charge carrier at position x and an electrode at unit potential providing the remaining electrodes are grounded. The problem is thus reduced to being solely geometry dependent.

A schematic diagram of a multielectrode detector and its weighting field is shown in Figure 3.9. The contours on the diagram quantify the weighting potential ϕ_0. The observed current as a function of time ($i(t)$), shown below the contour map, indicate the amplitude of charge observed on the electrode at unit potential for the two depicted charges q. The migration of q and the structure of the weighting field along its path define the current signal observed on the respective electrode.

Although the assumptions discussed above are not valid in a real detector, [He00] demonstrated that the charge induced on any electrode is independent of both the potential applied to other electrodes and the magnitude or presence of space-charge. This observation validates the Schockley-Ramo theorem derived in [Sho38] and [Ram39] for segmented

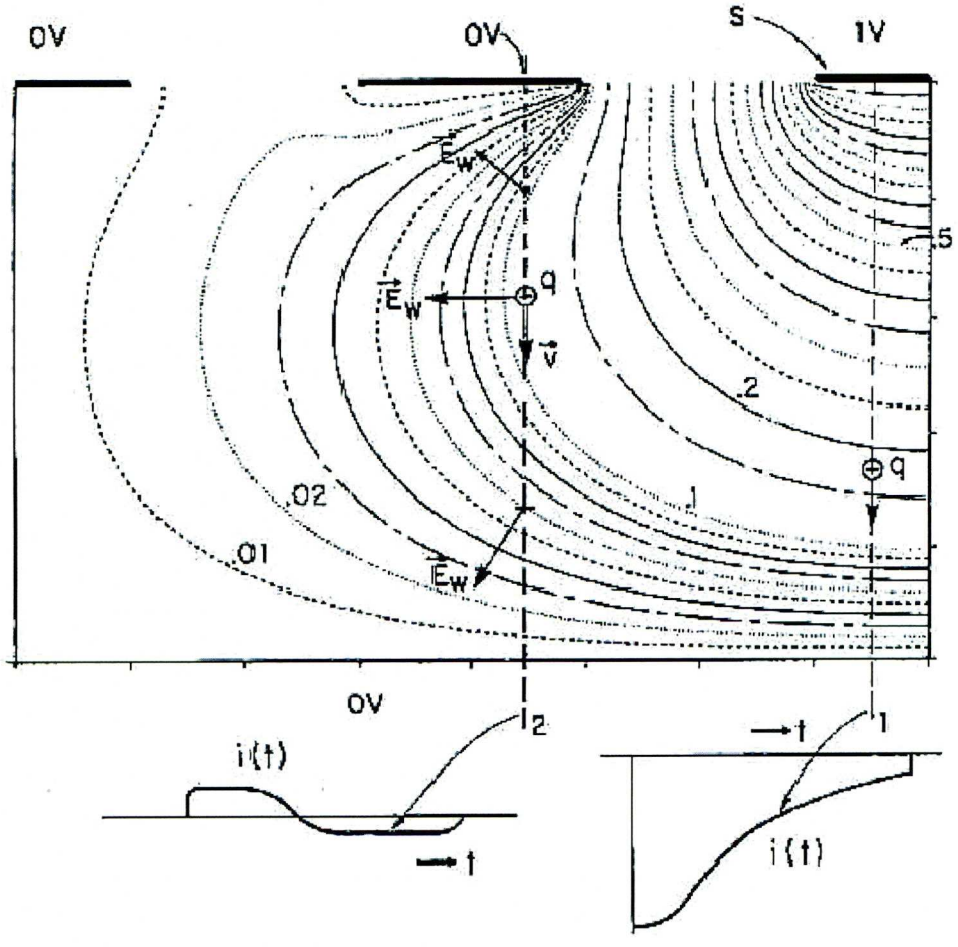

Figure 3.9: A diagram showing the weighting potential from an electrode at unit potential. The current induced on the same electrode when two separate charges q travel through the weighting field are depicted beneath the potential map in the $i(t)$ curves.

detectors of any geometry. This permits the current and charge induced in a detector segment by a moving point charge to be defined by

$$i = q\vec{v}_d E_0(x) \tag{3.27}$$

$$Q = -q\phi_0(x), \tag{3.28}$$

respectively, where ϕ_0 and E_0 are the weighting potential and field. For detector readout it is important to understand the amount of charge induced (Q) as a function of time (t) by a moving charge (q) as it is this physical quantity which shall be processed by an electronic unit such as a preamplifier. $Q(t)$ is described by

$$Q(t) = -q\phi_0(x(t)). \tag{3.29}$$

Although the charge cloud released within a semiconductor detector is of a finite size, the weighting potential as described in [He00] is still applicable. With relation to the detector geometry, the charge cloud dimensions are understood to be minimal and saturate at $\sim$1 mm even at energies of several MeV [Kro99]. The spreading of the charge cloud has been made subject of closer study in works such as [Kro99]. Their conclusions justify approximating the charge cloud to a point-like entity and add weight to the assumptions in [He00].

3.3.4 Anisotropic Charge Carrier Drift Velocity

The drift velocity of a charge carrier is linked to the size of the electric field and its mobility (μ) according to

$$\vec{v}_{d,e} = \mu_e \vec{E}(r) \text{ for electrons} \tag{3.30}$$

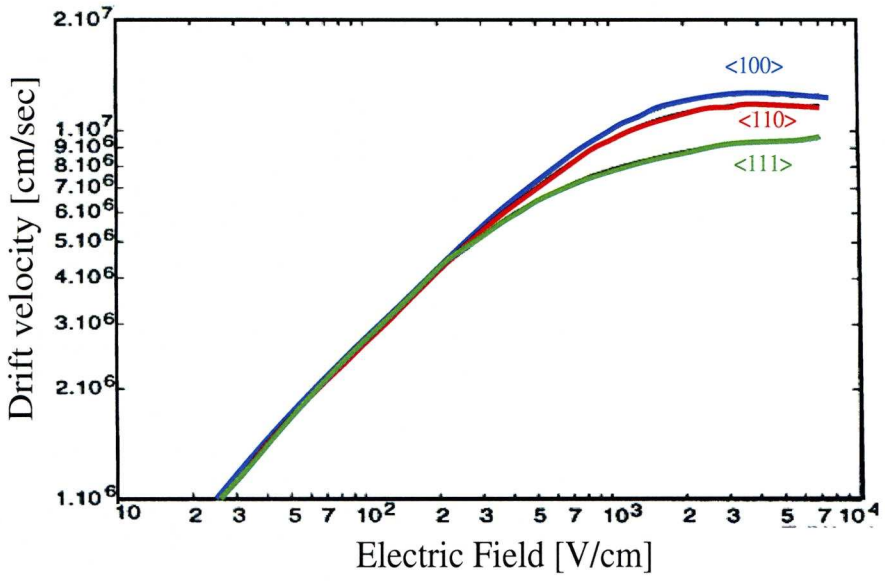

Figure 3.10: A graph of the drift velocity $\vec{v}_d$ of the electrons as a function of the magnitude of the electric field. The effect of the lattice orientation on $\vec{v}_d$ begins to contribute above an electric field of ~120 V/cm [Mih00].

or

$$\vec{v}_{d,h} = \mu_h \vec{E}(r) \text{ for holes.} \tag{3.31}$$

The charge carrier mobility will vary, dependent upon the crystallographic plane or Miller index it travels along. The electron drift velocities, for all three lattice orientations, as a function of applied bias voltage are shown in Figure 3.10 as reproduced from [Mih00]. This is an important criterion to consider in the design of a semiconductor detector. In planar detectors (Section 3.4.4), the bias must be applied along the axis facilitating easy charge migration in order to reduce charge recombination and trapping and produce an efficient charge collection system. It is also important to align the electric field vector with the <100> plane as a misalignment results in an angular offset between the drift velocity $\vec{v}_d$ and $\vec{E}$. This may, ultimately, result in a divergence of the charge cloud path [Mih00].

3.3.5 The Preamplifier

In the semiconductor detector relevant to this work, the current signal is processed by a preamplifier unit and integrated to produce a charge signal. Specially-developed, high-bandwidth, charge-sensitive preamplifiers are utilised. The current signal is initially processed using a *field effect transistor* (*FET*), to improve the signal-to-noise ratio and this signal is transferred to the preamplifier. The preamplifier step is necessary to amplify the current as the insufficient amount, generated within the crystal, cannot be manipulated directly. For signal-to-noise purposes, the preamplifier is located as close as possible to the detector, to minimise capacitive loading in connecting cables. Finally, the amount of the charge, i.e. the height of the charge signal produced by a charge sensitive preamplifier, contains information on the number of liberated charge carriers, N_{pair}. In data analysis, calculations are performed on the charge signal to extract its height and, with it, the energy deposited in the crystal.

Figure 3.11 displays a schematic diagram of a typical charge-sensitive preamplifier installed in a semiconductor detector. R_f and C_f are the feedback resistor and feedback capacitor respectively. A typical value for R_f is $\sim$1 GΩ and $\sim$1 pF for C_f. The product of $R_f \times C_f$ defines the time constant. For the preamplifiers used in this study, $R_f \times C_f$ = 50 μs.

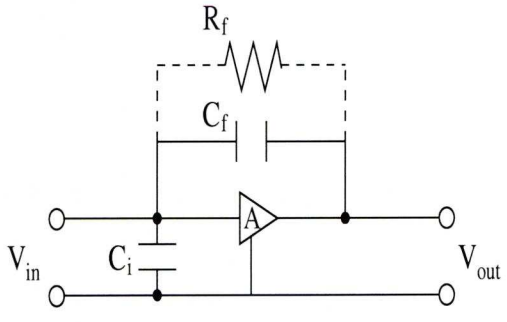

Figure 3.11: A schematic diagram of a resistive feedback charge sensitive preamplifier. The charge will be stored in the capacitor C_f and released slowly in an exponential decay proportional to the decay constant $R_f \times C_f$.

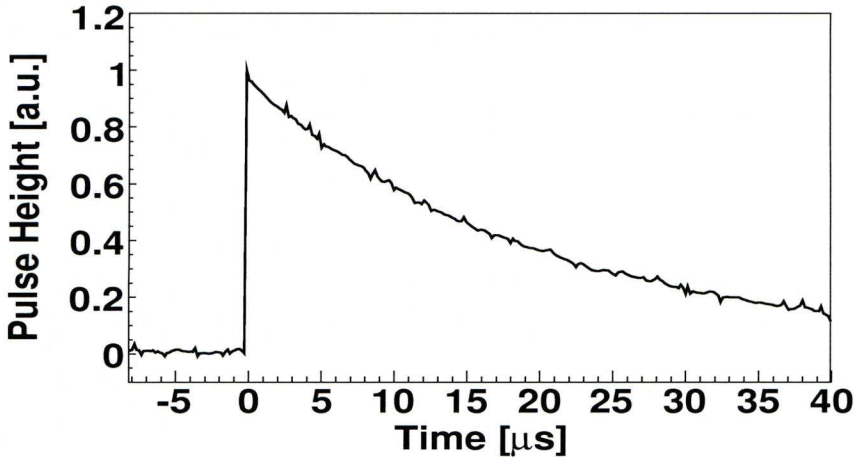

Figure 3.12: A sample preamplifier pulse digitised from a segmented planar HPGe detector. The initial fast rise as the charge is collected and the exponential decay as the capacitor C_f discharges are clearly seen.

Figure 3.12 provides an example of a preamplifier signal recorded with a digital oscilloscope from a HPGe segmented planar detector. The pulse shows the initial fast rise of the pulse as the charge is collected. The rising edge of the pulse is a convolution of both the intrinsic risetime of the preamplifier and the current induction due to the motion of the charge carriers. The intrinsic risetime was measured using a pulser to be 30 ns in [Tur06]. The risetime parameter (T90) is defined as the length of time passed for the pulse to go from 10% of its height to 90%. T90, along with analogous parameters such as T30 or T50, is often used in pulse shape assessment and will be discussed in detail and applied to experimental data in Chapter 6. The second shaping feature of the preamplifier is introduced by the discharge of the capacitor C_f. As charge accumulates within C_f, the capacitor will begin to decay. This is most easily observed in the exponential decay of the preamplifier after the charge is fully collected. The decay of the charge within the preamplifier is governed by

$$Q = Q_0 e^{-t/R_f C_f}. \tag{3.32}$$

3.4 Applications of Germanium Detectors

In this section the development of the HPGe detector will be discussed. Important metrics, for quantifying detector performance, shall be introduced and the historic route leading to detector applications outside of nuclear spectroscopy outlined.

3.4.1 Detector Performance

In order to evaluate detector performance, it is critical to develop figures of merit common to all detector systems. The categories addressed here are: efficiency, energy resolution, timing resolution and position resolution.

Efficiency

In general, the *efficiency* is the probability of a detection system producing a response to incident radiation. All stages of the detection system contribute toward the efficiency, including the interaction material (e.g. solid crystal or gas) and any subsequent electronics (e.g. photomultiplier tube). The efficiency is divided into three sub-categories:

Absolute Efficiency

The *absolute efficiency* (ϵ_{Abs}) is a direct ratio between the number of γ rays emitted and those detected during a measurement. The number of emitted γ rays is calculated according to Equation (3.33), using the activity of the source at time t ($A(t)$), the branching ratio of a given emission energy ($P(E_\gamma)$) and the acquisition time(τ_{exp})

$$\epsilon_{Abs} = \frac{N_{detected}}{N_{emitted}} = \frac{N_{detected}}{A(t) * \tau_{exp} * P(E_\gamma)}. \tag{3.33}$$

The *absolute photopeak efficiency* ($\epsilon_{Abs}(E_\gamma)$) quantifies the number of full energy absorptions for a given energy. In this case, only events in the photopeak contribute to the numerator, $N_{detected}$.

Intrinsic Efficiency

Although ϵ_{Abs} is a much employed metric, it is influenced by the source-detector geometry. For a representation more characteristic of material and/or system properties, the intrinsic efficiency ϵ_{Int} may be calculated. It was devised to normalise ϵ_{Abs} by the solid angle of a sphere covered by the detector

$$\epsilon_{Int} = \frac{A_{Det}}{\frac{4}{3}\pi r^3} * \epsilon_{Abs}, \tag{3.34}$$

where A_{Det} is the detector's surface area and r is the source to detector distance.

Relative Efficiency

As a means of comparing a system with a well understood and commonly available detector unit, the *relative efficiency* (ϵ_{Rel}) gauges the absolute efficiency relative to the efficiency of a 7.5 cm diameter and 7.5 cm long, cylindrical NaI(Tl) for the 1.332 MeV γ-ray emitted from a ^{60}Co source at 25 cm distance.

Energy Resolution

The *energy resolution* of a detector is a measure of the ability to produce a low uncertainty on an energy deposit. Individual systematic and statistical factors contributing to the energy resolution were discussed, in more detail, in Section 3.3.2. In this work, the energy resolution shall be quantified by the full width at half maximum (FWHM) of the Gaussian photopeak observed in an energy spectrum. In some documents, the σ parameter of a Gaussian fit is selected for this purpose. When performing to specification, a typical coaxial HPGe detector will produce a FWHM of <2 keV at 1.332 MeV.

Timing Resolution

The uncertainty on the γ-ray interaction time is an additional important property of a detection system. As with the efficiency, the *timing resolution* (τ) is a result of both the chosen detector material and the signal processing electronics [Kno99]. Ideally, a detector (in conjunction with its electronics) will have the ability to produce and collect a signal

rapidly, minimising the uncertainty on the interaction time. Firstly, accurate timing resolution is important in order to correctly identify the number of γ-ray interactions. Any energy deposits occurring within a time Δt are not resolved if $\Delta t < \tau$. In this case the interactions are falsely interpreted as a single deposit of the summed energy. Also in any form of coincident data readout, the ability to effectively define a narrow coincidence window results in higher quality data due to a larger fraction of *true coincidences* and a reduction of *random coincidences*. These terms are discussed in more detail in Section 2.6. The timing resolution of a system is most commonly quantified as the FWHM of a peak in a time spectrum between two "coincident" signals from separate detectors.

3.4.2 Lithium-drifted Germanium Detectors

A p-n junction with an applied reverse bias was first introduced as a radiation spectrometer in the 1950s by [Tea50]. However, in these early stages of semiconductor development, the devices were more suited to the detection of short range particles (e.g. α particles) rather than more penetrating γ rays [Kno99]. The reason for this was the thickness of the depletion region (d) defined by

$$d = \sqrt{\frac{2\epsilon V}{eN}}, \tag{3.35}$$

where V is the reverse bias voltage, e is the charge of an electron and N is the net impurity concentration. The thickness of a depletion region d was restricted by the net impurity concentration N. In order to produce thicker detectors, capable of attenuating particles with longer mean free paths, a reduction in the impurity concentration was required. For example, for a crystal to produce a 10 mm depletion width at a bias of 1000 V, an impurity concentration as low as 10^{10} atoms/cm^3 is necessary. Although such impurity levels were not possible at the time, thicker depletion regions were reached by [Pel60] in 1960 in silicon (Si) and reproduced for germanium in [Fre62]. Both publications avoid directly removing the impurities present in the crystal by compensating for them by introducing a dopant of opposing polarity. Commonly crystals were drifted with lithium (Li) after their growth in which case they are given the symbols Si(Li) and Ge(Li) for drifted silicon and

germanium respectively. This approach allowed germanium based p-n junctions of up to 20 mm to be manufactured, providing a much more efficient detector for higher energy photons.

3.4.3 High-Purity Germanium Detectors

The Ge(Li) detectors discussed above were, unfortunately, very inconvenient to operate as they required permanent liquid nitrogen cooling, even when no external bias supply was applied. This meant that any form of maintenance or transport was an inherently tedious procedure. New methods to grow germanium crystals were devised in the 1970s, which produced the desired net impurity concentrations directly, without lithium drifting. The earliest documentation of such crystal growing techniques were published in [Han71], while these ideas were later applied to detector manufacturing in [Hal71]. The technique begins with melted germanium and uses a germanium seed to grow a crystal from the liquid element. By adapting such parameters as the temperature gradients, seed rotation and withdrawal speed, properties of the new crystal can be controlled. Due to the distribution coefficients of the undesired impurities [Hal71] and their solubility [Kno99], the impurities accumulate in the liquid crystal, effectively filtering the newly grown solid crystal. With this technique, impurity levels as low as $10^{10}\,\mathrm{cm}^{-3}$ have been documented in the purest regions of the crystal [Hal71]. The purity of the crystal allows it to produce depletion regions which rival Ge(Li) crystal without the inconvenience of permanent cooling. Although the crystal must be cooled when biased; for storage, travel and repair purposes it can be allowed to warm to room temperature without its impurity level being affected. This was a major breakthrough in producing large volume devices, which were able to travel around the world as radiation sensors.

3.4.4 Detector Geometry

High-purity germanium detectors are generally manufactured into two different shapes: *planar* and *coaxial*. Figure 3.13 illustrates an example of both these types. The *planar* detector (Figure 3.13(a)) is defined by application of the bias potential across two opposing

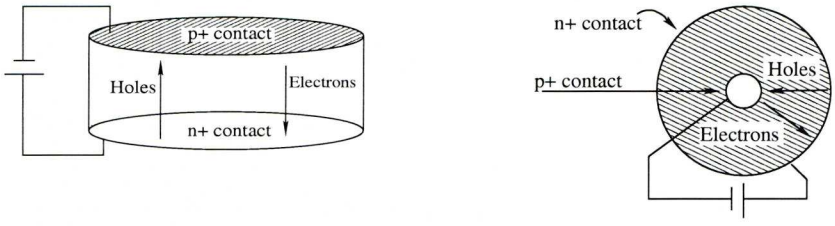

(a) Planar Detector Geometry (b) Coaxial Geometry

Figure 3.13: Schematic illustrations of both a planar (Figure 3.13(a)) and a coaxial detector geometry (Figure 3.13(b)). The difference, in where the potential is applied and how the charge carriers migrate, is displayed.

surfaces of the crystal. Conventionally, planar detectors are thinner square or rectangular crystals (up to $\approx 2\,\text{cm}$ thick) with each charge carrier species generally migrating in the same direction with respect to the lattice axes. *Coaxial* detectors, as depicted in Figure 3.13(b), have a more cylindrical shape and can be produced in larger volumes. The potential is applied between the outer surface of the cylinder and an inner, cylindrical contact produced by removing a *core* from the cylinder centre (see Figure 3.13(b)). For this geometry, charge carriers will migrate inwards or outwards depending on their polarity.

3.4.5 Detector Contacts

The charge signal is read out through detector *contacts*, which must be either n^+ or p^+ in their dopant concentration. With current technology, the n^+ contact is produced by lithium diffusion or evaporation onto the wafer surface, while the p^+ contact is formed by implantation of donor atoms using an accelerated beam. Most commonly, boron is chosen as the implanted dopant. An alternative to this approach was developed in [Han77], which allowed the contacts to be made thinner and less susceptible to neutron damage. The authors show that a contact fabricated from amorphous germanium can operate as a blocking contact. Today, HPGe contacts are most commonly manufactured from either lithium diffusion/boron implantation or amorphous germanium [Amm08].

3.4.6 Detector Segmentation

One disadvantage of large volume HPGe crystals was their poor position resolution. In nuclear structure experiments, this has major repercussions for the measured energy resolution due to Doppler broadening effects [Nol94]. The very first steps taken to address this problem involved simple restriction of the detector's opening angle, through lead collimation (as first used in the HPGe array TESSA0 [Twi81]) [2].

Fuelled by the desire to further improve position resolution for nuclear structure experiments, [Mac94] developed a lithographic technique to segment the outer contact of a coaxial detector effectively dividing the active volume into subsections with negligible loss of efficiency. The number of separable detector volumes (*granularity*) was enhanced, reducing position uncertainty on the interaction and minimising Doppler broadening. Detector segmentation was later applied to planar HPGe detectors, most commonly either by pixelating one contact (*pixel detector*) or by segmenting both contacts into orthogonally aligned strips (*Double-Sided Strip Detector* or *DSSD*).

3.4.7 Pulse Shape Analysis

The term *Pulse Shape Analysis (PSA)* covers any type of analytical technique where additional details, regarding an interaction, are obtained from the shape of the charge or current pulses. Such studies have been performed since the 1970s [Bru75], but it is the examination of interaction position, as a function of pulse shape, which prompted the expansion of semiconductor usage into other fields. The first attempts were conducted by [Krö96] using an unsegmented EUROBALL [Sim97] HPGe detector. Advancements on these efforts are documented in [Vet00], where a segmented detector was utilised to produce three dimensional position sensitivity in a segmented coaxial HPGe detector. In [Vet00], pulse shapes were categorised into *real charges*, induced directly by the collection of a charge cloud, and *image charges*, induced upon neighbouring segments by charge

[2] A similar technique is still employed in present arrays such as GAMMASPHERE [Del87] and TIGRESS [Gar07] where the BGO suppression shields extend beyond the front of the detector additionally acting as a geometric collimator.

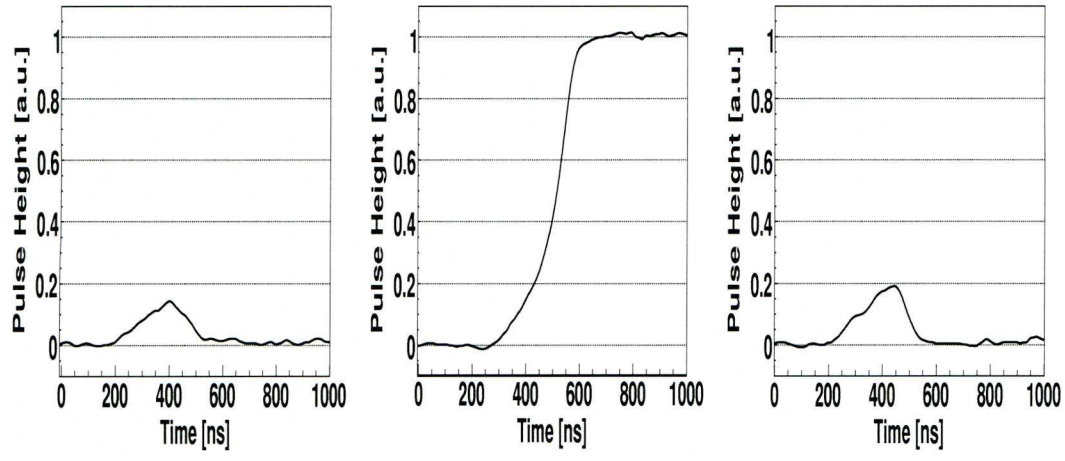

Figure 3.14: An example of pulse shapes as they appear after digitisation. The pulses have also been normalised. (centre) an example of a *real charge* as observed on the electrode where an interaction occurs. (left) and (right) are examples of *image charges* as induced on immediately neighbouring segments by the charge cloud migration.

cloud motion toward the contacts. Figure 3.14 displays an example of a typical real charge pulse, recorded by a segmented HPGe planar strip detector. Thorough analysis of the pulse shapes and/or some of their selected properties[3] (e.g. integral or rise-time) led to two major breakthroughs: firstly the γ-ray was localised along an unsegmented dimension (in the case of [Vet00], this was the radial dimension) and secondly, position resolution was improved much beyond the dimensions of the smallest segment.

Unsurprisingly, as it became clear that position resolution on the order of several mm was achievable using PSA, new detector arrays were designed to take advantage. Most famously, the long anticipated GRETA [Del99] and AGATA [Sim03] arrays will apply sophisticated PSA-algorithms to the digitised pulse shapes to achieve interaction position resolution of 2-3 mm[3]. Coupling the position resolution with germanium's excellent spectroscopic performance allows exploitation of Compton kinematics to reconstruct the

[3]Analysis of certain parameters of the pulse rather than its whole shape is often referred to as *parametric* PSA

interaction path throughout the array's entirety (*Gamma-Ray Tracking* or *GRT*). GRETA and AGATA will be the first nuclear physics arrays to reconstruct the γ ray path despite scatter between detectors. This increases the arrays' efficiency by orders of magnitude [Del99, Sim06, Bos07c] at 1 MeV, as events Compton scattered between detectors are no longer rejected. Although the application of these techniques in nuclear spectroscopy is not the subject of this work, the high position resolution developed in nuclear physics inspired scientists, from a wide range of disciplines, to apply semiconductors and HPGe to their fields.

3.4.8 Gamma-Ray Imaging Applications with Semiconductors

Across a broad range of fields, it is of interest to produce an image representing the locational distribution of a γ-ray source. Exploiting a principle first published by [Tod74], which would become known as the *Compton camera*, it was the Compton telescope (COMPTEL) [Sch78] to first experimentally demonstrate γ-ray imaging, albeit using NaI(Tl) scintillators. Further experimentation into Compton imaging was carried out by [Sin83], first applying Compton cameras to medical imaging and designing a system making the collimation stage of a Gamma Camera redundant. This field of research remains very active today with a multitude of proposals and systems currently under study e.g. [Yan01, Tak05, Mih07]. Another field of medical imaging, which is evolving through the use of semiconductor detectors, is positron emission tomography. Semiconductor detectors show much promise and may form the basis for the next generation of PET scanners [Tai05]. Numerous PET systems have been developed at research level using mercuric iodide (HgI_2) [Dah85], cadmium telluride (CdTe), silicon (Si) [Aur05], Cadmium-Zinc Telluride (CZT) [Ish07] and germanium [Bos07a, Coo09], while the effects on the medical industry are also well documented [DIm00, MNT08]. This work shall discuss a specific example of such an application of germanium detectors to positron emission tomography.

Chapter 4

The SmartPET Project

In the latter half of the last century, much research effort focused on the application of semiconductors to medical imaging [Act03, Tai05]. SmartPET (SMall Animal Reconstruction Tomograph for Positron Emission Tomography) [Bos07a] was a collaborative project between the University of Liverpool and STFC (formerly CCLRC) Daresbury Laboratory established in 2003 and is an example of a semiconductor-based medical imaging proposal. SmartPET utilises two segmented, planar HPGe detectors in a dual-head PET camera configuration. The detectors are coupled to digital pulse processing electronics and mounted in a rotating gantry to acquire radiation intensity projections at an angular range of 180°. The detailed digital sampling of the detector response enables application of sophisticated pulse shape analysis routines to produce high resolution images.

4.1 The SmartPET Detectors

Identically designed detectors (SmartPET1 and SmartPET2) were manufactured for the project by ORTEC [ORT]. Each is a Double Sided Germanium Strip Detector (DSGeSD), containing a HPGe crystal of 74 mm x 74 mm x 20 mm. These dimensions include a 7 mm wide guard ring, indented along the 74 mm edges, leaving an active crystal volume of 60 mm x 60 mm x 20 mm. A technical drawing of the crystal inside one of the SmartPET detectors is provided in Figure 4.1 (left). Figure 4.1 (right) highlights the crystal axes.

The active volume is orthogonally segmented into 12 strips with a 5 mm strip pitch. The manufacturer reports that both HPGe crystals have a comparable impurity concentration of $\sim 6 \times 10^9$ cm^{-3} with the impurity gradient not exceeding 5% through the depth (20 mm) of the crystal [San05a]. Charge carriers migrate through the 20 mm depth of the crystal, which follows the <100> lattice axis to within 1° [San05a]. As addressed in Section 3.3.4, this axis is capable of fastest charge transportation and aids optimum charge collection. The orthogonal strip segmentation is illustrated in Figure 4.2. The crystals are operated at -1800 V and, according to documentation provided by the manufacturer [San05a], deplete at -1300 V. Detailed information regarding the contact material on the detector faces has not been disclosed by ORTEC, however the AC coupled (p+) contacts (Figure 4.2(a)) have a $\approx$0.3 μm thickness and are separated by 180 μm (*inter-strip gap*). On the DC blocking contact (n+) (Figure 4.2(b)) the inter-strip gap is 300 μm and the contacts are 50 μm deep. The output from each contact is fed to an ORTEC-designed warm Field Effect Transistor (*FET*) and a fast charge sensitive preamplifier with a gain of 300 mV/MeV. The preamplifiers are designed for low-noise and high-bandwidth signal processing and have a decay time of $\tau \sim 54\,\mu$s. The risetime of the preamplifier has been quantified at 30 ns in [Tur06].

4.2 Digital Electronics

The SmartPET system requires highly-developed, digital electronics to perform sophisticated pulse shape analysis and achieve high spatial localisation of a γ-ray interaction. In addition, the electronics must be capable of operation at high count rates, to acquire sufficient statistics in the available time defined by the half-life of the radioisotope. In the case of fluorodeoxyglucose (FDG), a commonly used PET substance based on the decay of fluorine-18 (^{18}F), one half-life lasts $\approx$110 mins [DRU].

The digital acquisition units extract energy and time information from the charge response of the detector. For this reason, the pulse shapes or *waveforms* are digitised at a high frequency and recorded for offline analysis. Two types of digital electronics units

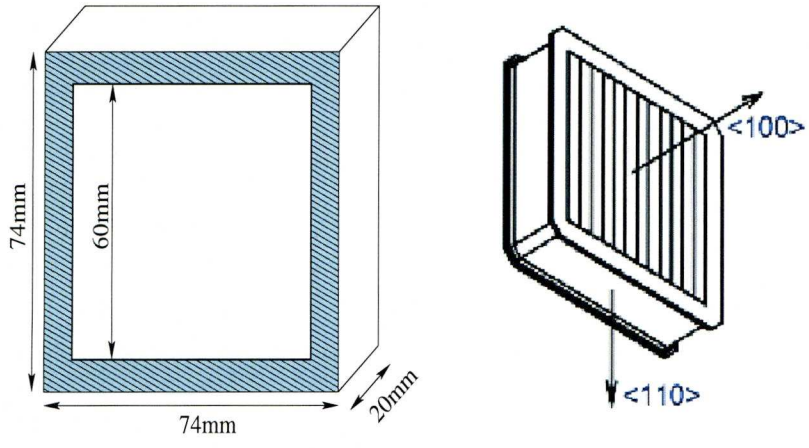

Figure 4.1: A technical drawing illustrating the dimensions of the crystal (left). The shaded area indicates the guard ring while the unshaded area indicates the active volume. (right) highlights the crystal axes. The charge carriers are collected along the <100> axis.

have been employed in SmartPET measurements: the well-understood and previously commissioned four-channel Gamma-Ray-Tracking (GRT) VME module [Laz03] and the more sophisticated, commercial Lyrtech VHS-ADC card [LYR]. The Lyrtech VHS-ADC units are currently being optimised for their role in the project and are in the development and testing phase.

4.2.1 The Gamma Ray Tracking 4 Cards

One GRT4 card is implemented with four 14 bit 80 MHz flash *Analogue to Digital Converters* (*ADC*s). Each analogue input trace is processed by a 40 MHz, low-pass, Nyquist filter to reduce the effects of electronic noise on the pulse shape. Processing is performed by two Xilinx Spartan 2 *Field Programmable Gate Arrays* (*FPGA*s), the first providing a 512 sample circular buffer, a digital trigger algorithm and a calculation of the deposited energy based on a *moving window deconvolution* (*MWD*) algorithm [Geo94]. The second available FPGA offers the potential for further pulse processing and trace buffering [Laz03]. The GRT4 cards are administered a common external *trigger* pulse, typically a

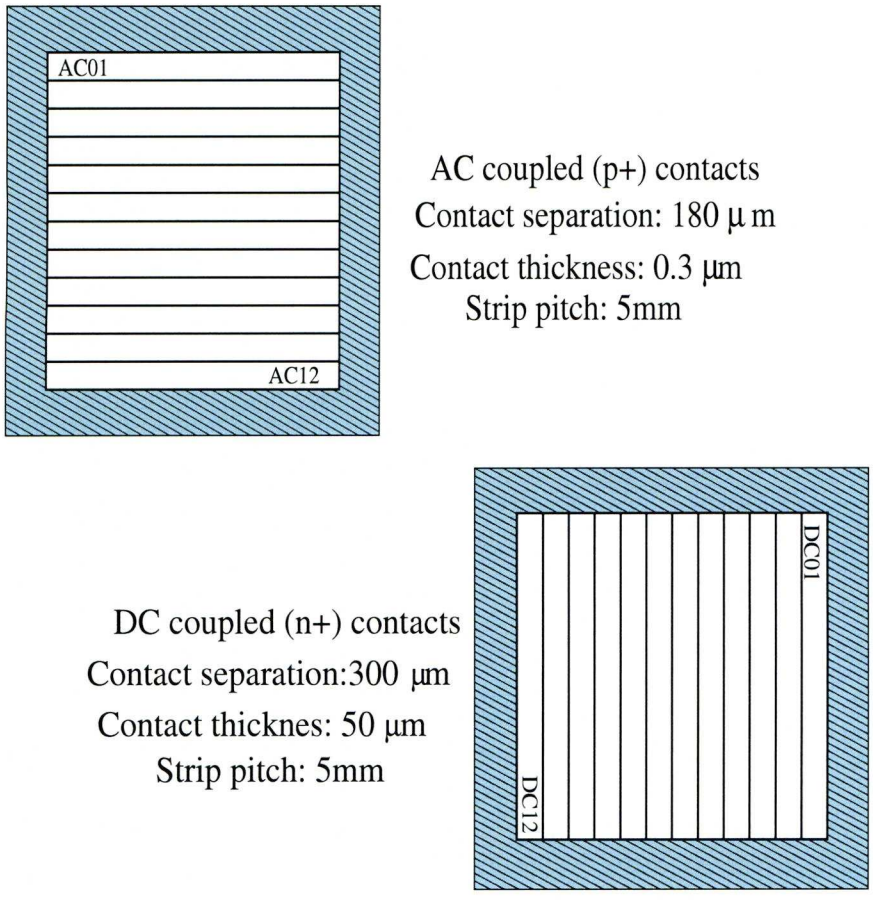

Figure 4.2: A display of the orthogonal strip segmentation on both the AC and DC faces of the detector. The shaded area of the crystal indicates the guard ring.

NIM logic pulse, as a signal to begin data storage. During data transfer, the cards return a *busy* or *inhibit* signal to the trigger system to prevent additional trigger signals. A detailed discussion of the experimental setup is found in Sections 4.6 and 6.2.

The GRT4 cards suffer from two major limitations which motivate their replacement by the Lyrtech ADCs: firstly, the readout of the VME crate which contains the GRT4 cards is limited to approximately 4Mb/s (~220 Hz per VME crate). Secondly, they are only temporally synchronised (*time aligned*) locally to each VME module. This means that although four channels within a card are collectively time stamped, the remaining cards

are not synchronised with each other. This weakness has dramatic implications for the pulse shape analysis algorithms [Dim08], see Section 6.8.

4.2.2 The Lyrtech Analogue to Digital Converter

The commercially available Lyrtech VHS-ADC digitiser cards [LYR] benefit from a significantly higher readout rate and a global time-synchronisation. Their high readout rate of 50 kHz per channel, dramatically exceeds the previous 220 Hz overall rate in the GRT4 setup. The radiation sources, measured in SmartPET experiments so far, have not challenged this count rate, resulting in a system with virtually zero dead time. The 16 14- bit ADCs operate at a sampling frequency of up to 105 MHz and are implemented with high-capacity Virtex-4 programmable FPGAs. Upon full implementation, the more advanced FPGAs shall permit online pulse shape analysis. This reduces the offline analysis time and the disk space required as only interaction parameters such as position (x, y, z) and energy (E) are stored. The global time stamp is crucial to the performance of sophisticated pulse shape analysis algorithms and is an additional reason why the full system is not programmable in the GRT4 electronics system. It should be stressed that the high readout rate is essential to the success of the SmartPET project as a majority of PET imaging is conducted using short-lived radioisotopes, e. g. ^{18}F, which has a half-life of ~ 110 mins. Even this seemingly short half-life, when compared to laboratory sources, is one of the longer lived clinical PET isotopes (see Table 5.2). Producing images with this isotope is a crucial step in the project's success and is not possible using the GRT4 system.

4.3 The Rotating Gantry

As with most dual-head PET cameras, the two SmartPET detectors are mounted in a stable holding structure which physically rotates them around the *Field Of View* (*FOV*). The gantry itself was custom designed and built by the University of Liverpool and the rotation is executed by two, high-precision McLennan stepper motors. The angular po-

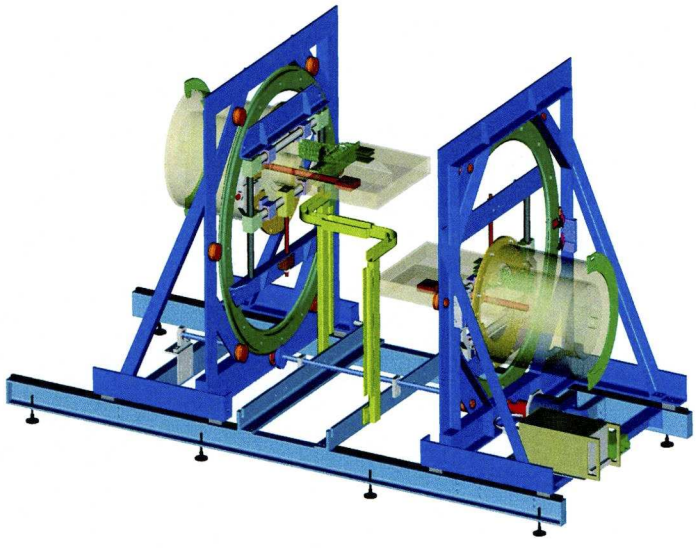

Figure 4.3: A CAD drawing of the SmartPET detectors mounted in their custom designed rotating gantry. The illustration includes the stepper motors and the central source holder.

sition of the stepper motors is coupled to the data acquisition system and included in the data stream. The motors operate with an angular step size as low as 400 increments per revolution (0.9°). The angular velocity is kept minimal to reduce microphonic noise induced by the motion of liquid nitrogen within the SmartPET dewars. A CAD drawing of the SmartPET detectors mounted in the gantry is presented in Figure 4.3.

4.4 Imaging with SmartPET

SmartPET was designed as a prototype system to evaluate the use of germanium in both PET imaging and Compton camera imaging ([Gil06]). The project has successfully demonstrated imaging capability with germanium in both of these modalities and led to a range of publications in imaging [Gil06, Coo09], fundamental understanding of detector response [Bos07a] and charge cloud behaviour and collection [Coo08]. The research carried out by [Mat06] and [Coo09] demonstrates undeniable potential in germanium-based scanners and the large impact of applying well-understood and fully-characterised detec-

tors to PET imaging. Complementary, collaborative work between Monash University, Australia and the University of Liverpool has resulted in highly successful Compton imaging publications [Gil06, Bos07b, Bev07]. With the fundamental possibility of performing imaging with a device similar to the SmartPET system established, it is crucial to be able to identify the limitations of the existing system.

4.5 The SmartPET Model

Attempting to answer these questions experimentally does not provide access to all the necessary information. In fact, the parameters are distorted as the radiation detection introduces many levels of uncertainty. Specifically, the general goal in nuclear imaging is to locate a radioactive decay, based on interactions of its products with matter. If, in detecting these products, an error is introduced (i.e. through the abilities of the detector), decoupling the uncertainty attributed to the physical process from the uncertainty for which the detector is responsible, is non-trivial. Although the origins of these distortions can be considered empirically [Mos93] and some single contributions can be studied through innovative experiment design [Der79, Der86a], their individual, quantitative impact on any one image cannot be measured. The individual contributions from all limiting factors (e.g. position resolution, timing resolution) are combined within the image and information, regarding the factors in isolation, is irretrievably lost. In a simulated data set, this is not the case. Providing the simulation truly represents the interactions with matter, access to the "true" interaction parameters, before they are distorted by the uncertainties of the experiment, is granted. Furthermore, one acquires information unobtainable experimentally, e.g. the interaction order. The near infinite level of precision on all parameters is not only beneficial in establishing system limitations, but also qualitatively assessing their origins. This knowledge is of general scientific interest, but is also essential for project evaluation and maximising the potential of current equipment and future systems in the design stage. As alluded to above, it is crucial to take particular care in interpreting simulated results. Without experimental comparison, miscalculations

may go unidentified. More importantly, a realistic link must be established between the performance and accuracy of the detector and the modelled data. Otherwise, no meaningful result can be concluded. For these reasons, the simulated results were thoroughly compared to experimental data and validated (Section 4.6).

4.5.1 The SmartPET Simulation Geometry

The SmartPET model is programmed in the Object Orientated (OO) C++ Geant4 (GEometry ANd Tracking) environment [Ago03]. Geant4 was selected as a simulation platform due to its extremely versatile functionality stemming from its OO roots. It allows free selection of parameters of interest and was more flexible than its competitors at the time of code development. The geometry, in the simulation, replicates the SmartPET detectors (Section 4.1) to the highest possible level of detail providing the information disclosed by the manufacturer.

The simulation geometry includes:

- The HPGe active volumes
- The surrounding guard ring
- The charge collecting contacts or dead layer[1].
- The aluminium cryostat housing
- The vacuum within the cryostat

[1] As the composition of the contacts has not been disclosed by the manufacturer the contacts were modelled as HPGe. This arises from the suspicion that they are manufactured from amorphous germanium[Gri64, Han77]. Reasons for this suspicion are two fold. Firstly ORTEC have commented that the contacts are not manufactured from lithium and boron [San05b] and secondly during discussions regarding SmartPET, M. Amman commented that given the contact geometry (particularly thickness) the contacts are highly likely to be manufactured from amorphous germanium[Amm08]

The simulation does not include:

- The copper cooling element surrounding the crystal
- Any cabling materials related to the FETs and preamplifiers
- The contact segmentation[2]
- Any mounting materials (e.g. screws)

The following validation results will clarify that neglecting these components had little impact on the accuracy of the simulated data.

4.5.2 The SmartPET Physics List

Primarily, the SmartPET model employs the *"G4LowEnergy"* physics package [Cha04] which is designed to reproduce electromagnetic interactions at low energies. A competing, available physics package to include was the *"Standard"* physics package. The most significant differences between the *"Standard"* package and its low energy equivalent are observed below 1 keV [Cha04]. Although energies this low are not of primary interest for this study, the long term aim of the SmartPET work is to produce a competitive diagnostic tool and the low energy physics package is documented to reproduce dose effects with higher accuracy than the "Standard" package [Cha04]. In Geant4, the *cut value* is the point at which the software is ordered to terminate a simulated track as below this threshold the microscopic detail of the particles path is no longer of interest. In this work the cut value was set to 100 μm.

4.5.3 Source Generation

With the exception of the simulations discussed in Sections 5.6.2 and 6.6, the SmartPET model has employed the *"GeneralParticleSource"* package (GPS) [QIN] to emulate radioactive sources. GPS permits a command line controlled source generation, while

[2]The contact segmentation was included offline.

its libraries include many fundamental source properties. This allows such attributes as source shape, emission particle, energy distribution and angular coverage (e.g. isotropic) to be called upon by a command series and do not need independently defining by the user. The sources utilised in this work include isotropic point sources, source planes and volumetric shapes such as cylinders. Both positron (e^+) and γ-ray sources were modelled and are discussed in full detail in their respective sections.

4.5.4 Data Stream

Data were written to file if radiation interacted with any part of either of the SmartPET active volumes or their guard ring. In this scenario, a range of information parameters was extracted from the simulation and stored in a list mode format for offline study. The list of parameters included the x, y, z coordinate of the interaction, a range of values for the energy lost in the interaction (e.g. energy lost by the particle, energy deposited in the crystal), the AC and DC strips in which the interaction occurred and the type of particle involved (e.g. photon or electron). The data were then analysed in the ROOT environment [ROO].

4.6 Simulation Validation

Monte Carlo simulations exploit random number generation in order to reproduce and predict the behaviour of a system. In order to maximise confidence in simulated results, it is important to validate the simulation by drawing comparison with experimental measurements. For this purpose, both experimentally acquired and simulated data shall be examined in parallel in this section.

4.6.1 Simulated Data

Simulations of the geometry described in Section 4.5.1 were conducted. The general particle source package [QIN] was employed to model isotropic, γ-ray emitting, point sources with experimentally available energies ranging from 80 keV - 1400 keV. The sources were positioned 25 cm above the aluminium housing of the detector.

4.6.2 Experimental Data

The geometry described above was assembled experimentally. Calibration sources emitting the modelled energies were, independently, placed 25 cm away from the aluminium detector housing. Data were acquired with both a europium-152 (^{152}Eu) and a barium-133 (^{133}Ba) source [3]. In all measurements, the 12 AC signals were divided into two paths: one to provide an external trigger for the data acquisition, the other for spectroscopic analysis. The 12 trigger signals each passed through a channel of an ORTEC 863 Quad *Timing Filter Amplifier* (*TFA*). The TFA output signals were then fed through ORTEC 935 Quad *Constant Fraction Discriminator* (*CFD*) units with a 60 keV discriminator threshold and a 20 ns internal delay. Data were to be recorded when at least one of the 12 channels registered an energy deposit above the 60 keV threshold. This was achieved by producing a logic pulse using a Phillips Scientific 755 Quad Majority *Logic Unit* which was subsequently delivered to a CAEN 32 Channel Multievent Peak Sensing analogue to digital converter (ADC). The DC pulses and other half of the AC pulses were input to

[3] Some additional data points were included from [Coo07b]

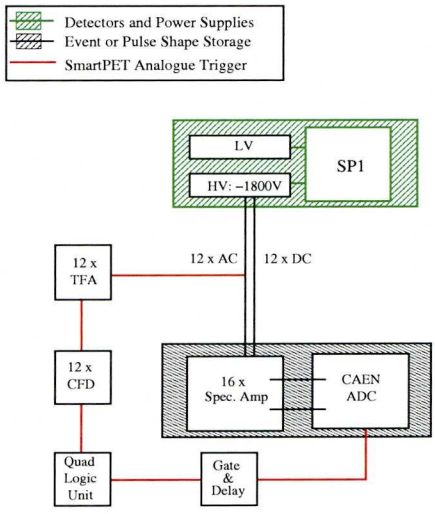

Figure 4.4: A graphic representation of the electronics setup assembled to acquire experimental validation efficiency data.

a CAEN N568LC 16 channel Programmable *Spectroscopy Amplifier* and then to the 32 channel ADC for digital energy storage. A schematic illustration of this setup is depicted in Figure 4.4.

4.6.3 Terminology

To ease the discussion of both the analysis and the results, two terms shall now be introduced. These will also feature in later sections of this document:

Fold

The *fold* of a detector face is defined as the number of strips which register energy exceeding a predefined threshold. The threshold is set intending to count the number of real charges in the detector. Values for the fold shall be quoted for each detector face using the $<AC\ fold\ ,\ DC\ fold>$ notation for one detector and
$<AC\ fold_1\ ,\ DC\ fold_1\ ||\ AC\ fold_2\ ,\ DC\ fold_2\ >$ for two detectors. The || symbol indicates that an order of the fold values is interchangeable. For example <1,1,2,1> demands AC $\text{fold}_2 = 2$, where <1,1||2,1> requires only that either detector registered a single fold event,

while the other contained only one fold two event.

Addback Energy

The term *addback energy* shall refer to the summed energy of all strips in a SmartPET detector face. In some cases, specific addback energies shall be discussed, for example the term *fold two AC addback* describes the summation of both detected energies in any event where the AC fold is two (<2,X>). The addback efficiency is calculated according to Equation 3.33 with only events which meet an addback criterion contributing to $N_{detected}$. An example of such a criterion may be an energy restriction.

4.6.4 Simulation Analysis

Simulated energy deposits in the SmartPET crystal were calculated along with an individual sum for each AC and DC strip. To account for further experimental effects, the following thresholds were applied:

- *Constant Fraction Discriminator threshold* - demanding that at least one of the energies in the AC strips exceeds the CFD threshold value of 60 keV. This parameter is analogous to the threshold which triggers the data acquisition.
- *Image Charge Threshold* - requires that the individual deposits on a strip are in excess of either 50 keV or a third of the photopeak energy as the acquisition system is otherwise likely to regard them as an image charge (Section 3.4.7) or noise.

The addback efficiency was then calculated by obtaining the number of energy deposits that fell within energy resolution of the source emission energy and dividing this by the total number of emissions.

4.6.5 Experimental Analysis

The experimental data were analysed in the MTsort environment [MTS], where a three-point, quadratic, energy calibration was carried out. When calculating an experimental

addback spectrum, residual charge induced in the electronics channels is undesirably included in the summation. This phenomenon referred to as *proportional cross talk* has been understood in SmartPET since [Coo08]. A correction was necessary when adding energy from neighbouring and next-to-neighbouring strips. If the interactions were separated by a greater distance, no effects of proportional cross talk were observed. The experimental absolute efficiencies were calculated using Equation 4.1 quoted below

$$\epsilon_{Addback} = \frac{N_{detected}}{N_{emitted}} = \frac{N_{detected}}{A(t) * \tau_{exp} * P(E_\gamma)}, \tag{4.1}$$

where $\epsilon_{Addback}$ describes the number of events which lie within a photopeak and meet a requested fold criterion. The reader is reminded that $A(t)$ is the activity of the source at time t, τ_{exp} is the data acquisition time and $P(E_\gamma)$ is the branching ratio of the γ ray of interest, as explained as part of Equation 3.33.

4.6.6 Validation Results

The absolute efficiencies for total addback, fold one addback and fold two addback shall be presented for both simulation and experiment over the 80 keV - 1400 keV energy range. Figures 4.5, 4.6 and 4.7 present the total addback, fold one addback and fold two addback values respectively for data acquired with the SmartPET1 detector and the source positioned above the AC face.

All three figures show a good level of agreement between simulated and experimental data with all values passing a standard consistency check. The most accurate agreement, over the energy range, is in the fold 1 data. In Figure 4.5 (total addback data), the simulated values are consistently higher than their experimental counter part, especially at low (0 keV - 200 keV) to intermediate (200 keV - 700 keV) energies. In the fold 1 data (Figure 4.6) the disagreement at low energy is maintained, where the intermediate energy points increase in accuracy. These two observations lead to the following conclusion. Firstly, it is argued that the over-prediction of the simulation at low energy in both data sets is due to photon attenuation. The detail of the interior of the SmartPET cryostat is unknown and, at low energy, any additional components excluded from the model could

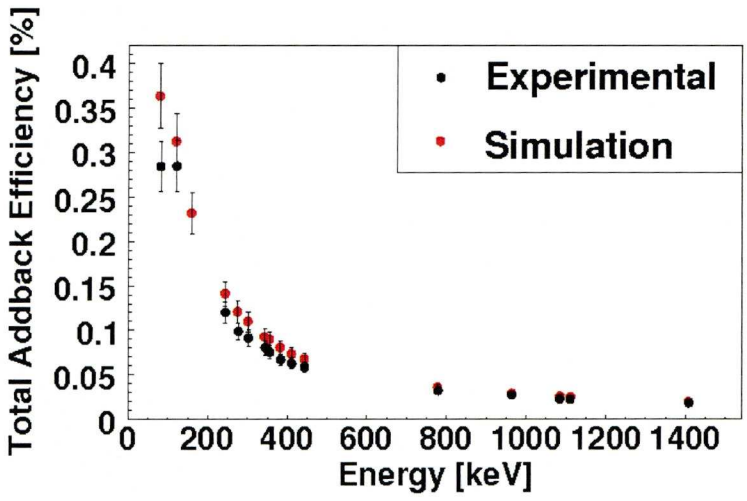

Figure 4.5: A comparison of simulated and experimental total addback efficiency for the SmartPET1 detector. The simulated points (red) and the experimental values (black) show reasonable agreement.

be responsible for the discrepancy. This hypothesis is consistent with the fold one results as any material difference between simulation and experiment will have the same effect, independent of fold.

Secondly, it is believed that the over-prediction in the total addback spectrum at intermediate energies is a result of the charge collection performance of the detector, particularly, in and around the inter-strip gap. The simulation does not bear any knowledge of charge clouds, their migration through the crystal or their charge processing within the electronics. Therefore, any effects produced by the charge cloud (e.g. charge loss, charge sharing, charge spreading, recombination and charge trapping) remain unmodelled. Any inefficiency regarding the collection of the charge cloud will only reduce the experimental addback efficiency and not the simulated data. Based on previous studies of SmartPET1 [Coo08], recombination and charge trapping are expected to be negligible; these phenomena are also rarely observed in high-purity germanium detectors.

The interactions which produce fold one data are contained entirely within one strip. As the discrepancy is not observed in the fold one efficiency curve, it is concluded that

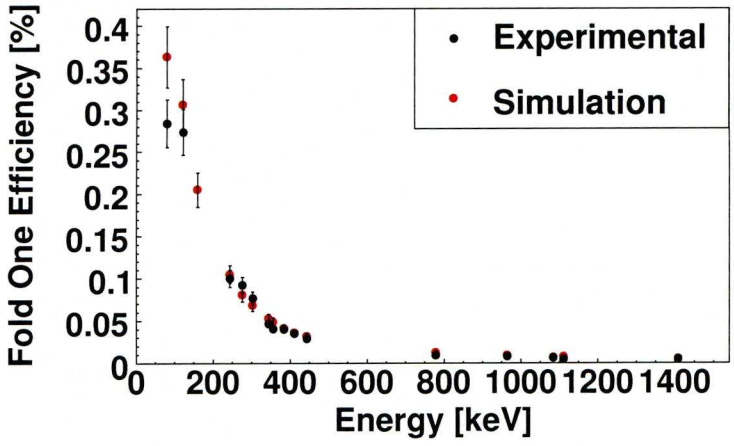

Figure 4.6: A comparison of simulated and experimental fold one addback efficiency for the SmartPET1 detector. The simulated points (red) and the experimental values (black) show reasonable agreement.

efficiency reduction is due to a process following the γ ray scattering across several strips and being added back. As the discrepancy only occurs at intermediate energies and reduces with increasing energy, it is argued that the effect is at its most prominent in Compton scattered events, separated by short distances. If charge were to be lost in the inter-strip gap between two segments, this would explain the reduction in the total addback efficiency. As energy increases, the two interaction sites are less likely to be in the vicinity of strip boundaries, reducing the probability of the charge cloud overlapping with the strip gap. As the energy range is increased further to the high energy range, scattered γ rays are more likely to travel through several strips. Therefore, the number of interactions at boundaries and any subsequent effects are reduced. Although the trend of the fold two values at intermediate energies support these statements, the uncertainties are deemed too large for this pattern to add further weight to the argument outlined above.

In Figure 4.7 it can be seen that the fold two data are higher in experiment than in simulation for low energy. It shall be stressed that this is the only occurrence of the

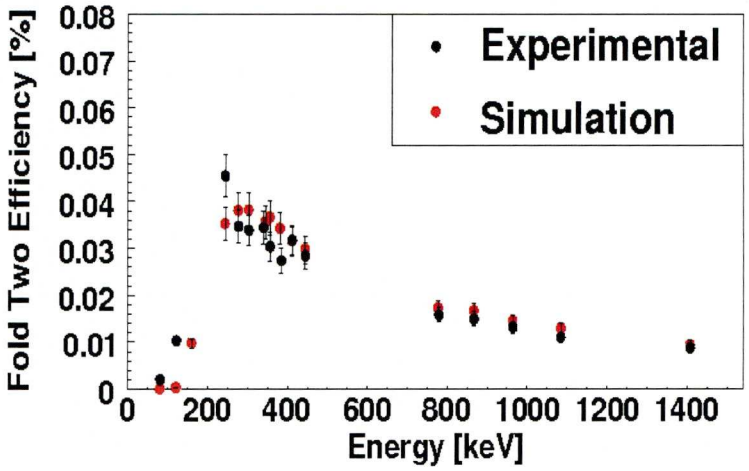

Figure 4.7: A comparison of simulated and experimental fold two addback efficiency for the SmartPET1 detector. The simulated points (red) and the experimental values (black) show reasonable agreement.

experimental values significantly exceeding the simulated counterpart. Again the charge cloud is believed to explain this discrepancy. During charge collection, close to the inter-strip boundary, the charge cloud can be split and shared between two electrodes. This phenomenon is known as *charge sharing* and will lead to a single interaction resulting in two separate charge clouds collected on neighbouring electrodes. In other words a fold one event will appear as a fold two event. Experimentally, both charge sharing and Compton scattering can produce a fold two event, whereas the simulation will only model Compton scattering. This explains the under-prediction of the simulation at fold two for low energy.

4.6.7 Summary

Although many discrepancies were discussed in detail above, generally the simulation shows excellent agreement with the experimental data. It is argued that the system has been modelled accurately and its output correctly interpreted. Any simulated results can be treated with the highest confidence level due to the successful validation of the SmartPET model. The simulation shall now be used to enhance the understanding of

SmartPET's performance as a positron emission tomograph in the following chapter.

Chapter 5

Positron Emission Tomography Imaging in Geant4

5.1 Motivation

The ability to reproduce radiation interactions within matter in a Monte-Carlo simulation provides an invaluable route to realistic data. The simulations offer a full understanding of the γ-ray path, free from the restrictions of physical materials and their inherent manufacturing cost. Simulated data are an essential tool in both understanding the potential and constraints of existing setups and in the design and optimisation of novel systems in development. This chapter shall focus on understanding the potential and limitations of the SmartPET system.

5.2 Producing PET Images from Simulated Data

Positron Emission Tomography (PET) data were simulated in the Geant4 environment [Ago03] to establish the imaging capabilities of the SmartPET system. Further aims were to quantify the effects of various experimental distortions upon image quality and prioritise design criteria for future PET systems. A final target was to devise a complex phantom geometry which can be reconstructed using this apparatus.

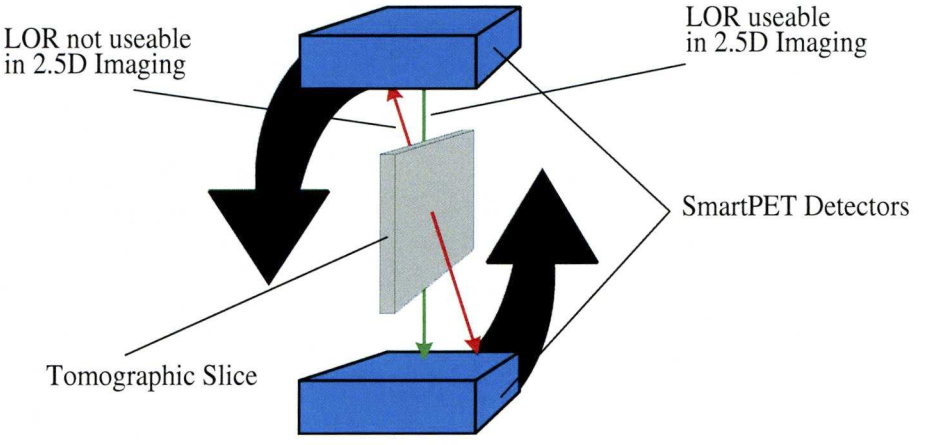

Figure 5.1: A graphic representation of the tomographic slicing principle and why only LORs which do not cross slices can feature in a 2.5 D reconstruction. Any LORs which cross slices must be rejected unless a 3 D reconstruction algorithm is developed. Further explanation is found in the text.

5.2.1 Acquisition of Simulated Data

In simulation, the SmartPET detectors were rotated from the 0° position to the 180° position around a positron emitting source in 10° increments. 5 million positrons were emitted per angular position. The source geometries were varied from simplistic point sources to complex extended phantom structures[1]. If each of the annihilation γ rays deposit energy in one of the SmartPET detectors (coincidence), the event and its necessary information parameters are recorded. As the data will be reconstructed into several two-dimensional slices of image space, lines of response could only be reconstructed if their depositions were in the same tomographic slice. This intermediate stage of imaging multiple two-dimensional slices is often referred to as 2.5 dimensional (2.5 D) imaging. Figure 5.1 illustrates the distinction between the two line of response categories graphically. The green LOR contributes towards 2.5 D reconstruction whereas the red LOR can only be included in a 3 D algorithm. A preliminary restriction, to exclude lines of response which are not common to one tomographic slice, was applied to reduce the data size.

[1]Their detailed structure shall be discussed in their relevant sections.

5.2.2 Reconstruction of simulated Data

Using a C++ algorithm in the ROOT environment [ROO], the lines of response were arranged into *sinograms* (Section 2.7). A sinogram is a two-dimensional histogram, where LORs are stored according to their displacement from a global point (the position, r) and the angle at which they were acquired (θ). This acts as the input format for the reconstruction algorithm and enables Fourier space filtering to be conducted. The sinograms were reconstructed with a Java [JAV] based Filtered Back-Projection algorithm (FBP) [Mat06] (or see Section 2.7.2) employing a RAMP filter. Figure 5.2 portrays a one-dimensional slice through a reconstruction of a point source, positioned near the centre of the Field Of View (FOV) at $(0.25, 0, 0.25)$ cm. The quarter centimetre displacement in the x- and z-dimensions ensures the source is placed centrally within a tomographic slice.

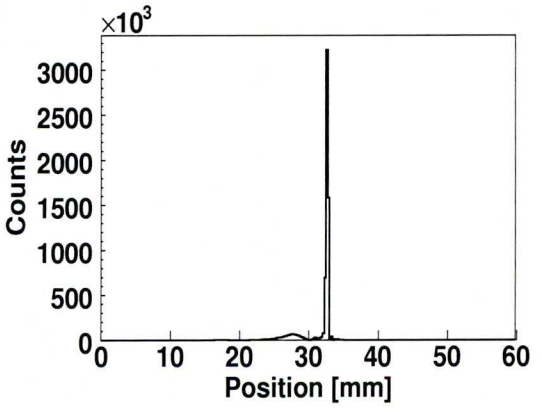

Figure 5.2: A one-dimensional slice through the reconstruction of the "perfect" point source reconstruction. Using the idealistic data from the simulation the intrinsic limit of the reconstruction algorithm can be measured.

5.3 Imaging Efficiency

5.3.1 Event Categories

An overview of the types of detected events is provided in Table 5.1 along with the fraction of the data which they constitute. The *relative fraction lost* is defined as the fraction of events remaining, since the previous restraint was applied. This metric was devised to highlight where the efficiency losses are greatest and which data processing stages require most attention. The imaging efficiency discussion is continued in Section 5.6.8 where the probability of defining a LOR correctly shall be assessed. In this section, the focus is placed on maximising the number of LORs usable to increase image efficiency.
From 90 million emitted positrons (5 million at each of the 18 angular projections), only 13 % of the produced annihilation photon pairs are incident upon the detector faces. This solid angle related constraint is controlled by the detector separation and surface area of the detectors. The effects of varying the detector separation shall be investigated in Section (5.6.6), yet increasing the detector surface area is implicitly linked with higher manufacturing cost. Although this step must be considered it is not a limitation imposed

Data Type	Number of Events	Fraction[%]	Relative Fraction Lost
Total Emissions	90 million	100	n / a
Incident on Detectors	12.2 million	13	0.13
Coincident Detections	1.9 million	2	0.15
LOR in one Slice	139257	0.155	0.073
Near parallel LORs	12792	0.014	0.092
Parallel LORs	5745	0.006	0.449

Table 5.1: An overview of the categories into which the emitted events fall. The relative fraction lost indicates the amount of data which is lost at each stage of the efficiency assessment.

upon the system by analysis methods [2]. The same statement is made for the second stage of efficiency loss. Here, the number of annihilation photon pairs, which interact in both detectors, is quantified. Only 2 % of photon pairs deposit energy in both detectors. The relative loss at this stage is $2/13 = 0.15$. This value indicates how the fraction of forfeited data due to the relatively low stopping power of germanium is approximately equal to that due to solid angle restrictions. The stopping power is an intrinsic property of the material and, again, can not be overcome by analysis methods, only by additional or higher Z material. The third stage of data rejection is due to the reconstruction algorithm. The 2.5 D nature of the algorithm places a constraint on the usable data as only LORs common to one slice can be reconstructed. This condition is also a large efficiency restraint and could be overcome with a volumetric three-dimensional reconstruction algorithm. However, the expansion from the 2.5 D imaging to 3 D imaging is non-trivial and results in much increased reconstruction time. Should PET imaging be pursued with this system, the development of such an algorithm is recommended, yet it shall not be addressed in this work.

5.3.2 Line of Response Categories

In previous experimental work [Mat06, Coo09], the system efficiency has been limited by the constraint of the reconstruction algorithm to process LORs, which do not align perpendicularly to the detector face. This issue is illustrated graphically in Figure 5.3, where LORs which fulfil this criterion are highlighted in the area shaded green. These shall be referred to as *parallel LORs*. Their position, r, is effectively equal in both SmartPET1 and SmartPET2 ($r_1 \simeq r_2$). To enhance efficiency of previous studies, LORs within the yellow shaded areas were included (*near-parallel LORs*, $r_1 \approx r_2$). It was argued in [Mat06, Coo09] that the angular parallax error, introduced by an inequality in r_1 and r_2, was negligible as the offset of up to 1 cm is projected across a 13 cm detector separation. The areas in which the detectors are shaded red contain *non-parallel* LORs.

[2] For completeness it must be stated that due to the crystal growth and manufacturing process (Section 3.4.3) there is a limitation to the achievable surface area of a planar HPGe detector.

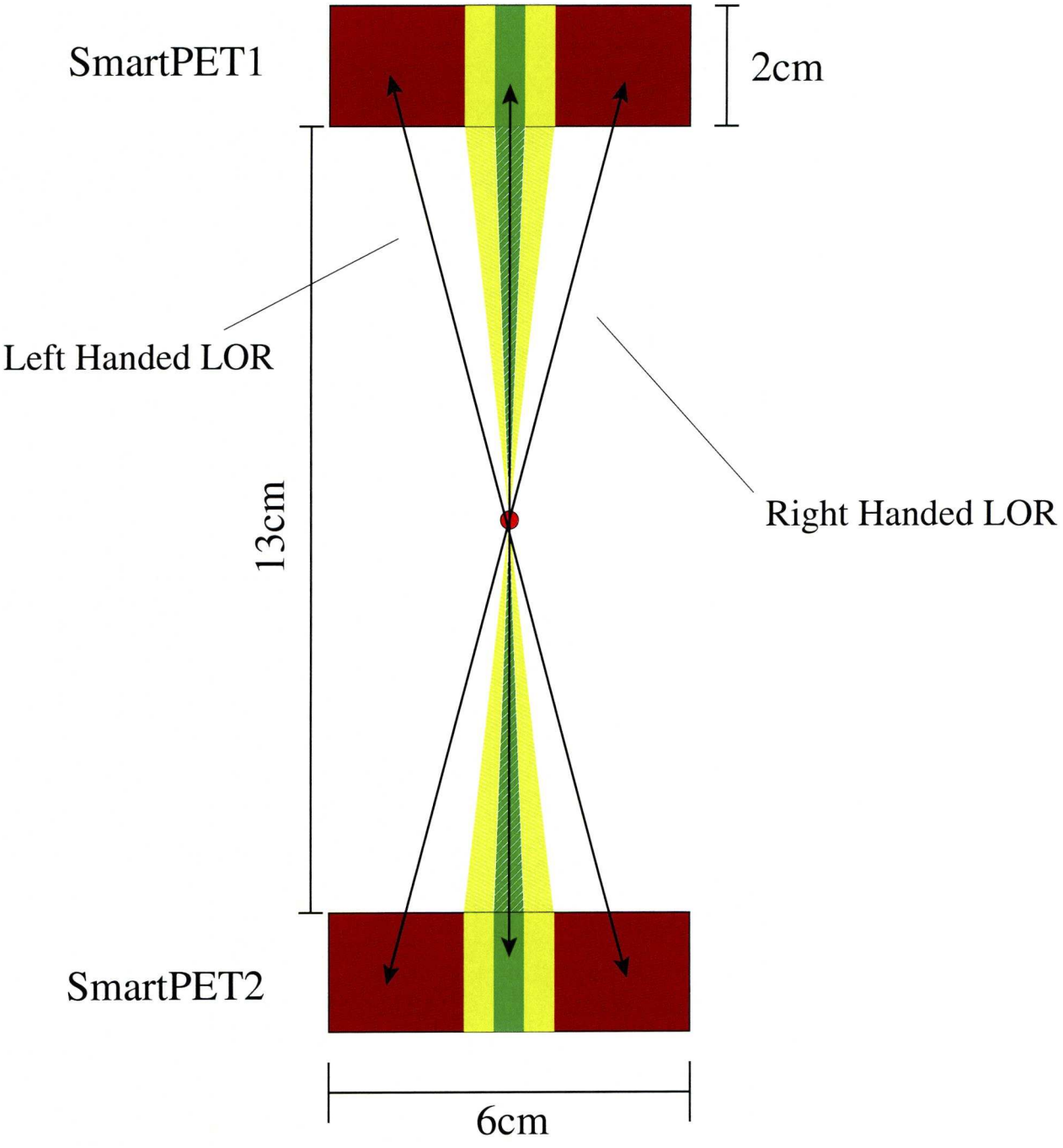

Figure 5.3: A schematic diagram of the different categories of LOR used in the sinogram production process. The area shaded green contains parallel LORs, while the yellow shaded area produces near-parallel LORs. The red shaded area comprises non-parallel LORs which require a frame of reference rotation before they can be included in the reconstruction. The reader is referred to the text for further details.

The non-parallel LORs are further sub-divided into two categories, depending on whether the opening angle between the LOR and SmartPET1 is positive or negative. The term *left handed LOR* is used when the opening angle is in the same direction as the detector rotation; *right handed LORs* are the reverse case. In previous work, non-parallel LORs were rejected as the reconstruction algorithm was unable to deal with LORs where θ did not equate to the detector position. Unfortunately, this is a major restriction upon imaging efficiency as only a marginal fraction of events (0.016%) fall into either the parallel and non-parallel LOR category.

5.3.3 Maximising usable Lines of Response

The image reconstructions presented in this work approach this problem differently, introducing an additional term: the *angle of incidence* (η). The angle of incidence is designed to decouple the angle of the LOR from the physical position of the detector and is calculated using basic trigonometry as

$$\eta = 90 - \zeta, \tag{5.1}$$

where ζ is the angle between the LOR and the inside surface of SmartPET2. Figure 5.4(a) displays the two SmartPET detectors and two LORs, one opposite (P with interaction positions $P1$ and $P2$) and one non-opposite (Q with interactions positions $Q1$ and $Q2$). The angle of incidence, for the non-opposite line of response, can hence be calculated using

$$\eta_Q = 90 - \zeta = 90 - \text{atan}\frac{|\text{Q2}_\text{y} - \text{Q1}_\text{y}|}{|\text{Q2}_\text{z} - \text{Q1}_\text{z}|}. \tag{5.2}$$

In the figure, the detectors are positioned at $\theta = 0°$. As the parallel LOR has an angle of incidence η_P equal to the angle of the detectors θ, it can feature in the sinogram without further manipulation at a sinogram position $p_P(r, \theta = \eta)$. In order to include the non-parallel LOR Q, its coordinates are rotated by an angle ρ and the displacement calculated for the hypothetical situation in which the LOR were acquired at $\theta = \eta_Q$.

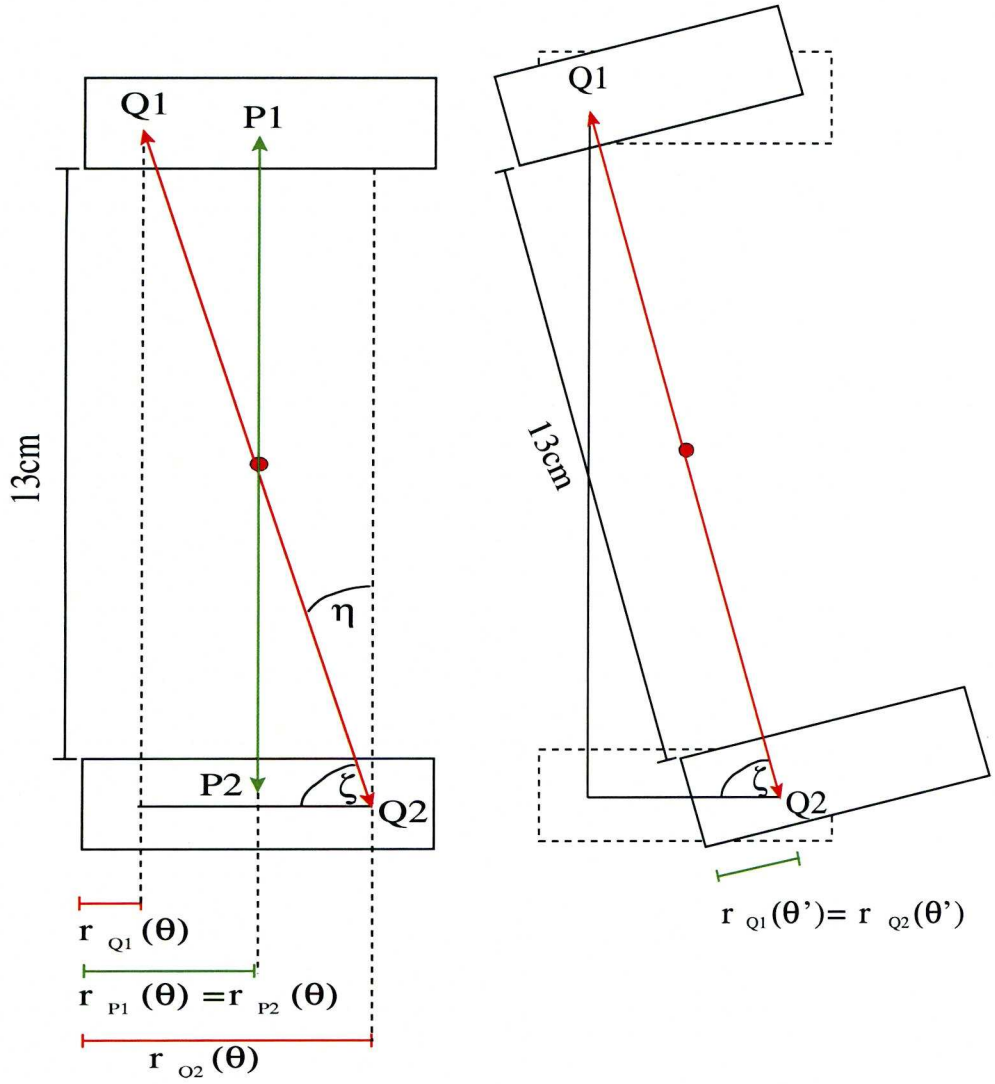

(a) $r_{Q1}(\theta) \neq r_{Q2}(\theta)$ (b) $r_{Q1}(\theta') = r_{Q2}(\theta')$

Figure 5.4: (a) An illustration of a non-parallel LOR and the parameters necessary to rotate the frame of reference for its inclusion in the image reconstruction. (b) the same LOR with the detectors rotated around it so that its new coordinates define its position as a parallel LOR.

The rotation matrix

$$\mathcal{M} = \begin{pmatrix} \cos(\rho) & -\sin(\rho) \\ \sin(\rho) & \cos(\rho) \end{pmatrix}$$

is used, where for left-handed LORs

$$\rho = \eta + \theta; \tag{5.3}$$

and for right-handed LORs

$$\rho = 180 - \eta + \theta. \tag{5.4}$$

The new interaction coordinates for the LOR in the rotated frame of reference are determined with

$$Q1' = Q1 \times \mathcal{M} \tag{5.5}$$

and

$$Q2' = Q2 \times \mathcal{M}. \tag{5.6}$$

In this reference frame, the rotated displacements r'_{Q1} and r'_{Q2} equate. The LOR can now be included in the sinogram with the entry $p_{Q\,left}(r', \eta + \theta)$ for left-handed LORs and $p_{Q\,right}(r', \eta - \theta + 180)$.

5.3.4 Advantages to Rotational Correction

The benefits of calculating an angle of incidence and rotating the axis frame around lines of response are threefold. Firstly, the imaging efficiency increases by a factor of 24.2 using all LORs over parallel LORs only. Subsequently, the reconstruction process only rejects events which are not unique to one tomographic slice. This could only be overcome by expanding the algorithm to a full three-dimensional volumetric imaging package. The rotation correction method also has accuracy implications as a parallax error, in parallel or near-parallel LORs, is no longer neglected, but corrected for by performing the rotation, even on LORs offset by small angles. Although the parallax error may have been minimal,

especially for parallel LORs, the method is fundamentally more reliable. Finally, image quality is enhanced (not just by improved statistics), as the number of angular projections has increased. The angular projections are not bound to the detector position, because data are effectively acquired at all angles, without an increase in sampling angles and/or acquisition time. It is possible for the sinogram to cover a range of 0° to 180° degrees in steps of unity despite the detectors sampling in larger increments. The application of this correction to all LORs justifies the sampling in 10° increments in the PET simulations executed in this work.

5.4 Image Quality Assessment

The precision with which a reconstructed image resembles the original object is referred to as the *resolution* of an image. High resolution implies a close match between object and reconstruction, while low or poor resolution indicates a distorted reconstruction. In the case of point sources, this work quantifies image resolution according to the *Full Width at Half Maximum* (*FWHM*) of a one-dimensional slice through the centre of a two-dimensional image map along either the x- or y-axis. The *Full Width at Tenth Maximum* (*FW.1M*) shall serve as an additional measure of image resolution in some cases. To minimise uncertainty, a Gaussian fit is performed upon this distribution using the MINUIT package [MIN], to access a standard deviation (σ) on the mean. The standard deviation is converted into a FWHM using

$$FWHM = 2\sigma\sqrt{2\ln 2}\,. \tag{5.7}$$

5.5 Distortions of Image Quality

In positron emission tomography, deficiencies in image resolution stem from multiple physical and experimental origins. Figure 5.5 is a flow diagram of the steps which occur before an image is reconstructed from PET data. The size and shape of the source is first distorted by the kinetic motion of the positron (positron range). Upon annihilation, the

two γ rays produced are assumed to be emitted at 180°. Their angular offset, of 0.5-1.0°, is a further source of error. Although more problematic in SPECT and human PET, there is a possibility of either or both γ rays Compton scattering in the subject (Section 2.6.2), leading to a definition of a LOR, which does not contain the annihilation site. Figure 5.5 displays the above steps inside a "black-box", as they occur before the γ rays reach the detector. Throughout, the figure separates information which can be retrieved in a simulation (red boxes, left column) from information available in a fixed experimental setup (green boxes, right column). The effects inside the "black-box" in the top-left of the diagram are inaccessible with a fixed experimental setup. The figure highlights how a large number of parameters are not directly available to the data acquisition system, as they are lost before an interaction occurs in the detector. The stages within the "black-box" can be essential to understanding image quality and are an important subject of study. Some information can be acquired by using specifically designed systems such as those in [Der79, Der86a]. An additional route to information on these parameters is provided by a validated simulation of the experiment, such as the model discussed in Section 4.6. The simulation offers direct and correct access to the parameters, before they are distorted by the experimental equipment, the analysis algorithms and/or the reconstruction routines. The simulation grants precise position and deposited energy values, where a detector would blur these parameters by its respective resolution. The simulation also offers the true number of interactions, where a detector is generally only aware of multiple interactions if they take place in different segments. Parameters such as the interaction order are only available in simulation. It shall be stressed that the validation is an essential step in this process and it is not the results of either column in isolation but the cross-referencing and knowledge between both which allows these effects to be quantified and a system to be better understood.

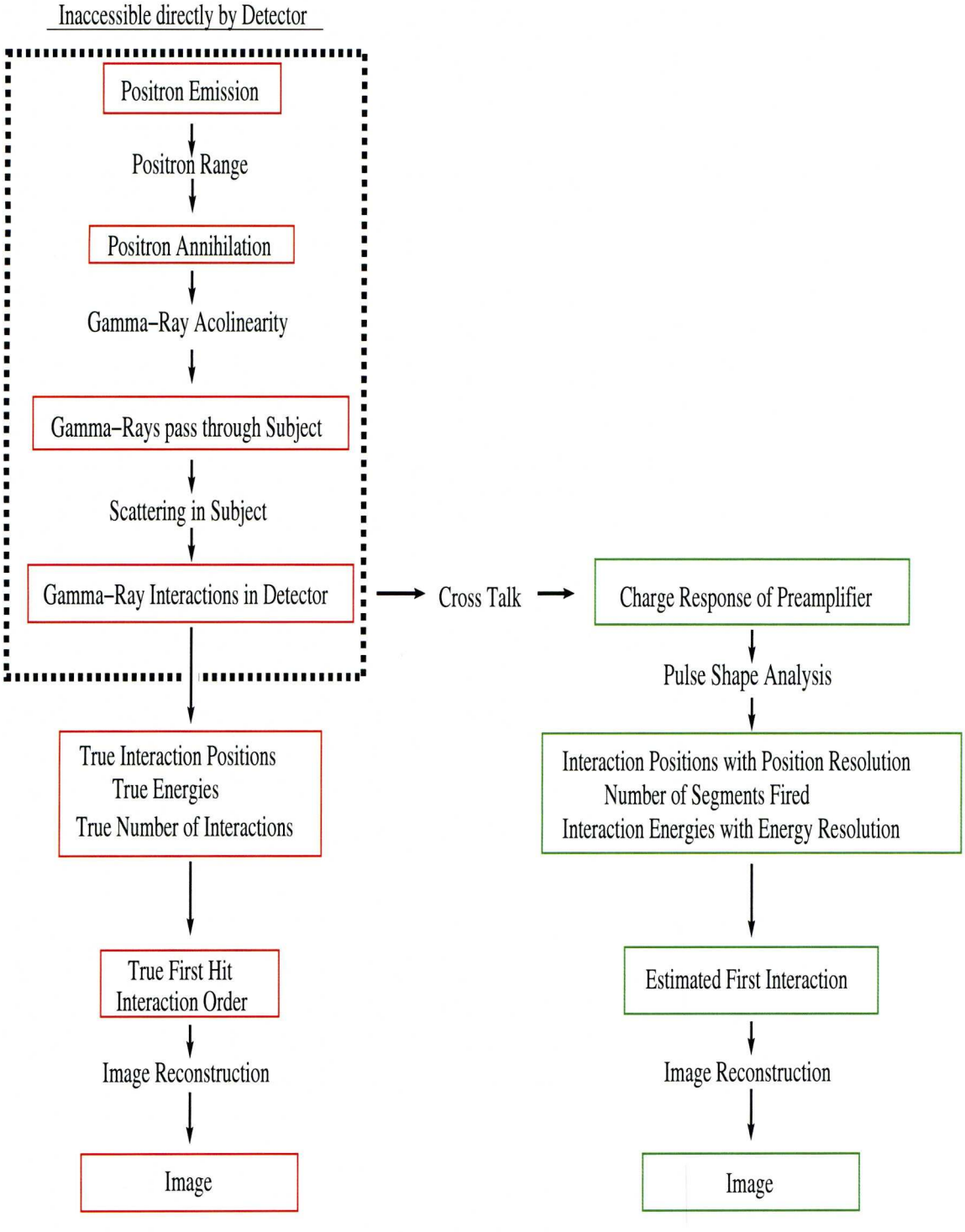

Figure 5.5: A flow diagram illustrating the events from a positron emission results in an increment in a reconstructed image. Each of these stages will add their own image distortion. Many are only accessible through simulated data.

5.5.1 Sources of Experimental Uncertainty

The uncertainties studied in this work are categorised and listed below:

- Physical sources

  The positron range

  The acolinearity of the annihilation photons

- Detector and Hardware

  Position resolution of the detector (x-z)

  Depth of Interaction (DOI) resolution of the detector (y)

  Identifying the correct event order

  Convolution of multiple interactions within one voxel

  False definition of a line of response

These uncertainties shall be systematically, and separately, imposed upon the simulated data. This is interesting for several reasons: firstly, it is valuable, from a fundamental point of view, to quantify their impact on image quality, secondly it is essential for the future of the SmartPET project to understand the limitations in the current system and thirdly building upon these limitations, it will be necessary for future experimental work to predict a realistic limit upon the performance of the SmartPET imaging device. Biological uncertainties e.g. patient movement (conscious or subconscious) and dispersion of the radioisotope shall not be studied in this work. Conscious, *short and sharp* (e.g. sneezing) patient movement can be responsible for shifts of up to 6 mm [Eis88], while respiratory motion has been quantified to move the patient by between 14 mm - 18 mm in [Osm03].

5.6 Quantifying Imaging Limitations

5.6.1 An Idealistic Simulated Image

The simulated data were reconstructed into an image with no physical or experimental distortions added. Although experimentally unachievable, this should infer the intrinsic limit of the reconstruction algorithm. However, the input stage for the reconstruction algorithm, the sinogram, Section 5.2.2, requires a finite number of divisions. Therefore, a bin size of 0.1 mm was selected. A finer level of resolution would have been ineffectual due to the pixel size in the image. No kinetic energy was assigned to the positron, in order to rule out the contribution from its range. The first interaction in both detectors was selected to ensure the LOR definition was always correct. No scatter material was simulated around the source. Figure 5.2 presents this "perfect" image, distorted only by the intrinsic limit of the reconstruction algorithm. It illustrates how the algorithm is sufficiently powerful to reconstruct LORs to an accuracy of one pixel of image space ($\frac{60\,\mathrm{mm}}{256} \times \frac{60\,\mathrm{mm}}{256} = 0.23\,\mathrm{mm} \times 0.23\,\mathrm{mm}$). These dimensions are exceeded by the size of an experimental point source ($\approx$ 0.5mm). This implies that the reconstructions should not be limited by the imaging algorithm.

5.6.2 Physical Distortions

Physical distortions are attributed to the positron-electron annihilation as seen in Figure 5.6. Specifically, these include the distance travelled by the positron before it annihilates (*positron range*) and the *acolinearity* of the produced γ rays.

The Positron Range

The β^+ reaction which results in a positron emission is described by

$$ {}^{A}_{Z}\mathrm{Mother} \rightarrow {}^{\mathrm{A}}_{\mathrm{Z-1}}\mathrm{Daughter} + \mathrm{e}^{+} + \nu_{\mathrm{e}} + \mathrm{Q}_{\mathrm{value}}, \tag{5.8} $$

where the Q_{value} is the kinetic energy liberated by the reaction. Following its creation in and emission from the Coulomb field of the mother nucleus, the positron undergoes

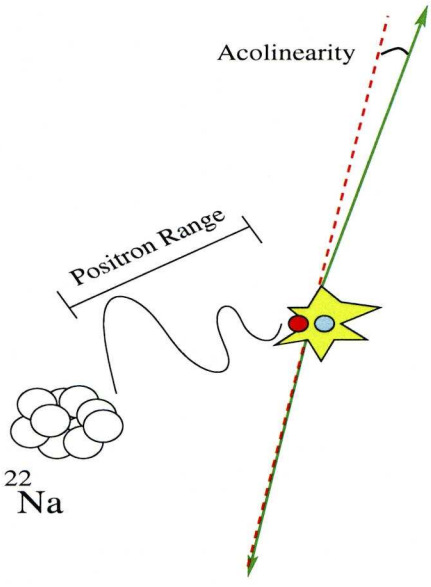

Figure 5.6: A schematic diagram of the positron-electron annihilation highlighting the two physical operations resulting in image distortion.

numerous elastic scatter reactions before annihilating with an electron. This process is termed *thermalisation* as the positron slows down to reach thermal energies. The positron range depends upon the density of the surrounding material and the kinetic energy with which the particle was emitted. Although the decay of a radioisotope has a constant Q_{value}, the kinetic energy of the positron is non-constant, as it shares this Q_{value} asymmetrically with a neutrino (ν_e) according to

$$Q_{value} = T_{e^+} + T_{\nu_e}, \tag{5.9}$$

where T_{e^+} and T_{ν_e} are the kinetic energies of the positron and the neutrino respectively. The maximum possible energy assigned to the positron is therefore the full Q_{value} and is referred to as the *beta end-point energy (β_{End})*. For ^{22}Na, the kinetic motion of the positron was modelled according to the probability vs. energy distribution in Figure 5.7(a). The spectrum reproduces the positron-neutrino energy sharing for a ^{22}Na source, with a beta end-point energy of $\beta_{End} = 545\,\text{keV}$. The frequency distribution in the y-axis is produced using a characteristic Bethe equation

$$P(E) = \frac{E^{\alpha}(1-E)^{\beta}}{\int u^{\alpha}(1-u)^{\beta}du}, \tag{5.10}$$

where $P(E)$ is the probability of an energy, E, being assigned to the positron and α and β are shaping parameters. The denominator of an identical function of u is included to ensure that the total probability scales between zero and unity.

Figure 5.7(b) quantifies the effect of the positron range in ^{22}Na on image quality. The figure contains one slice through a reconstruction, where the kinetic energy of the positron has been disabled in the simulation (black). The second slice presented (red) has the kinetic energy distribution, displayed in Figure 5.7(a), assigned to the positron. Both reconstructions contain 18 million events, emitted from a point source of positrons into a 3x3x3 cm cube of polythene (CH_2). To avoid overlap between the two slices, the source which included the positron range was positioned 2.5 mm further to the left. Although the γ-ray acolinearity will be discussed more thoroughly in Section 5.6.2, it is not possible to study the two phenomena in complete isolation. The acolinearity will also contribute to the width of Figure 5.7(b) (red), but not to Figure 5.7(b) (black). It can be stated that the combined effect of the energy emission spectrum in Figure 5.7(a) and the γ-ray acolinearity results in the minor image distortions presented above. The beta end point energy in ^{22}Na is sufficiently low that the distance travelled by the positron does not impact significantly on the peak width. The FWHM is quantified at 0.4 mm for both images. The difference is clearer in the FW.1M measured at 0.9 mm and 0.7 mm for the image with and without the inclusion of positron physics. Although some difference is observed in Figure 5.7(b), the effect is deemed negligible for ^{22}Na at this image resolution. A selection of some of the most commonly utilised PET isotopes are presented in Table 5.2. Positron emitting point sources with these β end point energies were also simulated to evaluate their impact on image quality. The modelled probability vs. energy distributions are displayed in Figure 5.8(a). The shaping parameters α and β were varied to reproduce the spectra published in [Lev99] and [Alb08]. The reconstructions of these sources, along with one-dimensional slices through the highest bin entry, are presented in Figure 5.8. The images were normalised to align all slices in height to the ^{11}C slice. The figure

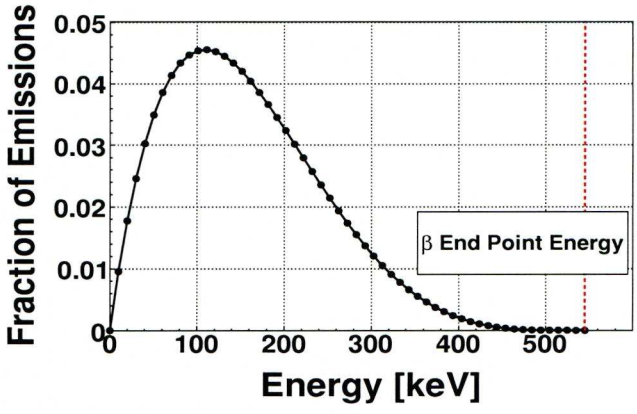

(a)

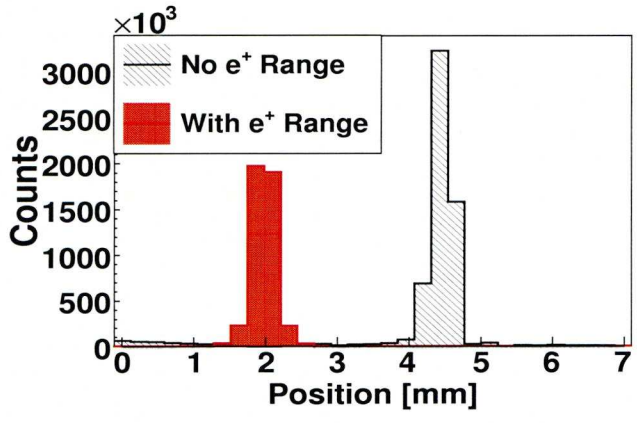

(b)

Figure 5.7: (a) A model of the kinetic energy assigned to the positron for a ^{22}Na source. The probability of the positron being emitted with a kinetic energy is defined by the plotted distribution. The beta end-point energy is 545 keV. (b) A slice through both the "perfect" image with no experimental or physical distortions included (black) and the reconstruction where the kinetic motion of the positron was modelled (red). The two sources were deliberately offset to aid the reader.

Isotope	Half-Life [mins]	β_{End} [keV]	FWHM [mm]	FW.1M[mm]
^{22}Na	2.60*	545	0.4 (2)	1.4 (2)
^{18}F+	109.74	650	-	-
^{11}C	20.39	970	0.4 (2)	2.3 (2)
^{13}N	9.97	1190	0.4 (2)	2.8 (2)
^{15}O	2.22	1720	0.7 (2)	4.5 (2)
^{68}Ga	67.63	1899	0.7 (2)	4.8 (2)
^{94m}Tc	52.0	2438	0.9 (2)	7.0 (2)

* Quoted in years.

+ ^{18}F was not modelled due to its similarity to ^{22}Na.

Table 5.2: Table of the most commonly utilised PET isotopes and their decay properties. The effect of the positron range has been quantified by measuring the FW.1M.

highlights how the majority of the distortion introduced due to the positron range is at the base of the reconstructed slice. Only at sufficiently large β_{End} values (over 1 MeV) is the FWHM effected. This illustrates that, despite the long distance travelled by higher energy positrons, their multiple scatters prohibit the majority of them from annihilating at large net displacements from the emission point. Instead, they scatter around the emission point in three dimensions. Similar observations were made in [Der86a] where the annihilations with a large separation from the source were established as a low frequency distortion and reduced using Fourier analysis. The FWHM and FW.1M of the various isotopes are summarised in Table 5.2. The measurements are largely consistent with available literature [Lev99].

Gamma Ray Acolinearity

The γ-ray acolinearity arises due to the non-zero momentum of both the positron and the electron when entering the annihilation reaction. Any momentum of the reacting particles must be carried forward to the produced photon pair. Therefore, in realistic experimental scenarios the 180 ° degree (back-to-back) assumption is inaccurate by up to 0.25° degrees

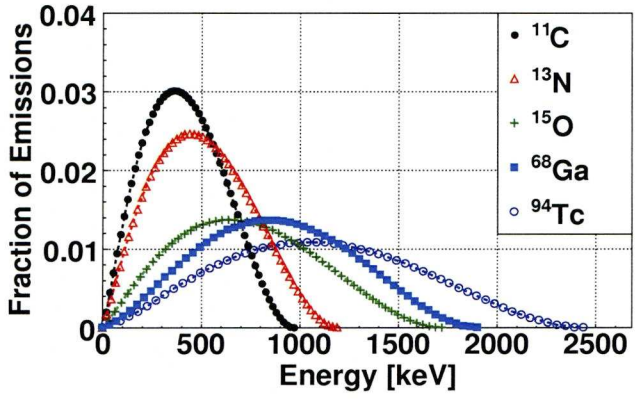

(a)

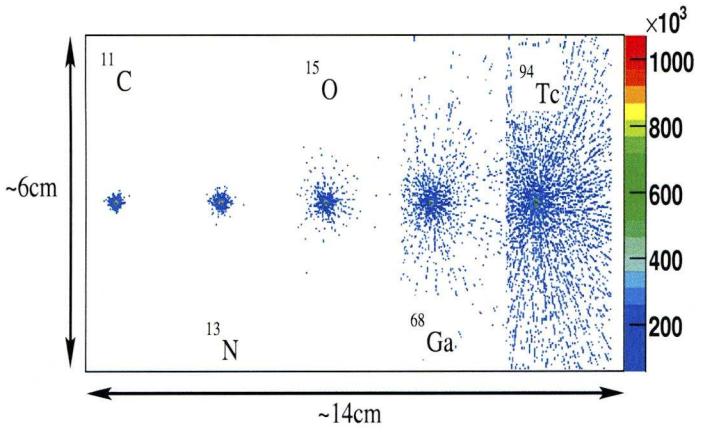

(b)

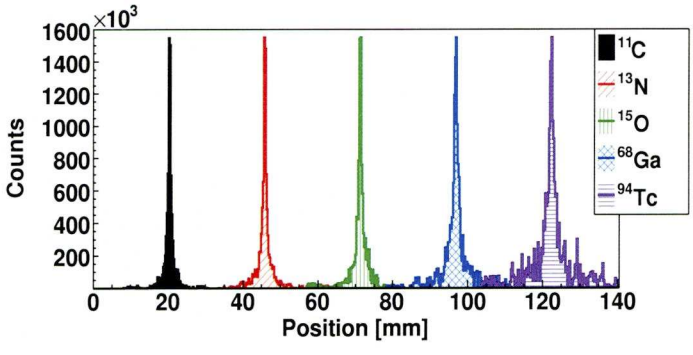

(c)

Figure 5.8: (a) The kinetic energy spectra assigned to the positrons from different PET isotopes. (b) Reconstructions of the different positron emitting isotopes modelled. As the positron range increases, the quality of the reconstructed image is clearly compromised. (c) Slices through the reconstructions in (b) to visually highlight the FWHM and FW.1M of the reconstructions. The measurements of these parameters are summarised in Table 5.2.

[Der86b]. The effect of the γ-ray acolinearity on image quality is understood to increase with detector separation at a rate of approximately 28 μm/cm [Hof86]. This would predict an effect of approximately 0.364 mm for the current SmartPET configuration, which is consistent with the reconstructions in Figure 5.7(b).

5.6.3 Scattering within the Subject

When one, or both, of the 511 keV γ rays Compton scatter in the imaging subject, the defined LOR does not include the true point of positron-electron annihilation (Section 2.6). Independent of the detector system and the physics of the positron, the probability of the γ rays Compton scattering within the imaging subject depends on the thickness and density of the subject material. In scintillator based PET, the stopping power of the crystals is sufficiently high that a full energy photopeak absorption can be demanded in both detectors. This procedure, referred to as *photopeak gating*, rules out any significant scatter within the subject[3]. Due to the lower stopping power of some semiconductors, particularly germanium and silicon, this photopeak requirement can rarely be met as the γ rays often only deposit a fraction of energy in the detectors (81 % at 511 keV and 2 cm thickness of HPGe). In addition to solid angle limitations, this is a further reason why the main application of semiconductors in PET is in small animal imaging. The reduced volume of the imaging subject results in a much lower scatter fraction.
The amount of scattering within the subject was investigated by surrounding two opposing 511 keV γ-ray beams (as in the above Section 5.6.2) with a sphere of water. These were then absorbed in an artificially large and dense detector material to register all γ rays which exit the sphere.

Several scenarios were modelled, with the radius r ranging in integer steps from one to five centimetres. For each geometry 100,000 pairs of γ rays were emitted. Figure 5.9(a) is a spectrum of the energy of the γ rays entering the detector, before their interaction. Inaccessible experimentally, this quantity depicts how the majority of γ rays still enter the detector with their full 511 keV energy. It is observed, that the peak-to-total ratio

[3]Some small angle scatters may remain undetected due to the poor energy resolution of the scintillator.

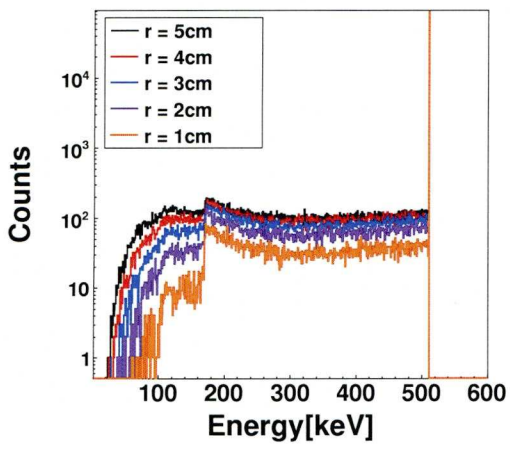

(a) Energy when entering the Detector

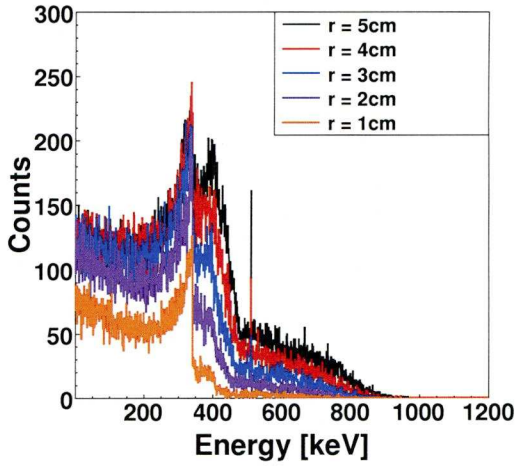

(b) Energy deposited in the Subject

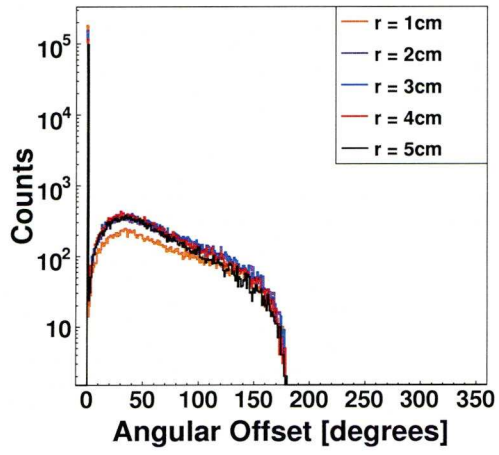

(c) Angular Offset from 180°

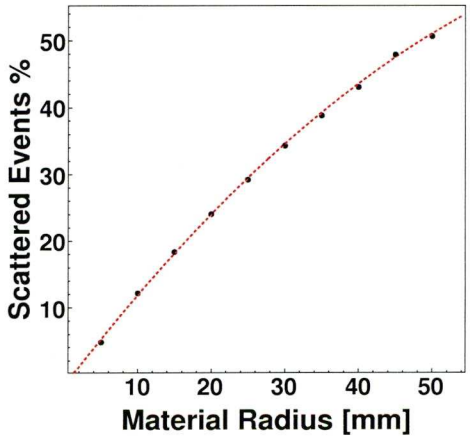

(d) Fraction of Scattered γ Rays

Figure 5.9: (a) histograms the energy with which the γ ray entered the detector after leaving the scattering material. (b) depicts the amount of energy deposited in the scattering material by both back-to-back γ-ray beams for a range of radii of scattering material. At large radii a photopeak absorption peak appears signalling some fully attenuated γ-rays in the material. (c) is a histogram of the angle with which the "back-to-back" γ-rays differ from 180° after passing through the scatter material. The same spectrum is plotted for subject material of different radii. (d) is a plot of the fraction of scattered γ rays. The slight saturating trend occurs as only γ rays which reach the detector have been included and attenuation takes effect at larger radii.

diminishes slightly with scatter thickness. To produce Figure 5.9(b), the modelled sphere of water acted as a detector and the energies, which were deposited in the water, are detailed in the figure. A distinct Compton edge and a slight 511 keV photopeak at larger radii as some γ rays are fully attenuated, are visible. For large radii, the deposited energy extends beyond the 511 keV photopeak as energy was deposited by both γ rays. The angular offset caused by an energy deposit in the subject has been registered in Figure 5.9(c). The majority of events do not show any offset, yet the log scale highlights the angular continuum obtained. Figure 5.9(d) illustrates the percentage fraction of γ rays, which deposit any energy in the subject before interacting in the detector. A quadratic fit (red) was performed to emphasise the trend. It can be deduced from the figure that the scatter fraction for small animals (with a radius of $\approx$<3 cm) is $\sim$30% if no energy condition is placed on the detected γ ray energies. This result is consistent with clinical literature [Blo95].

5.6.4 Position Resolution in the Detector

The three-dimensional position resolution of the detector was separated into *lateral* position resolution (parallel to one set of strip segmentation lines) and *depth of interaction* (*DOI*) position resolution (perpendicular to both strip segmentation lines). The dimensions implied by the term lateral and depth of interaction is illustrated in Figure 5.10. This distinction was made for two reasons: firstly existing scintillator PET cameras have significant difficulty in obtaining reliable depth information. For a ring geometry, at positions increasingly far from the centre of the field of view, this results in a parallax error when defining the line of response. The depth of interaction is a criterion on which semiconductor PET can show major improvements, it is therefore interesting to examine the depth dimension in isolation; secondly, in planar germanium detectors the lateral position and the depth position are obtained through different analysis procedures. The fact that they potentially have non-equal limitations is an additional argument for decoupling the dimensions.

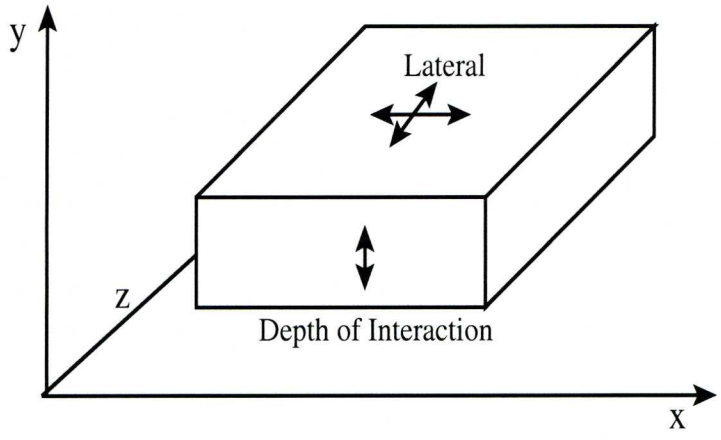

Figure 5.10: A depiction of the dimensions of position resolution and the axis labelling scheme applied.

Lateral Position Resolution

The effect of the lateral resolution of the detector was investigated by reconstructing sinograms, where the detector had been segmented to a variety of resolution levels. In SmartPET, voxels of 5 mm x 5 mm x 20 mm are defined by raw granularity. These levels were enhanced in [Mat06, Coo09] through application of parametric PSA algorithms to obtain a lateral position resolution of $\approx 1\,\mathrm{mm}^2$.

The effect of improving the lateral spatial resolution is displayed in Figure 5.11. A linear relationship is observed between the FWHM and lateral spatial resolution which holds down to the sub-millimetre level. Although the SmartPET detectors are unlikely to achieve sub-millimetre resolution of this description (see Chapter 6), this implies that the intrinsic limitation of the reconstruction algorithm is not reached until this degree of resolution. It also indicates that opting for a system with high and reliable lateral spatial resolution is crucial to high resolution PET imaging.

Attaining such position resolution in a semiconductor detector is not straight forward. The most direct means of achieving high spatial resolution is to segment a detector into a large number of small pixels or strips. This route is inherently linked to high cost due to the implementation of each channel with digital readout electronics. Additionally, even

neglecting the expense of the system, smaller detector segments increase the likelihood of charge sharing at segment boundaries [Coo08]. Although this effect could be modelled and corrected for it serves as an example of the complications of small segment size. A second option is to implement larger segments, avoiding the cost of a large number of readout channels and charge sharing issues, and use PSA techniques to retrieve spatial information. The PSA techniques introduce their own uncertainties discussed in Chapter 6. To conclude, although high lateral spatial resolution must be made a priority in any small animal PET scanner, achieving such resolution can be challenging. The most straight forward route to high spatial resolution is the implementation of many small, isolated detector segments. Unfortunately, this option is also the most expensive. This issue shall be discussed further in Chapter 7.

Depth of Interaction Resolution

The depth at which a γ-ray interaction occurs in the detector is a subject of much discussion in clinical scintillator PET [Tai05]. The inability of the scintillator to identify this

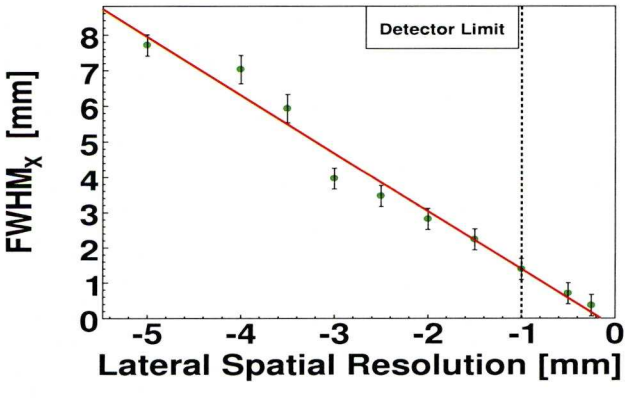

Figure 5.11: A depiction of the FWHM of a reconstructed point source as a function of lateral position resolution. The linear and steep trend emphasises the direct link between lateral spatial resolution and high resolution images. The vertical line indicates the level of lateral resolution currently achievable using the SmartPET system.

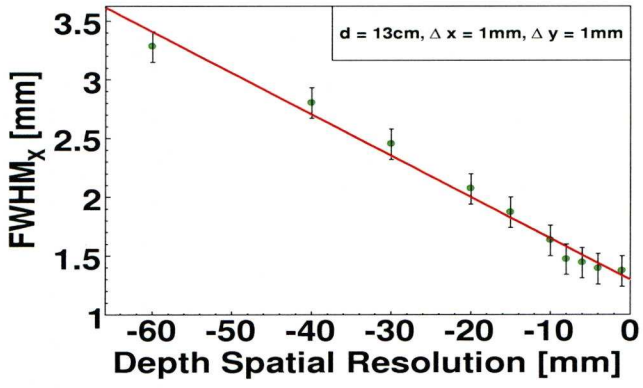

Figure 5.12: A plot of the image resolution as a function of DOI resolution. The initial linear increase with depth sensitivity plateaus between ~10 mm and ~5 mm. This implies that the benefit of DOI resolution on the LOR definition becomes saturated in the sub-centimetre range. The reader is referred to the text for further details.

interaction dimension introduces a significant parallax error, especially toward the edge of the field of view. More modern PET systems address this problem by employing multiple crystal layers [Rol07]. In a semiconductor detector, a three dimensional interaction localisation is performed based upon pulse shape analysis (Chapter 6). The influence of the depth of interaction uncertainty on image quality of a point source reconstruction has been modelled. Measurements extended beyond the 20 mm depth dimension of SmartPET up to 60 mm to include the effect for systems with thicker scintillator detectors. Figure 5.12 is a plot of the image resolution as a function of depth resolution. These reconstructions were obtained with a 1 mm lateral position resolution in the remaining two dimensions and a detector separation of 13 cm. The trend of these values highlights an initial linear increase with improving depth resolution which plateaus ~5 mm.

Figure 5.13 presents slices through images reconstructed with different depth sensitivity. The plateau effect is highlighted by minimal observed differences between the slices with 4 mm (red) and 1 mm (blue) depth resolution. The plateau is believed to be a result of the 1 mm depth resolution having little impact on lines of response defined across the 13 cm separation between the two detectors. This implies that, in system design, it is

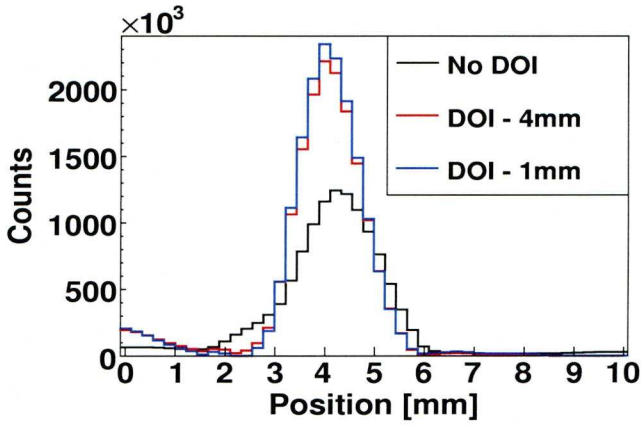

Figure 5.13: Slices through the reconstructions with different levels of depth sensitivity. The slices illustrates how the difference between the reconstructions with 1 mm (blue) sensitivity and 4 mm (red) sensitivity are minimal.

important to have some depth of interaction sensitivity down into the millimetre region, yet sub-millimetre depth of interaction resolution may not be fruitful.

5.6.5 Interaction Clustering

Due to the aforementioned mediocre stopping power of germanium (Section 3.3), multiple interactions will commonly occur within the same detector pixel. Therefore, the true number of interactions (N) cannot be established by counting the number of fired segments. Instead, more intensive analyses of the leading edge of the pulse shape must be performed (Chapter 6). In order to model and quantify the effect of this phenomenon on image quality, multiple interactions, if present, have been replaced by their energy-weighted barycentre, calculated according to

$$P_T = \frac{\mathrm{E_1}}{\mathrm{E_1 + E_2 + ... E_N}} * P_1 + \frac{\mathrm{E_2}}{\mathrm{E_1 + E_2 + ... E_N}} * P_2 + ... + \frac{\mathrm{E_N}}{\mathrm{E_1 + E_2 + ... E_N}} P_N, \quad (5.11)$$

where the interactions P_1 - P_N are the individual interactions depositing energies E_1 - E_N in the segment. $\mathrm{P_T}$ is the vector of the weighted barycentre where the total energy $E_T = \sum_{i=0}^{N} E_i$ is deposited. The application of this interaction clustering formula shall

be referred to as *packing* or *clustering*. For this analysis, the volume in which the interactions were clustered was the volume of one voxel of 5 mm x 5 mm x 20 mm. The effect of this phenomenon on image quality was quantified for fold <1,1,||1,1> data. An image distortion of ~0.2 mm was introduced through packing resulting in a measured FWHM of ~1.4 mm. In an experimental data set, this value may be higher due to the effect of the convolved interaction on the accuracy of the PSA routine. This issue shall be addressed in parts in Chapter 6.

5.6.6 Varying the Detector Separation

The simulations discussed above were repeated with the two SmartPET detectors separated by reduced distances ($d_{Sep} = 11,9,7,5$ cm) to investigate the dependence of the above parameters on the detector separation. Figure 5.14 presents the image resolution of a reconstructed point source with different distortions included as a function of detector separation. The x-axis has been negated, to allow the reduction in separation to flow from left to right.

The figure illustrates that the majority of the included effects remain constant within errors as d_{Sep} is reduced. This implies there should be no decrease in image quality if the detectors are brought closer together experimentally. Previously [Mat06, Coo09], the detector separation was maximised as only parallel and near-parallel LORs were to be utilised in image reconstructions. The large separation reduced the error in treating near-parallel LORs as parallel. With the ability to use non-parallel LORs developed in Section 5.3.3, experimental data can be acquired at lower separations. The increased solid angle coverage raises the overall efficiency of the SmartPET system. As determined through the simulations, at 13 cm the total imaging efficiency is 0.022% of all source emissions. This number increases by a factor of ~10, if the detector separation is reduced to 5 cm. With regard to image quality, the only points indicating a trend are those corresponding to images with no depth of interaction (DOI) information (open circles). Although the values all pass a consistency check, a successive rise is present, implying a linear dependence on detector separation. This is understood to occur for the same

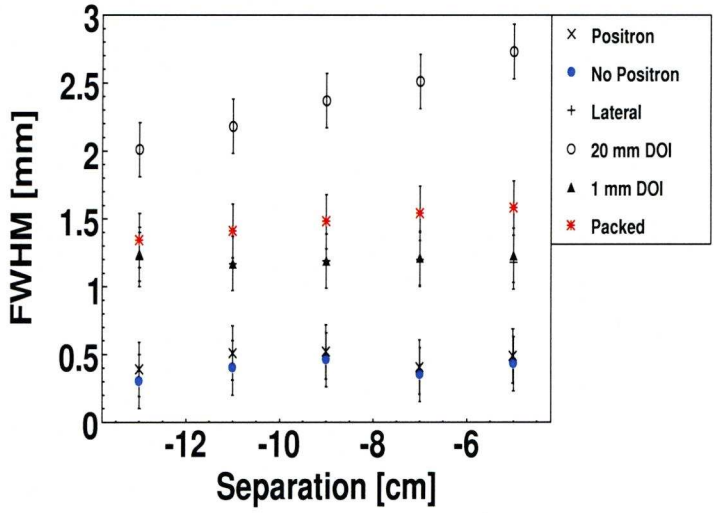

Figure 5.14: A plot of FWHM for various distortion parameters added as a function of detector separation d_{Sep}. The x-axis has been negated to permit the separation reduction to read from left to right.

reason as the plateau in Figure 5.12. The impact of an error of up to 10 mm in depth on a LOR increases for trigonometric reasons as the detectors are brought closer together. If the LOR is considered as a vector, it will consist of a lateral- (x) and depth-component (y). The depth component of a LOR is defined as $d_{Sep} + \mathrm{DOI}_{SP1} + \mathrm{DOI}_{SP2}$. The greater the magnitude of d_{Sep} is, the more it dominates the depth-component of the LOR and the more negligible the error on the remaining terms becomes. For d_{Sep}=5 cm an uncertainty of up to 10 mm on the depth-coordinate of the interaction positions therefore has a greater detrimental effect on image quality than at d_{Sep}=13 cm.

5.6.7 First Hit Identification

Due to the lighter Z of the material, the likelihood of multiple γ-ray interactions in the detector is increased in silicon and germanium over a denser scintillator. For a defined LOR to contain the positron annihilation point, the first interaction must be correctly identified. The determination of the first hit is made ever more crucial by the longer

mean free path of the γ rays in lighter Z materials increasing the separation between interactions. This means an erroneous LOR definition has more dramatic implications on image quality. The effect of the correct identification on image quality is studied below and various methods of determining the first hit are explored. A γ-ray tracking algorithm has also been developed using the SmartPET model. Its performance and accuracy has been investigated.

Producing data sets with multiple first hit candidates in one detector

To accentuate the effect which the presence of multiple first hit candidates has upon image quality, simulated data were pre-selected that consisted of events where

- one detector registered an interaction on only one strip in both detector faces
- the other detector registered two strips firing on both of its detector faces.

This pre-analysis step was performed as the fraction of fold <1,1||1,2> events is otherwise small compared to the fold <1,1,||1,1,> events (15%) and any benefit or reduction in image quality may go unnoticed.

Identifying the First Hit Based on Energy

The assumption that the interaction, which deposited the most energy, was the first hit led to a correct first hit identification accuracy of 59 %. Figure 5.15 displays a reconstruction of the fold <1,1||1,2> gated data, where the first hit was correctly established using information from the simulation, while Figure 5.16 utilised the above discussed energy based assumption. The difference in the FWHM and FW.1M are clearly visible. The FWHM increases from 1.39 mm in Figure 5.15 to 2.28 mm in the assumption based reconstruction. The FW.1M equate to 2.58 mm and 4.22 mm for the ordered and energy assumption based reconstructions respectively. The ratio of FWHM/FW.1M is constant within errors at ~0.54 for each reconstruction and shall be calculated to monitor any change in the Gaussian shape of the point source. This information is summarised in

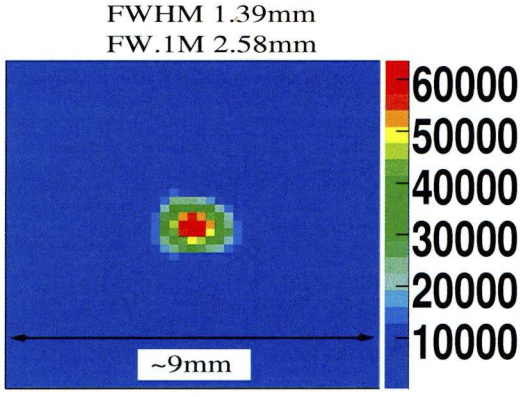

Figure 5.15: A reconstruction of a point source using only fold<1,1||1,2> events where the first hit was correctly identified by obtaining the interaction order from the simulation.

Table 5.3, where the Efficiency column refers to the fraction of the fold <1,1||1,2> data subset that different event ordering methods were applicable to.

Identifying the First Hit Based on Depth

The Klein-Nishina distribution (Equation 3.4 displayed in Figure 3.2) indicates that γ rays with an energy of the order of 511 keV have higher probability of scattering forward, than in any other direction. Due to this behaviour, the interaction, which has a shallower position in the crystal, has an increased chance of having occurred first. A reconstruction performed, based upon this assumption, is presented in Figure 5.17. The first hit identification accuracy was reduced to 52 % for these data and the FWHM and FW.1M were measured to be 2.38 mm and 4.45 mm respectively. The ratio between these metrics has remained unchanged inferring that the general shape of the peak has not been affected. With the accuracy barely above a random choice of first interaction, a more sophisticated method must be derived.

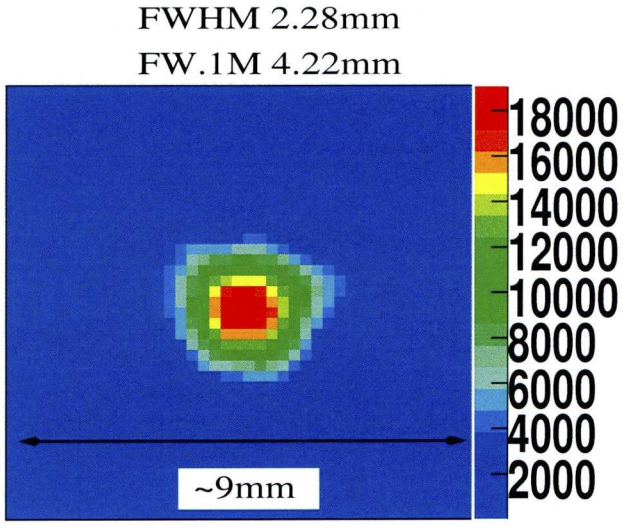

Figure 5.16: A reconstruction of a point source using only fold<1,1||1,2> events where the interaction depositing most energy was assumed to be the first hit.

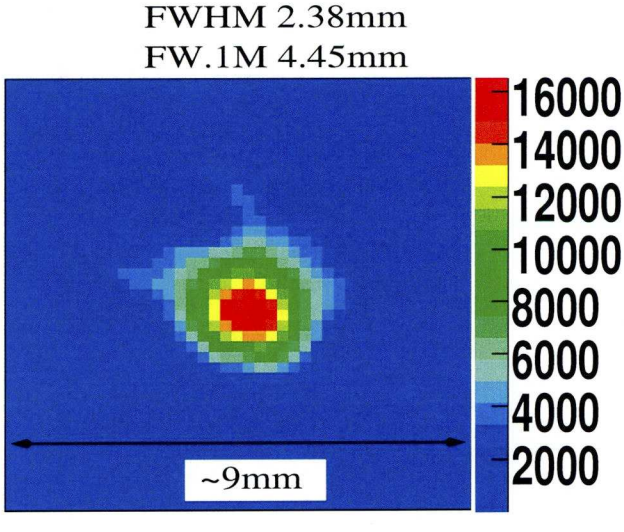

Figure 5.17: A reconstruction of a point source where the shallowest γ-ray interaction was used in LOR definition.

5.6.8 Gamma-Ray Tracking

Gamma-ray tracking algorithms have been under study for nuclear physics applications throughout the last decade [vdM99, Sch99, vdM02, Mil03, Lop04]. These have developed the ability to track γ rays throughout a 4π geometry of a next generation array such as AGATA [Sim06] and GRETA [Bea03]. However, some of the assumptions, utilised in these works, do not hold for PET analysis. The algorithms presented in [vdM99, vdM02, Mil03] are *back-tracking* algorithms based around determining the final interaction and reconstructing the γ-ray path in inverse chronological order. The last interaction can be identified as it often deposits least energy and fulfils an energy restraint (e.g. E_{last} <90 keV) [Lop04]. This initial assumption is based upon full absorption of the γ ray within the germanium shell and a final photoelectric absorption. Furthermore, the higher initial energy (of the order of 1 MeV) ensures higher energy deposits are likely to happen first. In SmartPET, these assumptions cannot be made. The full absorption of the γ ray does not occur in a majority of cases, therefore an adopted and simplified version of a forward tracking algorithm (e.g. [Sch99, Lop04]) has been developed and applied.

Algorithm Structure

The tracking algorithm is applied to the simulated data after adding Gaussian blurring on all three dimensions of the position coordinate and the energy deposit. Furthermore, the data have been clustered according to Section 5.6.5. In Figure 5.18, the methodology behind the simplified forward tracking algorithm is displayed, through a schematic diagram of a fold <1,1||1,2> event. The single interaction (fold<1,1>) in one detector (SmartPET2 in Figure 5.18) acts as a starting point for the γ-ray track. In the other detector (SmartPET1 in Figure 5.18), two interactions remain as potential candidates for a first hit. A vector $\vec{a}$ is defined connecting this single site interaction with one of the two interactions. An additional vector $\vec{b}$ links the two first hit candidates in SmartPET1. Using the scalar product, the angle between $\vec{a}$ and $\vec{b}$ is determined. This angle is then converted into an energy based upon inverse Compton kinematics and the assumption that the incident γ ray energy was 511 keV to produce a *geometrically obtained energy.*

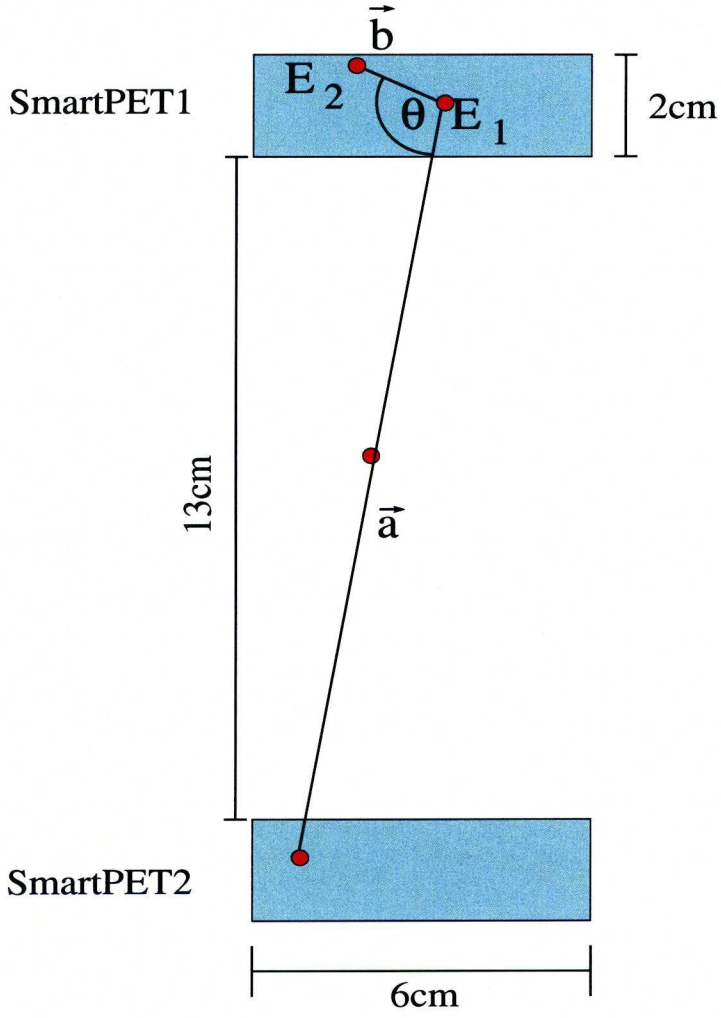

Figure 5.18: A cartoon illustration of the process by which the correct LOR is identified using γ-ray tracking. A single site interaction must be available in one detector to function as a starting point. Using vectors and geometrically obtained angles, the most likely γ-ray path is identified.

This geometric energy is compared with the detected energy at that point (E_1 in the figure) to act as a confidence parameter for this track iteration. The interaction order is then reversed, and the process repeated, to calculate a figure of merit for the opposing track starting with the other first hit candidate (E_2 in the figure). The figure of merit is calculated by taking the absolute difference between the experimental and geometric energies. If neither, or both, geometrically obtained energies (from the first and second iteration) lie within a 35 keV energy gate of the detected energy, the event is rejected. However, if the algorithm results in a unique solution, where one interaction has a much closer match to the expected energy, this interaction is defined as the first hit.

Algorithm Performance

The algorithm produced a unique solution in only 43 % of cases. However, of these 43 %, the first hit was correctly identified 86 % of the time. Reconstruction of a point source applying this method produces a FWHM of 1.81 mm, depicted in Figure 5.19(a). In order to overcome the efficiency deficit, an image was also produced, where the shallowest hit was declared the first hit if the tracking method was inconclusive. This reconstruction is presented in Figure 5.19(b) and has a FWHM of 1.98 mm. The ratio between FWHM and FW.1M has not diverged outside of consistency throughout application of the tracking approaches.

First Hit Used	FWHM [mm]	Efficiency [%]	Accuracy [%]
Correct	1.39	100	100
Most Energy	2.28	100	59
Shallowest	2.38	100	52
Tracking	1.81	56	81
Tracking with Shallow	1.98	100	65

Table 5.3: A summary of the performance of the γ-ray tracking algorithm when applied to fold <1,1||1,2> data.

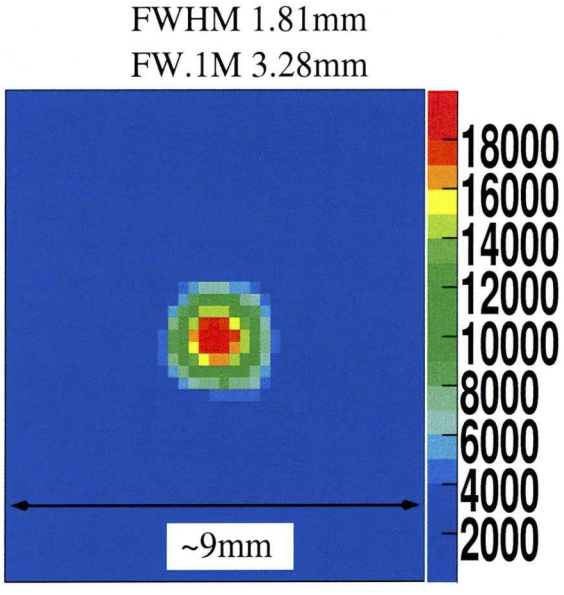

(a) Tracked events only

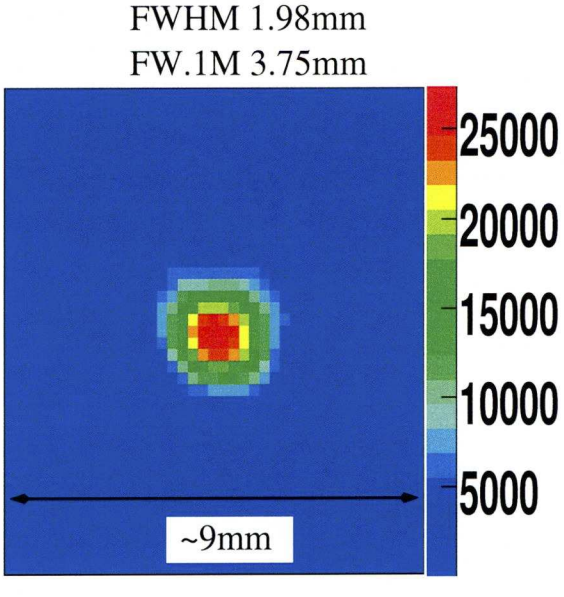

(b) Tracking and Klein-Nishina

Figure 5.19: (a) A reconstruction of a point source using fold<1,1||1,2> data where the tracking algorithm was applied to identify the first hit. The data were only included in the reconstruction if the tracking algorithm produced a unique solution. The FWHM is 1.81 mm, a significant improvement on the single parameter based first hit identification methods discussed above. (b) A reconstruction of a point source using fold<1,1||1,2> data where the tracking algorithm was the primary means of identifying the first hit. If a

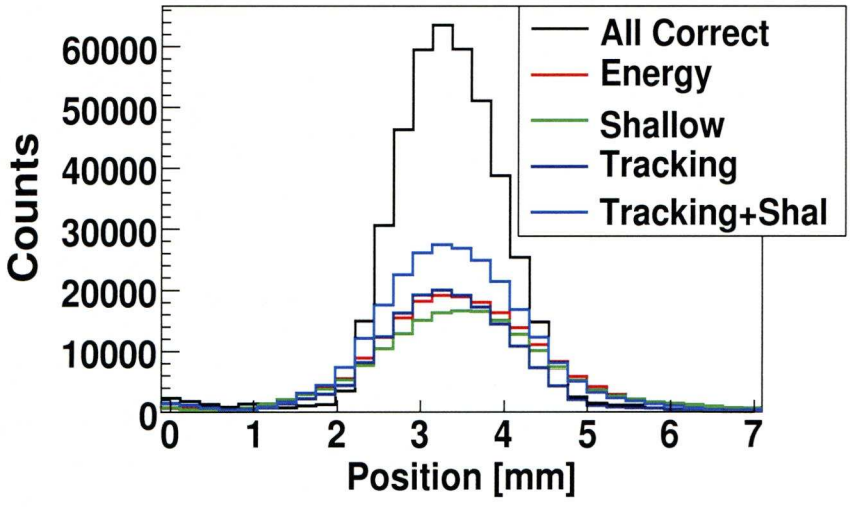

Figure 5.20: Slices through all five discussed point sources reconstructions using the different methods of identifying the first hit. The figure illustrates the improvement achieved by employing the γ-ray tracking algorithm to establish which interaction occurred first.

The Klein-Nishina method was chosen as the alternative to the tracking algorithm as the most likely causes of inability to track the γ ray originate from issues regarding the energy parameter. The two main responsible processes are: scattering within the subject matter, in which case the assumption of an incoming 511 keV γ ray is invalidated; and/or the clustering of interactions within a detector voxel (Section 5.6.5). Although the clusterisation of the interactions within a segment had a reduced direct effect on the reconstructed image, as the distance between interactions in a segment was often minimal, the error introduced by the energy summation is a major issue for the tracking algorithm - more so than the inclusion of position and energy resolution. If γ-ray tracking algorithms are to be utilised in future PET imaging applications, the ability to deconvolve multiple interactions within a segment is essential.

First Hit Used	FWHM [mm]	Efficiency [%]	Accuracy [%]
Correct	1.64	100	100
Most Energy	1.80	100	60
Shallowest	1.76	100	50
Tracking	1.68	56	86
Tracking with Shallow	1.78	100	70

Table 5.4: A summary of the performance of the γ-ray tracking algorithm when applied to fold <1,1||1,3> data.

Gamma-Ray Tracking on Fold 3 Events

The algorithm was extended to process fold three events. The methodology is as described above, except the γ-ray track includes a third event, adding more iterations, but also more parameters, to determine a correct path. The algorithm is therefore slower, yet as the third interaction is also available for comparison with the track, the accuracy increases. Table 5.4 summarises the performance of the tracking algorithm using fold <1,1||1,3> data. Although the minor variations in the FWHM follow the trend seen in the fold <1,1||1,2> (Table 5.3), it must be stated clearly that all FWHM measurements below are consistent within their uncertainties. This means that the additional data point available to the tracking algorithm increases the accuracy to the extent of any erroneously assigned γ-ray paths barely decreasing image quality. This shall be discussed further in Chapter 7.

Expanding the Algorithm to Higher Fold Events

The feasibility of applying these tracking techniques to data with higher and more complex fold combinations was investigated. For this purpose, the different fold distributions in the data are represented graphically by introducing two metrics, *fold sum* and *fold max*. The fold sum is the summation of the detected event folds on all four detector faces (e.g. <1,1||2,3> fold sum = 7). Similarly, the fold max is the highest fold registered on any

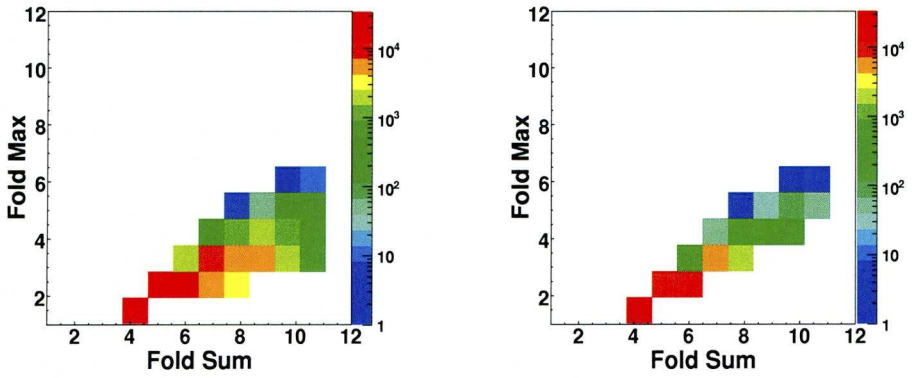

(a) Fold Distributions (b) Gated Fold Distributions

Figure 5.21: (a) a two-dimensional histogram with fold fax on the y-axis and fold fum on the x-axis for all coincident PET data. (b) the same matrix but only including event where one detector registered a fold<1,1> event. These events can be used for γ-ray tracking.

face (e.g. <1,1||2,3> fold max = 3). Figure 5.21 contains two-dimensional histograms of fold max vs. fold sum for all the data (Figure 5.21(a)). The plot highlights how the majority of the data have fold values $\leq$3.

More importantly, Figure 5.21(b) is a two-dimensional histogram of fold max vs. fold sum for the data subset where a fold <1,1> event registered on at least one of the detectors, offering the necessary starting point for the tracking algorithm. Analogous to the data in Figure 5.21(a), it is clear how the data fraction gained from tracking higher fold data is relatively low as 82% of the data lie in the fold<1,1,1,1> histogram entry. Of the remaining 18%, $\sim$80% are some combination of a fold 2 event. In summary, it can be stated that, for SmartPET, only a small data fraction is gained by including fold distributions above fold max = 3. For these reasons, the γ-ray tracking algorithm was not expanded to include higher fold combinations.

5.7 Phantom Imaging

Although PET is employed for a functional insight to the imaging subject rather than information regarding fine detail, reconstructions of complex sources - such as the *Jaszczak phantom* (Figure 5.22(d) [JAS]) - are an ideal means of testing a system's capabilities. The cylindrical Jaszczak phantom consists of four regions each filled with multiple smaller cylinders that vary in width and separation. It was designed to challenge tomographic scanners and its reconstruction often serves as a comparison between commercial systems. A range of phantoms similar in structure and varying in complexity have been simulated and reconstructed to obtain a level of the SmartPET system's potential in fine structure resolution. All phantoms embody a number of cylindrical rods, with different radii, aligned perpendicular to the tomographic rotation plane of the field of view. Reconstructions of these phantoms with all experimental deficiencies included in the reconstruction are found in Figure 5.22. The results portrayed in these figures are highly encouraging for the SmartPET imaging system. A next stage of the research will aim to reproduce these results experimentally and verify these abilities. Should this prove successful, it is believed that the SmartPET system is a worthy competitor in the commercial field of small animal PET scanners from the perspective of image resolution.

5.8 Summary

A full discussion on SmartPET's and semiconductor PET's place in PET can be found in Chapter 7, however a brief overview of the above points shall be provided here. Both the experimental measurements in [Coo09] and the simulated geometries above present highly encouraging results for the capabilities of the SmartPET system. Various sources of experimental image distortion have been quantified and the image resolutions are summarised in Table 5.5.

The criteria with the most significant impact upon a point source reconstruction are precise lateral position resolution and the accurate determination of the first interaction. Germanium detectors offer the potential to achieve sub-millimetre spatial (lateral and

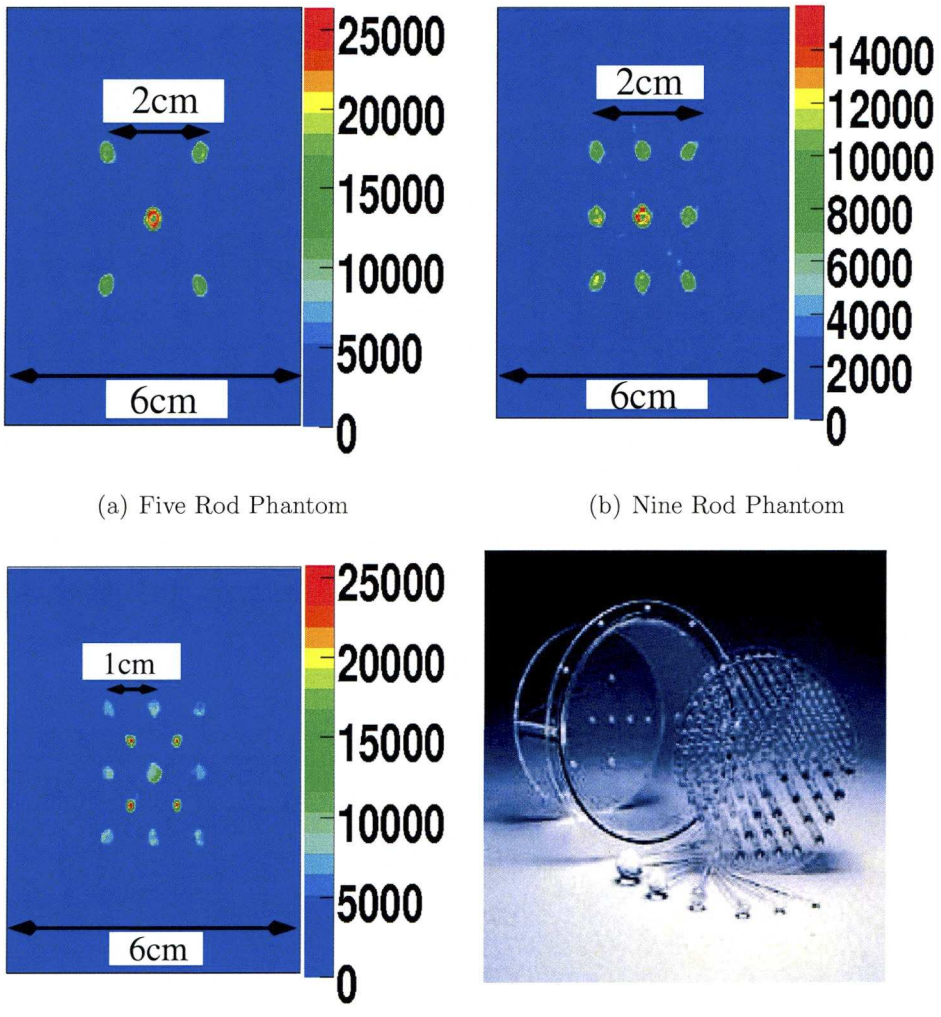

(a) Five Rod Phantom

(b) Nine Rod Phantom

(c) Thirteen Rod Phantom

(d) Jaszczak Phantom

Figure 5.22: A reconstruction of increasingly complex line source phantoms. (a) - (c) contain five, nine and thirteen cylindrical rods. (d) is a photograph of a clinically used Jaszczak phantom [JAS].

depth) resolution using pulse shape analysis techniques. The question as to whether these aims can be achieved with the SmartPET detectors shall be addressed in Chapter 6. A large image distortion arises when the effects of position resolution and event ordering are combined. Although not discussed for the modelled data, but only in Chapter 6, the

Distortion	FWHM [mm]
No Distortions	0.23
^{22}Na e^+ range	0.34
Lateral Position Resolution 1	1.21
DOI 20 mm	2.01
DOI 1 mm	1.23
Interaction clustering	1.34
Correct First Hit Identification*	1.39
Energy based First Hit Identification*	2.28
Position based First Hit Identification*	2.38
γ-Ray Tracking*	1.81
γ-Ray Tracking with Position Based*	1.98
Correct First Hit Identification$^+$	1.64
Energy based First Hit Identification$^+$	1.80
Position based First Hit Identification$^+$	1.76
γ-Ray Tracking$^+$	1.68
γ-Ray Tracking with Position Based$^+$	1.78

* Fold 2 subset

$^+$ Fold 3 subset

Table 5.5: A final summary of the effect of all introduced uncertainties on image quality.

distorted pulse shape, produced by a clustered interaction, adds significant error to the PSA routines. The interaction clustering also hampers the ability to identify the first hit using γ -ray tracking as the position and energy of the individual interactions must first be retrieved. Attempts to overcome these hindrances are made in the following chapter, but sub-millimetre position resolution will most certainly not be obtained for clustered data in the current detector design. Small animal PET will require a system which consistently, and reliably, produces millimetre or sub-millimetre position resolution in its detectors and allows a clear identification of the first hit. This could occur either with a dense material, ensuring only one interaction, or using a light material, encouraging many scatters, and

easing γ-ray tracking. Whether the sensitivity of the SmartPET pulse shapes is sufficient to overcome these obstacles, shall be addressed in the following chapter.

Chapter 6

SmartPET Detector Characterisation

6.1 Motivation

As discussed theoretically in Section 3.3.3, the charge signature produced by a semiconductor detector is highly sensitive to the precise location of a γ-ray interaction. Thorough analysis of the induced pulses allows the enhancement of spatial resolution, beyond the granularity of the device. To reliably study the relationship between pulse shape characteristics and an interaction site, the following conditions must be met:

- the interaction position must be controlled and known,
- the pulses must contain a low or zero noise component,
- the charge response must be induced by a single γ-ray interaction.

For obvious reasons, knowledge of the interaction position is crucial, as the aim is to establish an output typical of a site in question. The degree to which the γ-ray interaction position is understood can impose a limiting factor on the extent to which the granularity can be improved. Secondly, the noise contribution must be minimised, as it is not characteristic of the interaction position but depends on the experimental surroundings, the

detector performance and setup. Finally, pulses generated by multiple interactions within the detector must be excluded, as they too are non-characteristic of the single interaction position which shall be defined.

For semiconductor detectors, two approaches exist to obtain pulse shapes characteristic of the interaction positions in a detector. The first involves solving Poisson's equation and calculating the charge induced on the contacts for an interaction site [Med04]. These *electric field simulations* have speed advantages and do not require a detector or any electronics, merely knowledge of its geometry. However, they must be validated with experimental data to ensure confidence in the simulated pulses. Further difficulties are the inclusion of any additional effects, such as the intrinsic delay of the preamplifier and/or cross-talk between channels, which must be added retrospectively. Phenomena such as cross-talk can prove particularly challenging to model and are often tedious to incorporate [Rad09].

An alternative is to produce the pulses experimentally, while controlling the interaction position of the γ-ray and ensuring the interactions all stem from only one energy deposit. The influence of random noise is minimised through summation of many pulses. This method is also necessary to validate any pulse shapes produced by electric field simulations.

Once derived, these pulses are stored in a look-up table or *pulse shape database* and compared with data from unknown interaction locations to enhance position resolution. The quality of agreement between a pulse shape response and the database can also indicate the presence of multiple interactions within a detector voxel.

The aims of this chapter are therefore to understand the charge response within the detector as a function of position, to apply this approach to real data to improve position resolution and to identify and deconvolve multiple interactions in a segment using this technique.

6.2 Experimental Setup

Two dimensions of the γ-ray interaction site were controlled by collimating the γ-ray source and mounting it to a table, whose position was manipulated with high precision stepper motors [Par08]. This restricted the incident γ rays to a spot of between 1 mm and 2 mm diameter, depending on the distance from the collimator opening. A secondary collimation stage, along with an array of bismuth germanate (BGO) scintillator detectors, was assembled around the germanium detector (see Figure 6.1). This allowed γ rays coincident between the two materials to be localised in three dimensions through the position of both collimator sets. This configuration also increased the number of single site interactions, as the unique kinematics of 90 ° Compton scattered γ rays are rarely reproduced by a sum of multiple interactions. Details on each individual setup component are discussed below, while the results of Monte-Carlo simulations evaluating this method are presented in Section 6.6. A schematic diagram of the experimental setup is presented in Figure 6.1, while a photograph of the experimental assembly is provided in Figure 6.2. As the figures illustrate, the SmartPET1 detector was mounted on its side as the dimension of primary interest was the 2 cm detector depth.

6.2.1 Scanning Table and Primary Collimation

A 907 MBq ^{137}Cs source was mounted inside a lead castle upon a mount coupled to two high precision Parker stepper motors [Par08]. The motors allowed the enclosed source to cross the detector face in x-y steps with micrometre precision, while the detector itself remained stationary. The source directionality was controlled with a 16 cm long coaxial tungsten collimator with a 1 mm opening diameter. This produced a well-defined beam of 662 keV γ rays.

6.2.2 Secondary Collimation and Scintillator Elements

To geometrically constrain the coincident γ-rays' scattering angle, an array of both secondary collimators and BGO scintillator detectors was assembled around the planar HPGe

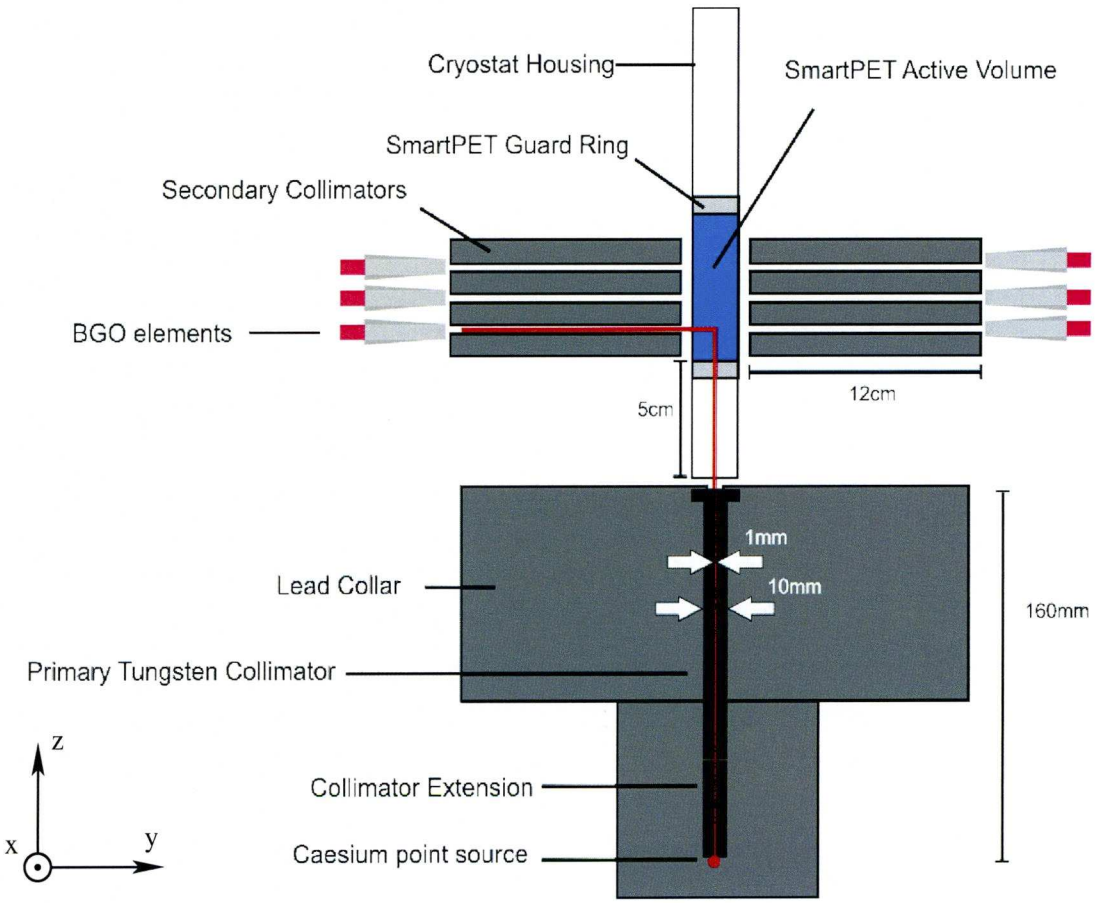

Figure 6.1: A schematic diagram of the experimental setup used to maximise single site interactions by selecting γ rays coincident between the germanium detector and the surrounding BGO array.

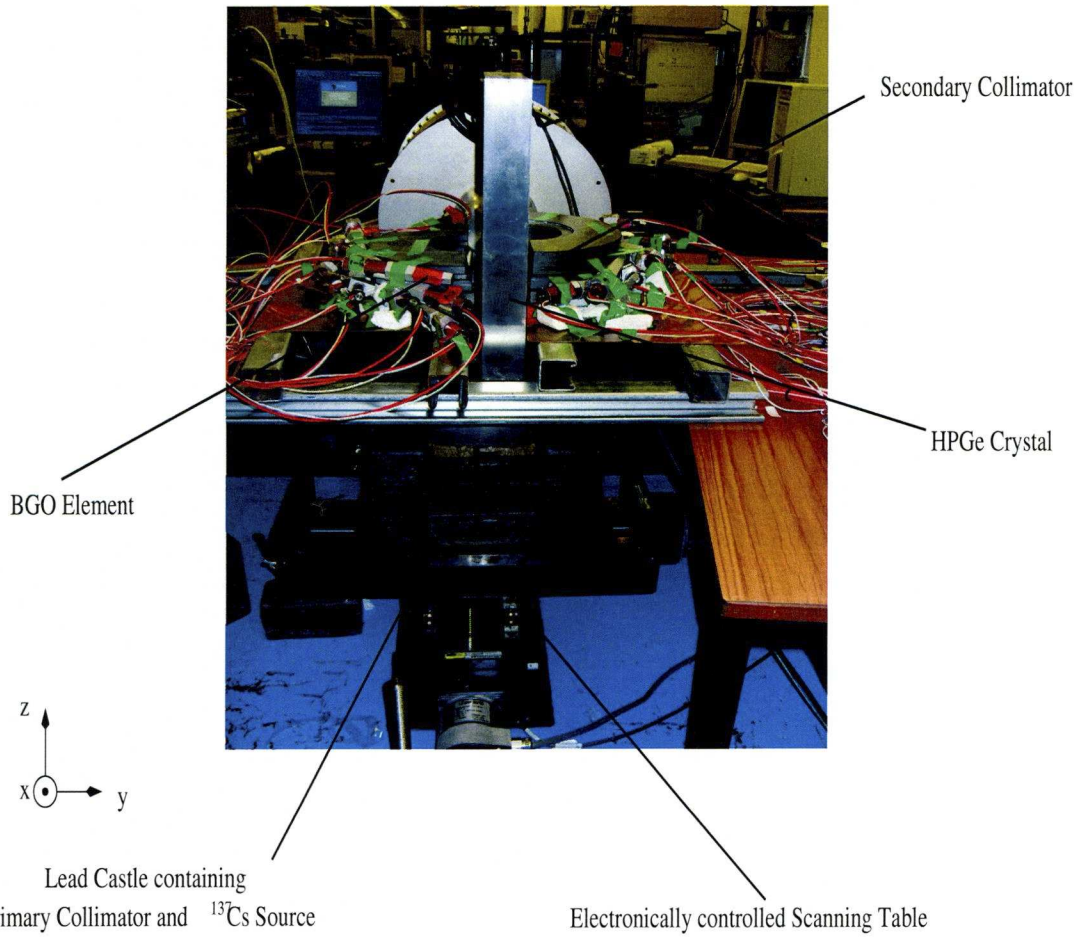

Figure 6.2: A photograph of the SmartPET detector mounted upon the scanning table surrounded by the secondary collimators and the BGO array.

detector. The secondary collimators were assembled from semi-circular lead slices with inner and outer radii of 5 cm and 13 cm respectively. The BGO elements were a mixture of hexagonally and pentagonally tapered cylinders of ~8 cm length with back and front radii of 2 cm and 1 cm respectively. Each crystal was directly coupled to a *photomultiplier tube* (*PMT*) supplied with an operating voltage of +700 V. Plastic spacing elements were placed between the stacked secondary collimator slices to define openings at three different positions in the crystal which shall be referred to as depths. The opening at the lowest depth was 1.5 mm wide while the two remaining openings were 3 mm wide.

6.3 Electronic Setup

The electronic data acquisition and trigger setup shall be discussed in terms of separate components corresponding to either the HPGe (SmartPET1) detector or the BGO array.

6.3.1 SmartPET Electronics

The SmartPET1 detector was biased to its operational voltage of -1800 V with an ORTEC 659 Detector Bias Supply. The 12 DC preamplifier outputs were fed, via a grounding panel, into the VME GRT4 cards (Section 4.2.1, [Laz03]) for digitisation. The signals from the 12 AC channels were branched into two paths at the grounding plate: one route leading to the remaining VME GRT4 channels; the other providing an analogue logic pulse to trigger data acquisition. The trigger signals were processed with three ORTEC 863 Quad Timing Filter Amplifier (TFA) units whose fast outputs were connected to three ORTEC 935 Quad Constant Fraction Discriminator (CFD) units. The internal delay of each CFD was set to 20 ns while the thresholds were individually set to ≈ 300 keV using a ^{152}Eu source and an ORTEC MAESTRO analogue to digital converter (ADC). The logical OR of all 12 CFD outputs was obtained using a Philips Scientific 755 Quad Majority Logic Unit. The extension of this logic pulse to 50 ns through an ORTEC 416A Gate/Delay generator acted as the indication of an energy deposit in at least one of the AC strips and the trigger for the SmartPET system.

6.3.2 Scintillator Electronics

The PMT outputs were fed into multi-channel gain/offset processing units, where the signal amplitudes and baselines were manually aligned. Subsequently, each signal was divided into two. As with the SmartPET detector, one half of the signals was led directly into the data stream through a CAEN N568LC 16 channel Programmable Spectroscopy Amplifier. This multi-channel output was integrated into the digital VME data stream using a CAEN 32 Channel Multievent Peak Sensing ADC. The remaining half of the output signals produced a trigger for the scintillator side of the coincidence setup. These pulses were amplified using three ORTEC 863 Quad TFA units following into three ORTEC 935 Quad CFDs. The thresholds on the scintillators were set to $\approx$60 keV with an ^{241}Am source. The logical OR of all CFD signals was generated using a LeCroy 380A Multiplicity Logic Unit, which transmitted a logic pulse, if any one of the 12 channels registered an impulse. This signal was prolonged with an ORTEC 416A Gate/Delay generator and then served as the BGO component to the coincidence signal.

6.3.3 Coincident Master Trigger

The trigger signal from each detector system was used to produce a coincidence gate by implementing a LeCroy 465 Triple 4-fold Coincidence Unit. Providing both triggers were registered within a 200 ns window, a master trigger signal was sent to a Philips Scientific 794 Quad Gate/Delay Generator, where it was converted to a TTL pulse. The TTL pulse was copied between each GRT4 card of the VME DAQ system using a LeCroy 429A Quad Mixed Logic Fan-In/Fan-Out. This signal prompted the digital acquisition of all pulses (SP1) and energies (BGO array) by the system. During data readout further triggers from the Gate/Delay generator were prevented, by directing the inhibit pulse from the GRT4 units back into the Gate/Delay generator with an additional LeCroy 429A module. Figure 6.3 is a simplified diagram of this electronics chain. To aid the clarity of the figure, the true number of signals is not displayed nor are units which fan these in or out.

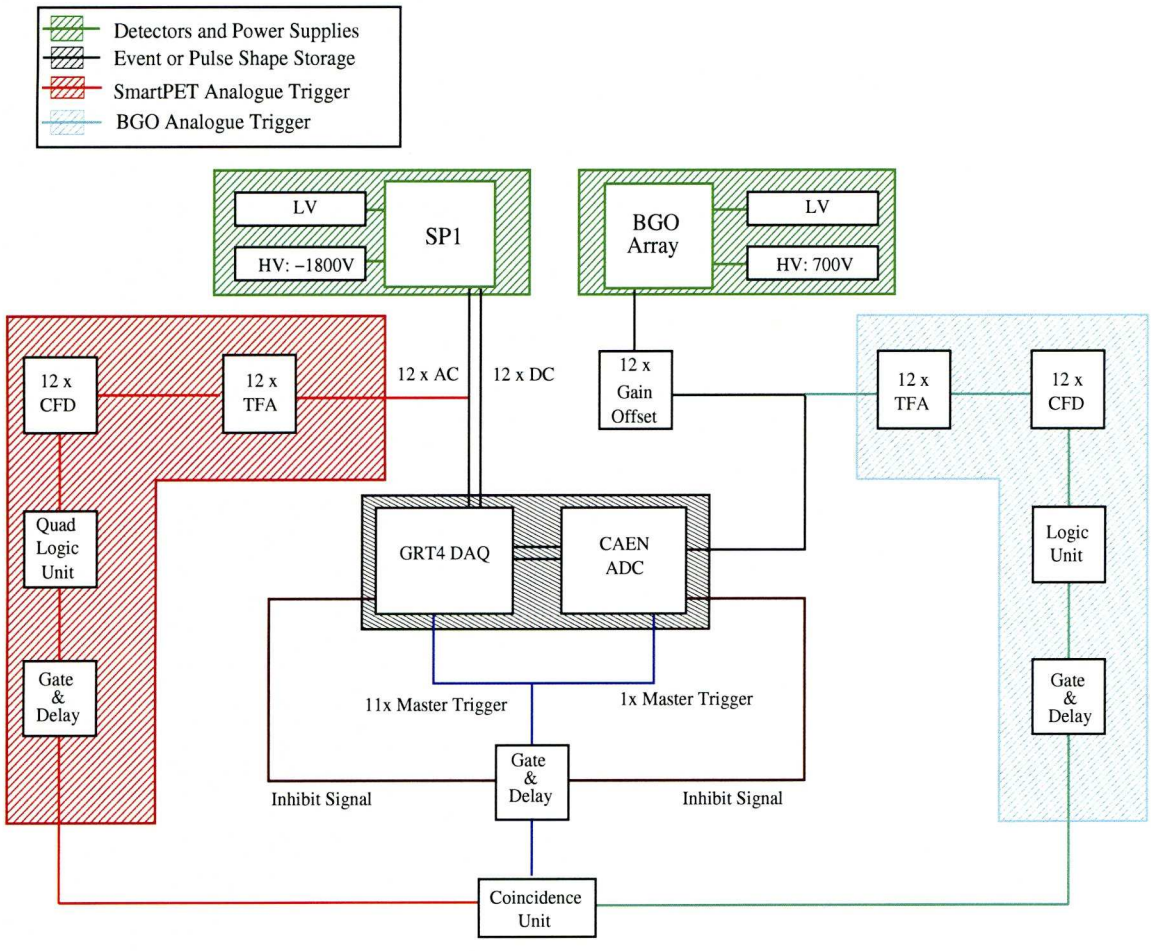

Figure 6.3: A simplified schematic diagram of the electronics setup for the coincidence trigger. Data are only digitised and stored when an energy deposit is registered in both the germanium and scintillator detectors.

6.4 Data Runs

The collimated beam was moved across the face of the detector in straight lines of 1 mm step size referred to as *runs* or *scans*. Figure 6.4 illustrates the paths of the collimated beam. In the figure, the detector is viewed looking upwards, from the perspective of the source. For each run, data were extracted at the three different secondary collimator depths: DC03, DC06 and DC09. The following scans were performed:

- centrally through AC05 from DC contact to AC contact
- centrally through AC03 from DC contact to AC contact
- centrally through AC10 from DC contact to AC contact
- parallel to the DC strip boundaries, 2.5 mm from the DC contact in AC03
- parallel to the DC strip boundaries, 2.5 mm from the DC contact in AC05
- parallel to the DC strip boundaries, 2.5 mm from the DC contact in AC10
- parallel to the DC strip boundaries, 2.5 mm from the AC contact in AC03
- parallel to the DC strip boundaries, 2.5 mm from the AC contact in AC05
- parallel to the DC strip boundaries, 2.5 mm from the AC contact in AC10
- parallel to the DC strip boundaries, in the centre of AC03
- parallel to the DC strip boundaries, in the centre of AC05
- parallel to the DC strip boundaries, in the centre of AC10

The source was placed at each position for 12 h at a coincidence rate of ~10 counts per minute (cpmin) to acquire sufficient statistics. The SmartPET singles count rate was ~80 counts per second (cps).

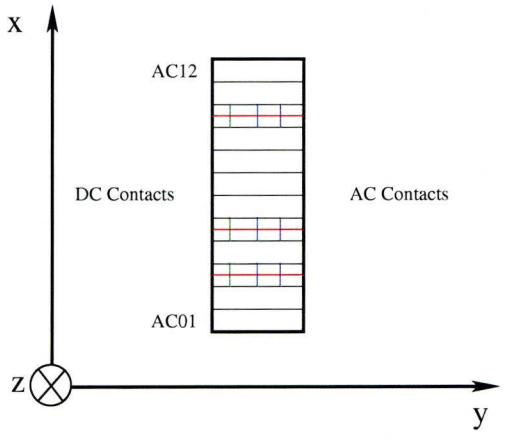

Figure 6.4: A schematic representation of the paths scanned by the collimated beam in steps of 1 mm size. For all lines, pulses were extracted for the three different depths of secondary collimation.

6.5 Data Pre-Selection Criteria

The coincident setup design aims to ensure a high fraction of the data consists of single site interactions. To verify that criterion, and reject events which scatter through either the primary or secondary lead shielding, the following conditions are applied before the data are accepted for analysis. Firstly, the events were requested to have only triggered one pixel in the detector i.e. one DC strip and one AC strip. Secondly, it is demanded that the scattered γ-ray interacting in the secondary detectors only triggers one row of scintillator elements.

6.5.1 Germanium Energy Spectrum vs. BGO Energy Spectrum

A γ ray entering the SmartPET1 detector with 662 keV which scatters by 90 °, and is fully absorbed in a scintillator element, will produce energy deposits of 374 keV and 288 keV in the germanium and bismuth germanate detectors respectively (see Compton Scattering in Section 3.1.2). Figure 6.5 is a two-dimensional histogram displaying the intensity of the energy registered in the scintillator material vs. the energy deposited in the germanium detector. The region of intense counts contains the genuine 90° scattered events. A

polygonal energy window or gate was placed around this region to extract pulse shapes assumed to only originate from true 90° scatter coincidences. The germanium detector energy gate was 40 keV wide and ranged from 350 keV to 390 keV, while the BGO gate included the energies from 240 keV to 349 keV.
The following experimental features can be observed in Figure 6.5:

- The threshold of the constant fraction discriminator for the HPGe trigger is visible as the level of background counts increases around the 250 keV mark on the x-axis. The scintillator threshold is also seen at around the $y = 60$ keV line.
- Secondly, photopeak energy deposits in the germanium are visible in a vertical line at $x = 662$ keV. These events arise when a γ ray is fully absorbed in the germanium in temporal coincidence with a deposit from background or scattered radiation in the scintillator. The line diminishes in intensity with increasing y as the likelihood of the scintillator stopping higher energy γ rays decreases.
- A vertical line at E_γ (x-axis) $= 511$ keV is also observed. This originates as some naturally abundant isotopes emit γ rays above 1022 keV, e.g. ^{40}K where $E_\gamma = 1460$ keV. These quanta contain sufficient energy to undergo pair production (Section 3.1.3), subsequently resulting in 511 keV γ rays detected in the germanium crystal. Providing they coincide with a background interaction in the scintillator, they shall be recorded and feature in the presented matrix.

6.6 Monte Carlo Setup Evaluation

The setup, described above, was modelled using the Geant4 environment [Ago03] to assess the accuracy of the fold- and energy-based single site event selection. The number of multiple site events, which fulfil all criteria stated above, was also to be obtained. A simplification was made, neglecting the individual BGO crystals and readouts. Instead,

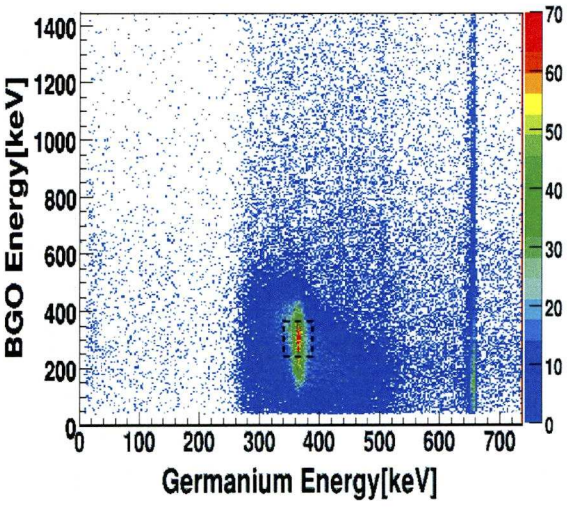

Figure 6.5: A two-dimensional histogram of scintillator energy shown on the y-axis vs. the energy measured in the germanium crystal plotted on the x-axis. The intense region of the plot surrounding (374 keV,288 keV), highlighted by the dashed box, contains the true coincidences between germanium and scintillator detectors. These γ rays have entered the germanium crystal with 662 keV, scattered by 90° and deposited their remaining energy in the scintillators. A detailed discussion is provided in the text.

cylindrical tubes of BGO detectors wrapping around the secondary collimators were modelled.

6.6.1 Scattering in the Shielding

The 90° scatter energy prediction presumes a γ ray incident on the crystal with an energy of $E_\gamma = 662\,\text{keV}$. Any Compton scattering, either in the lead shielding, along the tungsten collimator or in the housing of the detector, is neglected. To add confidence to this postulate, Figure 6.6 (black) displays the energy of the simulated γ ray, before its interaction with the germanium crystal. Here, the simulation allows the fraction of γ rays which deposit energy before reaching the crystal to be quantified. One clearly sees that the discussed assumption is largely valid as 75 % of γ rays which trigger the system enter

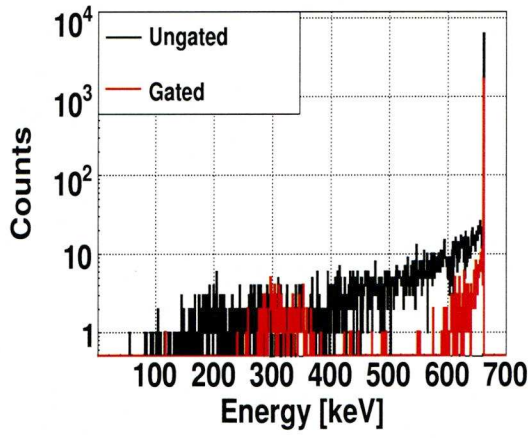

Figure 6.6: A simulated spectrum of the energy of the collimated γ rays before interacting in the germanium crystal (black). The y-values are depicted on a log scale. The figure highlights how most of the γ rays enter the detector with the expected 662 keV. (red) plots the simulated incident energy of the γ rays which met the energy gates applied to both the HPGe and the BGO.

the crystal with an energy of 662 keV. This value is dependent on the collimator material and geometry, rather than any γ-ray properties, yet is an interesting constraint on the data accuracy. The low energy tail on the photopeak in Figure 6.6 is indicative of small angle Compton scatters, either in the lead shielding or the tungsten collimator, while the continuum more distant from the photopeak is a result of larger energy losses most likely γ rays penetrating the lead shielding. In Figure 6.6 (red) the same information is displayed, however after only examining γ rays which deposit between 350 keV - 390 keV in the HPGe and 240 keV - 349 keV in the BGO. The figure illustrates how applying this gate accurately removes significant fractions of γ rays, which scattered previously, from the data.

6.6.2 Uncertainties in the Scatter Peak

There are three physical factors which contribute to the width of the experimental scatter peak in the germanium detector. As with the PET study in Chapter 5, an experimental approach only observes the summation of all uncertainties. In simulation, the ability to control sources of error and quantify their isolated influence is granted. In Figure 6.7 a simulated spectrum of deposited energy in the HPGe, providing a coincidence with the scintillator detector, is depicted in black. This spectrum does not include the intrinsic energy resolution of the HPGe detector, therefore the width of the peak is defined solely by the inaccuracy in the geometric definition of the scattering angle introduced by both the primary and secondary collimator openings. The red spectrum is broadened, by adding a random number to account for energy resolution in the detector. The random number was distributed around the true value following a Gaussian function. The σ parameter of the Gaussian was selected to produce a FWHM of 2.8 keV - a worst case example of the energy resolution measured with this detector. Finally, the blue spectrum was obtained in the experimental measurement from strip AC03 of the SmartPET detector and includes *Doppler Broadening* - a result of the γ ray scattering off a target in motion, namely a loosely bound electron of a germanium atom. As Figure 6.7 demonstrates, this effect dominates the width of the experimentally measured peak. The two simulated spectra are normalised to the experimental 374-keV peak. The FWHM of the individual peaks are summarised in Table 6.1. The effects of background radiation are also clearly visible in the experimental energy spectrum (blue), as is a 662-keV photopeak resulting from random coincidences as discussed in Section 6.5.1.

6.6.3 Fraction of Single-Site Interactions

The most interesting question to be answered with the simulation is the accuracy with which the selection process identifies single-site interactions. A histogram of the *multiplicity*, i.e. the true number of interactions, is presented in Figure 6.8 for the various filtering stages. As restrictions upon interaction fold and energy are applied, the fraction of single site interactions (multiplicity = 1) in the accepted data increases. Figure 6.8 confirms that

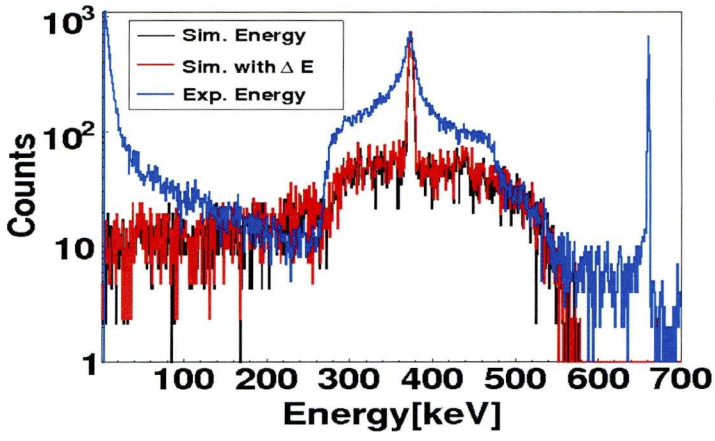

Figure 6.7: A comparison of both simulated and experimental energies deposited in the SmartPET1 detector. The black spectrum contains simulated energies with no additional blurring. The width of the peak is defined by the geometric opening angles of the primary and secondary collimators. The red peak includes the intrinsic energy resolution of the HPGe detector. The spectrum obtained experimentally is presented in blue. Its much greater width is due to Doppler broadening, an uncertainty produced by the γ ray scattering off a target in motion.

Source of Uncertainty	**FWHM [keV]**
Geometrical	6.5(2)
Geometrical and Energy Resolution	7.4(2)
Experimental	16.0(5)

Table 6.1: An overview of the individual FWHM of the simulated and experimental spectra. The uncertainties originating from the geometry, the detector performance and Doppler broadening have been quantified.

the most important condition in isolating single site interactions is to gate on the scatter peak in the germanium detector. The figure was produced applying a 40 keV energy gate (350 keV - 390 keV) in the HPGe and a 100 keV wide energy window on the scintillator

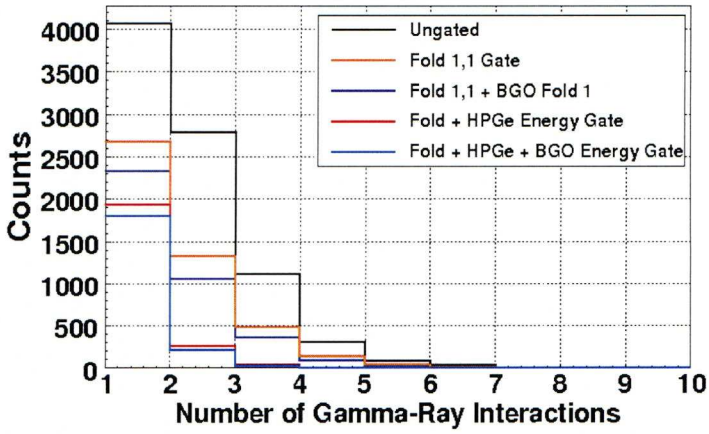

Figure 6.8: A display of the true number of interactions in an event which passes the quoted criteria as evaluated in the simulation. As the restrictions upon fold and deposited energy become stricter, the fraction of true single site events also rises. Finally, when all conditions are applied 89 % of the data are single site interactions.

energy (240 keV - 349 keV)[1]. The data which meet these conditions consist to 89 % of single site interactions.

6.6.4 Multiple Site Interaction Separation

For the 11 % of the data where a multiple site interaction passes the selection criteria, the distance between the two (or more) interaction points is crucial to the impact of this pulse on the database. Figure 6.9 contains the absolute distance between the first and second interaction in SmartPET1, providing the event fulfilled the acceptance criteria. The average distance between the two interactions is ≈1 cm. The interactions have been included in this histogram regardless of their deposited energy. As one interaction may deposit insufficient energy to trigger the experimental energy threshold, the absolute separation can exceed the boundaries of a voxel despite the fold <1,1> condition being realised. Although somewhat paradoxical, this phenomenon may well occur in the experimental data and must be included in the model.

[1]These gates are identical to those applied in the experimental analysis

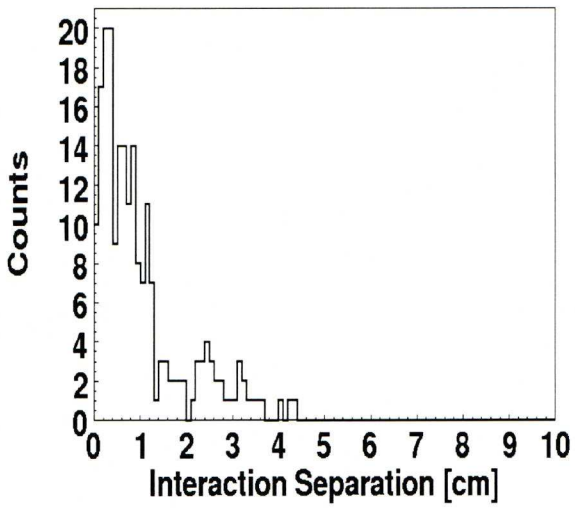

Figure 6.9: A histogram of the separation between multiple interactions which pass the applied restrictions as obtained from the simulation. The separation can exceed a strip boundary if one interaction deposited energy below the level of the experimental threshold.

6.7 Database Construction

The data pre-selection was carried out in the MTSort analysis package [MTS] and began with a three point energy gainmatching process. The data, selected based upon fold and energy restrictions, were extracted through a $3100 \times N$ matrix, where N defines the number of events which meet the criteria and 3100 arises as the approximate product between the 24 channels at 128 samples each. These pulse matrices were analysed in the ROOT environment [ROO], where a pulse analysis function library was developed.

The first analysis stage was to interpolate the waveforms by a factor of five from 128 samples to 640 samples, using a quadratic moving fit function. The original 128 pulses acted as the *skeleton* of the interpolated pulse and were not altered. A three parameter fit was performed over three samples of the skeleton (37.5 ns). The interpolated points between the first two samples were then filled according to the fitted quadratic expression. Subsequently, the fit range was moved forward by one skeleton point (12.5 ns) and the process repeated, until the end of the interpolated pulse was reached.

Next a filtering/smoothing algorithm acted upon the interpolated pulses, to reduce the

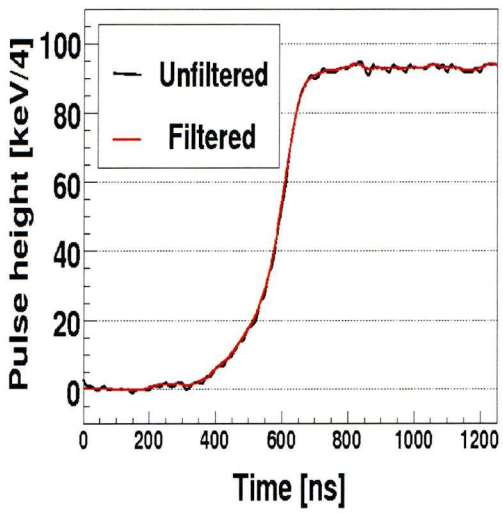

Figure 6.10: An example of a pulse pre- (black) and post-filtering (red). It is demonstrated that the filtering algorithm maintains the characteristic shape of the waveform yet removes a majority of the noise oscillations.

impact of noise fluctuations. A typical pulse pre- and post-filtering is presented in Figure 6.10. The figure illustrates how the filtered pulse (red) is smoother and less affected by noise spikes, yet the algorithm reliably conserves the shape of the original pulse (black). The filtering algorithm implements

$$F(j+7) = \frac{\sum_{i=0}^{15} P(j+i)}{15}, \tag{6.1}$$

where j=7,8,...589,590; P describes the unfiltered pulse and F corresponds to the filtered pulse. Equation (6.1) averages seven samples back in time and eight samples forward, replacing the central value with the average of the fifteen samples.

The real charge pulses were subsequently normalised to range from zero to unity by subtracting an average of the first 100 samples (baseline) and dividing by an average of the last 100 samples (maximum). The image charges were scaled by the same factor as their neighbouring real charge.

A correction to remove the preamplifier's exponential decay from the normalised maximum

height was applied, by summing the pulse with an exponentially fitted function from t100 onwards. The pulses were then *time aligned* (see Section 6.8). Time alignment, in this context, is the temporal shift of a pulse to maximise its overlap with another. A discussion of a selection of methods to time align traces, which are not globally synchronised, is provided in Section 6.8. Once time aligned, the pulses are summed and re-normalised to produce an average pulse response or *superpulse*.

Figure 6.11 illustrates the standard deviation (σ_{Noise}) on the baseline noise calculated over 100 samples for the superpulse, as a function of the number of pulses with which it was constructed. The figure highlights how, through summation of many pulses, the error resulting from electronic noise is reduced. No systematic error is observed to remain as the standard deviation tends to zero. The figure also confirms that, despite the low number of pulses available, a plateau in the standard deviation has been reached. The figure was produced using the pulses closest to the DC side at the lowest secondary collimator level

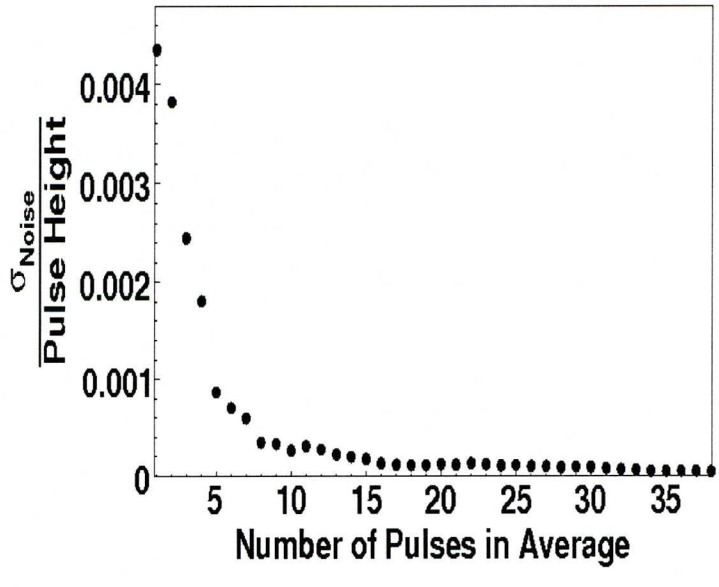

Figure 6.11: The standard deviation on the baseline noise of a superpulse as a function of the number of pulses used to construct the superpulse. The figure shows how despite less than 50 pulses the standard deviation saturates and tends to zero. No systematic error is observed in the trend.

in the voxel shared by AC05 and DC03.

Finally, the superpulse is compared to each individual pulse once more and a new superpulse is generated using only pulses which pass a χ^2-rejection test according to

$$\chi^2 = \sum_{AC-1}^{AC+1} \sum_{t=t0}^{t100} \frac{|P(t) - D(t)|}{\sigma} + \sum_{DC-1}^{DC+1} \sum_{t=t0}^{t100} \frac{|P(t) - D(t)|}{\sigma}. \tag{6.2}$$

In Equation (6.2) AC and DC are the AC and DC strip numbers which register real charge; $P(t)$ and $D(t)$ are the contents of the raw pulse and database pulse at time t. In Figure 6.12, each sub-plot depicts the χ^2 values for all pulses at a position through the voxel shared between AC05 and DC03 (lowest secondary collimator level). Position 1 (top-left) was the position closest to the DC side. The first five positions are in the top row from left to right, while positions 5-10 are in the second row etc. The rejection thresholds were set individually for each position based upon the quality of its pulses and were gauged to include as close to the most accurate 66.6̇% of events as possible.

Figure 6.13 contains the averaged charge pulses for a line of positions where the collimator was moved in 1 mm steps from the DC to the AC face. The collimated beam line ran as centrally as possible through AC05; events in DC03 were selected by gating on the lower BGO level. The real charge pulses are aligned to $t5$ for the display purposes of the figure, yet the iterative alignment approach (Section 6.8.3) was employed in the analysis. Image charges are presented from AC04 and AC06, DC02 and DC04. These are included in the neighbouring sub-plots. A number of observations can be made from the figure. First the separation of the real charges is more dominant in the AC pulses than in the DC pulses. This has also been observed in earlier studies including [Tur06, Coo07b, Coo08, Gri09].

Secondly, the imbalance between the magnitudes of the image charges in the AC strips (AC04 vs. AC06) implies that the beam was positioned slightly off-centre in AC05. Judging by the image charges, its positioning was marginally closer to AC06. This observation is not made in the z-dimension, where the magnitudes between the image charges on DC02 and DC04 are in reasonable balance.

Figure 6.14 contains the pulses from the same collimator positions as discussed above,

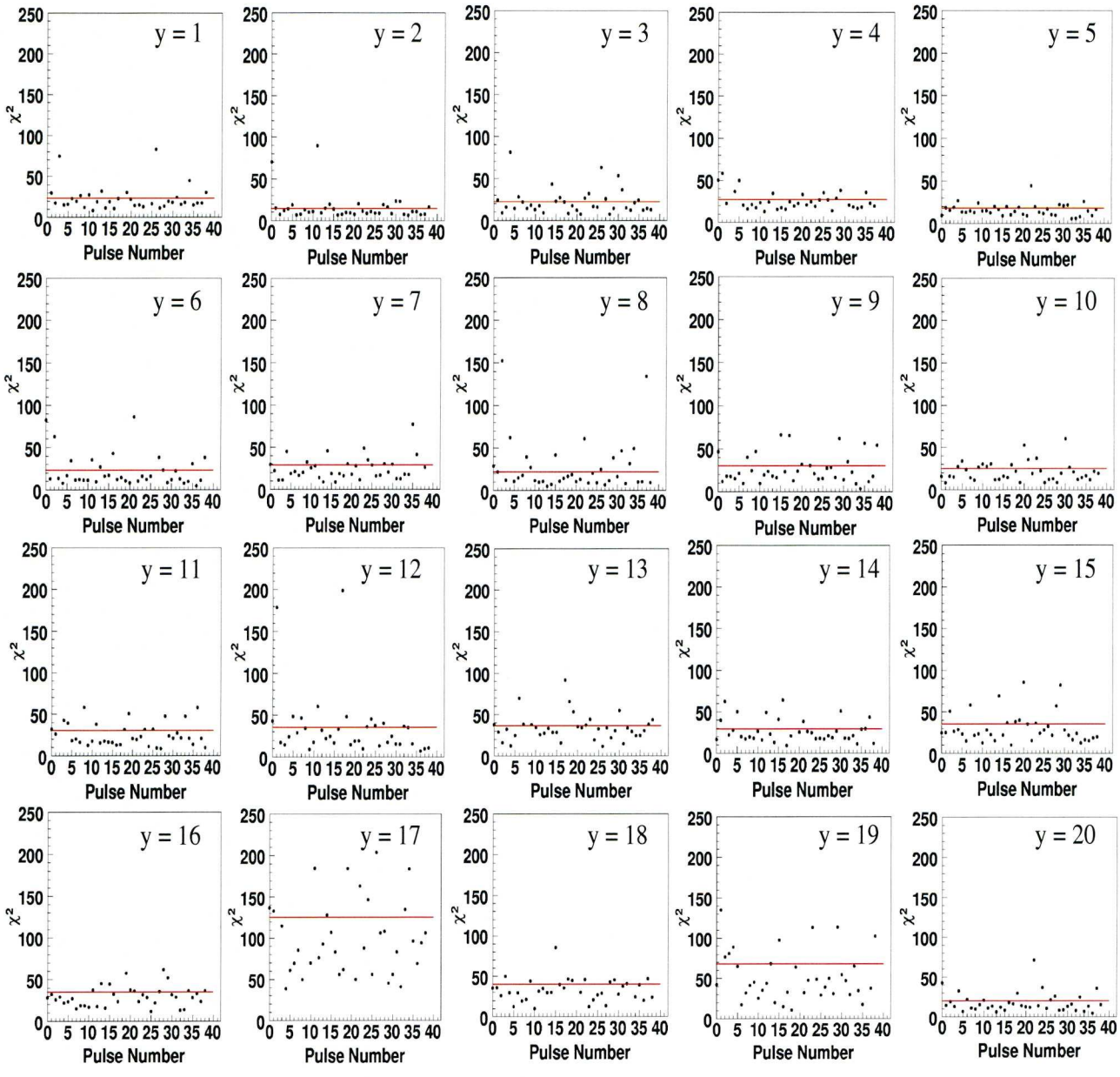

Figure 6.12: A histogram of the χ^2 values for all pulses and positions at the lowest secondary collimator level. The first row displays the results from positions 1-5; the second from positions 6-10 etc. The χ^2 rejection level is displayed by the horizontal red line on each sub-plot. The level was adjusted for each position to include the most characteristic 66.6% of the data.

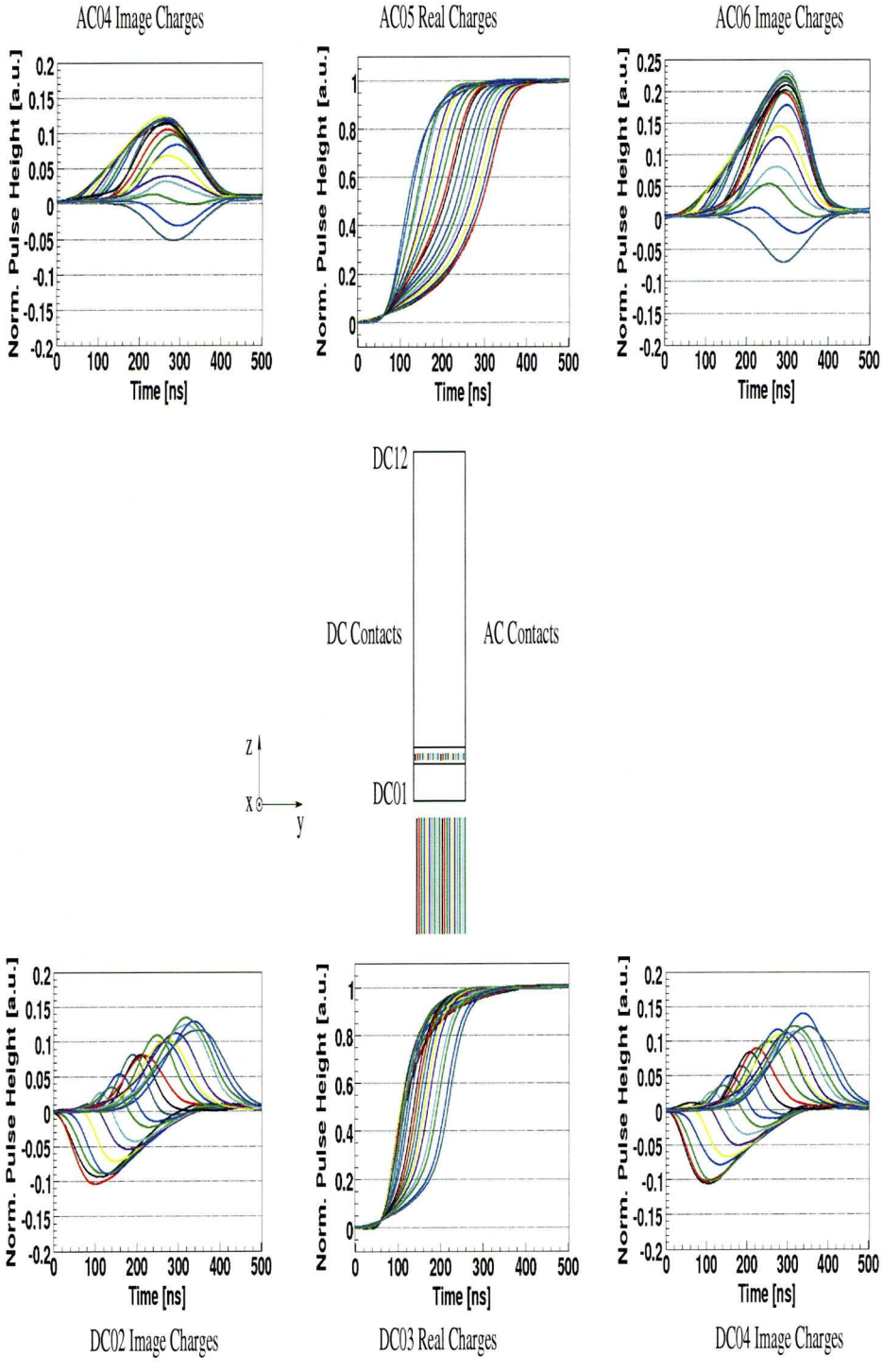

Figure 6.13: The position characteristic charge response for twenty interaction positions through the depth of the pixel shared between AC05 and DC03. The average response from strips AC04, AC05 (real charge) and AC06 are depicted at the top of the figure. The DC pulses from DC02, DC03 (real charge) and DC04 are presented in the bottom row of sub-plots.

however this time the voxel shared between AC05 and DC09 was selected by gating on the higher BGO level. Real charges from AC05 and DC09 are presented along with neighbouring image charges from strips AC04 and AC06 and DC08 and DC10. It shall be noted that only 18 pulse shapes, corresponding to 18 positions, are displayed in the figure. At the DC09 level - furthest away from the collimator - the two positions closest to the DC side did not acquire sufficient statistics to form an average pulse. This relation between available events and distance from the AC face was consistently observed at all secondary collimator levels and is a result of using the AC face as the acquisition trigger. Fortunately, sufficient statistics were available at lower secondary collimator positions. In Figure 6.14, the image charges in DC10 show increased amounts of cross-talk over the image charge pulses in DC08, DC02 and DC04. As no net charge is collect at the image charge contacts, the pulse should return to the zero baseline value. This does not occur in DC10, implying that minimal amounts of charge remain in the strip. This charge is the result of cross-talk between electronics cables and circuity in the signal path. A speculative reason the cross-talk is observed more dominantly in this channel is that its neighbouring contact DC11 has registered a mechanical fault, since the detector's commissioning in 2004. Increased cross-talk is, therefore, likely to take place between the contacts in question, if they are not sufficiently grounded inside the cryostat.

6.8 Time Alignment Optimisation

Along the stages discussed above, significant issues arose in optimising the time alignment of the pulses. The tested methods, their surrounding issues and procedures through which they were overcome, are discussed herein.

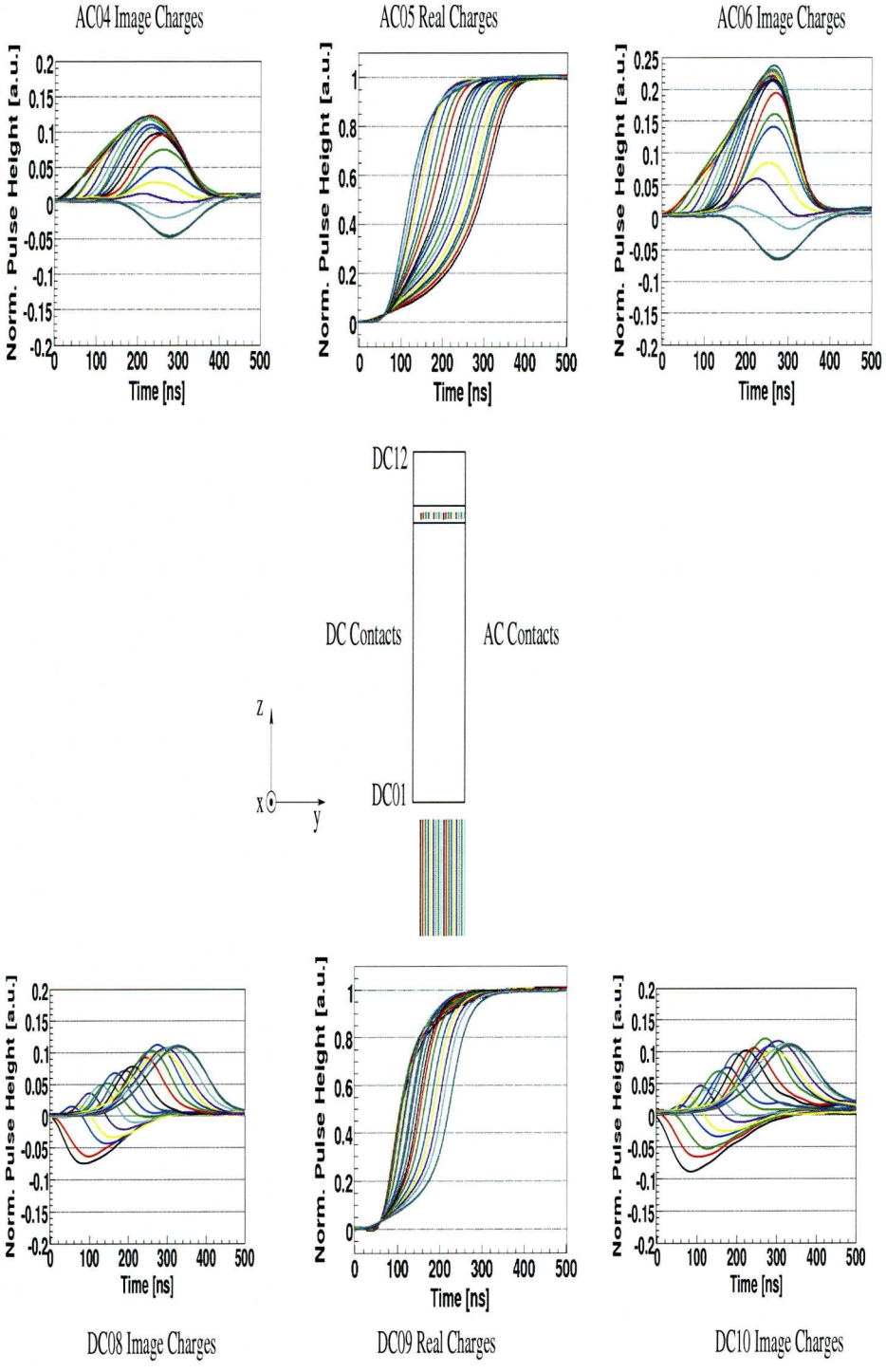

Figure 6.14: The position characteristic charge response for eighteen interaction positions through the depth of the pixel shared between AC05 and DC09. The average response from strips AC04, AC05 (real charge) and AC06 are depicted in the top of the figure. The DC pulses from DC08, DC09 (real charge) and DC10 are presented in the bottom row of sub-plots.

6.8.1 Parametric Time Alignment

Parametric time alignment has been employed to construct superpulses in [Coo08, Dim08, Gri09]. The method uses a fixed fraction of the pulse height e. g. t10[2] to serve as an alignment point . For two pulses, t10 is calculated and one pulse is dynamically shifted forward or back until their t10 values overlap. This process is referred to as *parametric time alignment to t10.* Weaknesses in this method arise when significant noise fluctuations are observed; an example of this is provided in Figure 6.15(a). The inaccuracy of the alignment is a dominant source of error when matching uncollimated data to the pulse shape database (Section 6.9.1). Alternative methods were thus devised as a part of this thesis.

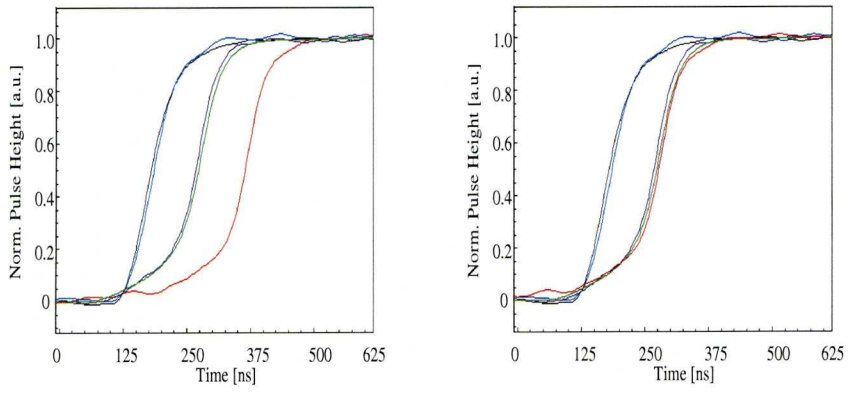

(a) Pulse aligned to t10

(b) Pulse correctly time aligned

Figure 6.15: An example of a pulse which is inaccurately time aligned using the parametric method. The black and pink pulses are average pulses while the blue and green pulses are responses from the same position which align well with this approach. The pulse displays a large fluctuational artifact in its earlier trace and is falsely aligned parametrically in Figure 6.15(a). In Figure 6.15(b) the red pulse has been correctly aligned using the iterative approach (Section 6.8.3).

[2]The reader is reminded that t10 is the time at which a real charge pulse reaches 10% of its height.

6.8.2 Constant Fraction Time Alignment

In an attempt to align pulses to a parameter less sensitive to fluctuations caused by noise and variations in shape, an algorithm based around a digital constant fraction discriminator (CFD) was implemented. A CFD is applied in experimental pulse processing when a timing signal is required from pulses, which are expected to differ in shape. The inaccuracy produced in a timing signal attributed to the shape of a trigger signal is referred to as *walk* [Kno99] and is significantly reduced by implementation of a CFD. A version of this approach would therefore seem applicable to this problem. A digital CFD is also often used in *free-running* digital electronics, e. g. the Lyrtech ADC (Section 4.2.2), to identify real charge without the need for an analogue trigger. The CFD algorithm was devised loosely around the description of a CFD pulse processing unit found in [Kno99]: in the algorithm, a duplicate of the pulse is inverted, amplified and delayed. An example of the original pulse, along with the duplicate, are provided in Figure 6.16(a). The unaltered original pulse is then summed with the manipulated copy to produce the waveform presented in Figure 6.16(b). As in the experimental pulse processing unit, the *zero-crossing point* of the summed pulse should be independent of pulse shape and only be susceptible to uncertainties induced by electronic noise (*jitter*) [Kno99].

6.8.3 Iterative Time Alignment

The final time alignment algorithm implemented is referred to as *iterative time alignment*. This approach consumes significantly more computer processing time than the two discussed above, yet has produced more accurate results. Here, pulses are first aligned to t10 using the parametric method. One pulse is then shift backward in time by 50 ns. A χ^2 parameter is then calculated (Equation 6.2), assessing the agreement between the two pulses at this point. The shifted pulse is then moved forward by 100 ns in 2.5 ns increments (one sample), thus sweeping over the second pulse. A χ^2 value is calculated and stored for each of the 40 positions. The position of minimum χ^2 is declared the point at which the pulses are correctly time aligned. Figure 6.17 depicts typical χ^2 entries as a function of pulse positioning as one waveform is dynamically swept over another. A

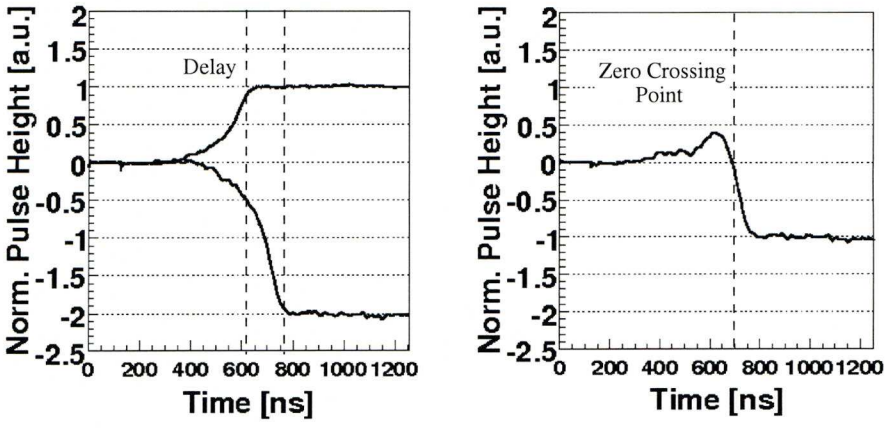

(a) Original and Inverted Pulse (b) Summed Pulse

Figure 6.16: Excerpts from different stages of digital CFD algorithm. Figure 6.16(a) shows the original pulse (top) along with the inverted, amplified and delayed copy. Figure 6.16(b) displays the sum of the two. The zero-crossing point to which the pulses are time aligned is indicated by the vertical dashed line.

single, distinct global minimum, representative of the point where the pulses are aligned, is clearly present. The remaining χ^2 at the global minimum is a result of the electronic noise on both pulses.

6.8.4 Time Alignment Assessment

The quality of each time alignment algorithm has been quantified by measuring the FWHM of a set of time aligned pulses. The assessment was conducted for two extremes of pulse shape: the most challenging shape i.e. with a shallow gradient around t10; and the least challenging shape i.e. with a steep gradient around t10. Table 6.2 and Figures 6.18 and 6.19 depict the precision of each algorithm for the different example cases. The most reliable was the iterative approach which produced a FWHM of 10.0 ns and 5.0 ns for the two selected scenarios.

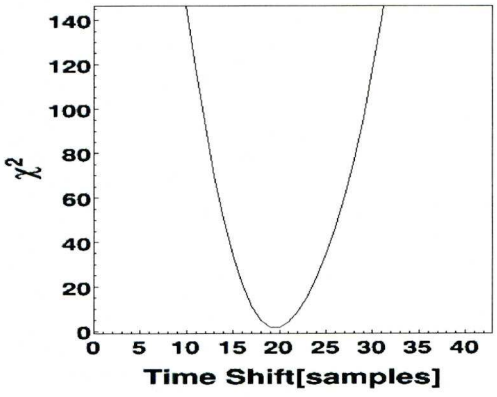

Figure 6.17: An example of the χ^2 agreement between two pulses as a function of pulse position as produced with the iterative time alignment algorithm. A well defined global minimum is reached when the pulse shapes are aligned.

	Method	FWHM [ns]
Shallow at t10	Parametric	53 (3)
	Constant Fraction	18 (3)
	Iterative	10 (3)
Steep at t10	Parametric	18 (3)
	Constant Fraction	8 (3)
	Iterative	5 (3)

Table 6.2: An overview of the time distribution measured in full width half maximum (FWHM) for the time alignment algorithms. Two extreme cases of steep and and shallow initial rise have been studied. The iterative time alignment method demonstrates best performance.

6.8.5 Time Alignment of Image Charges

Both nearest neighbour and next-to-nearest neighbour image charges prove significantly more challenging in their time alignment. A combination of their shape and poorer signal

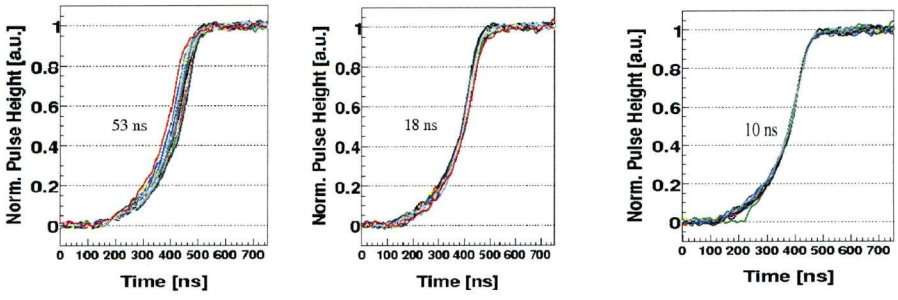

(a) Parametric T5 (b) CFD (c) Iterative

Figure 6.18: An overview of a sample set of pulses time aligned using the three algorithms discussed in this section. Pulse shapes with an initial slow rise were selected as the low shallow gradient ensures their early alignment is most challenging. The figure highlights how the most accurate match is reached with the iterative approach.

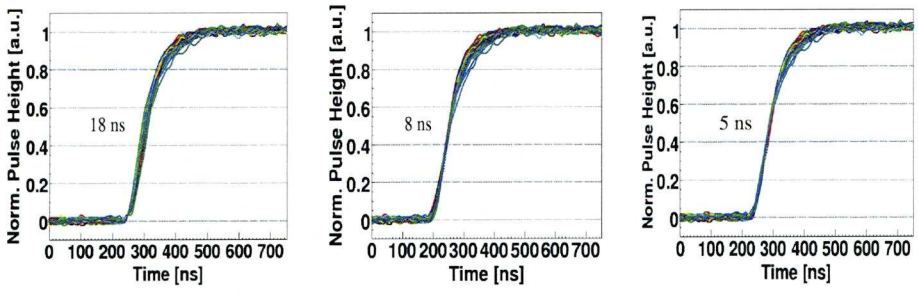

(a) Parametric T5 (b) CFD (c) Iterative

Figure 6.19: An overview of a sample set of pulses time aligned using the three algorithms discussed in this section. In this figure, pulse shapes with an initial fast rise are presented. These pulses are easier to align due to the steep early gradient. The figure highlights how the most accurate match is reached with the iterative approach and how performance is improved for pulses with an initially fast rise.

to noise ratio is responsible for this issue. Two methods of image charge time alignment were studied. In the first approach, the image charges are not time aligned but the traces are averaged without additional processing. The disadvantages to this method are obvious, as no correction has been applied for the sources of pulse misalignment. Specifically, these

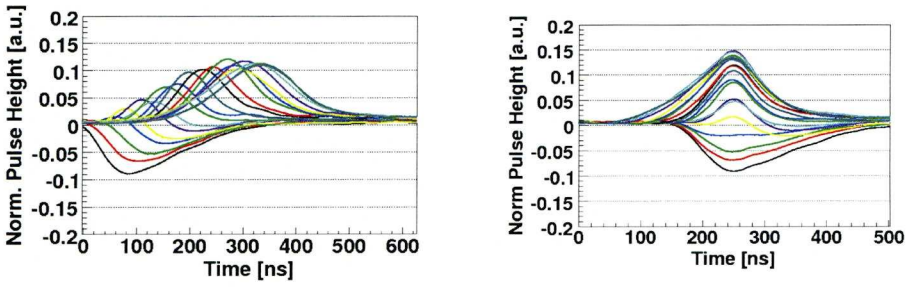

(a) No Time Alignment

(b) Point of Greatest Displacement

Figure 6.20: A comparison of image charge time alignment methods for pulses from DC02. The pulses in Figure 6.20(a) were not time aligned but summed without further processing. In Figure 6.20(b) the pulses were aligned to their point of maximum displacement.

are: the jitter induced by electronic noise when establishing a trigger point with the CFD which should be of random nature; a delayed output as the digital electronics are readout sequentially. The latter effect will follow a systematic trend. However, as pulses which originate from the same electronics cards are to be compared, the systematic delay will be constant and negligible. It shall be argued that the jitter, present in the CFD signal, which culminates in a timing error on the trigger signal, will oscillate in a Gaussian manner around the true trigger time (t0) thus a net offset should be minimised through the averaging process. Figure 6.20(a) depicts an example set of image charges through the depth of the crystal using this simplistic approach. The second method aligned the image charges parametrically to their point of maximum displacement from the baseline. This method produced more reliable results for strongly unipolar image charges as their point of maximum offset was characteristic of their shape and accurately obtained and reproduced. The alignment was less accurate for image charges low in magnitude and of a bipolar nature. These were particularly susceptible to a bias introduced by the method. As seen in Figure 6.20(b) only very few bipolar image charges are observed; this behaviour strongly disagrees with predictions by basic weighting field calculations and existing work (see Section 6.12 and [Tur06]).

In summary it was deemed more important to be consistently less accurate, yet pro-

duce reliable, unbiased data. Therefore, the image charges were not time aligned to any further degree than their natural overlap. It should be stressed that no systematic error should be introduced as the image charges under comparison originate from the same electronics channel. When comparing pulse shapes (of any type) from different channels, a correction for the sequential readout must be applied.

6.9 Matching Collimated Data with the Database

Having produced the pulse shape database using optimised algorithms, the position resolution achievable with this approach must be made a subject of study. For this purpose, the collimated pulses and the database were compared to obtain the position of minimum χ^2 value. An event was defined as correctly matched if its position of lowest χ^2 agreed with the location of the collimator to a degree of Δy. The Δy parameter is the level of uncertainty tolerated in the matching process. For example, it is logical to accept events as correct if they are matched to within 1 mm of the collimator position due to the 1-2 mm spot size of the beam. This criterion would be described as $\Delta y = 1$ mm; the demand of an exact match is referred to as $\Delta y = 0$ mm.

6.9.1 Accuracy through the Depth of SmartPET

The accuracy of the database was assessed for the positions running along the y-axis through the centre of AC05 for two separate secondary collimator levels: the upper layer (DC09) and the lower layer (DC03). The single site interactions from the coincidence data acquisition were treated as interactions from unknown positions. These test pulses were extrapolated, filtered, normalised (see Section 6.7) and then compared with every pulse in the pulse shape database from the relevant voxel to produce the position of best fit with the χ^2 parameter in Equation (6.2). Iterative time alignment was utilised to overlay the pulses. The results for the upper (lower) layer are represented graphically in Figure 6.21(a) (Figure 6.21(b)). Significant fluctuation is observed for $\Delta y = 0$ through the detector which appears to follow no logical pattern. The erratic nature of the distributed

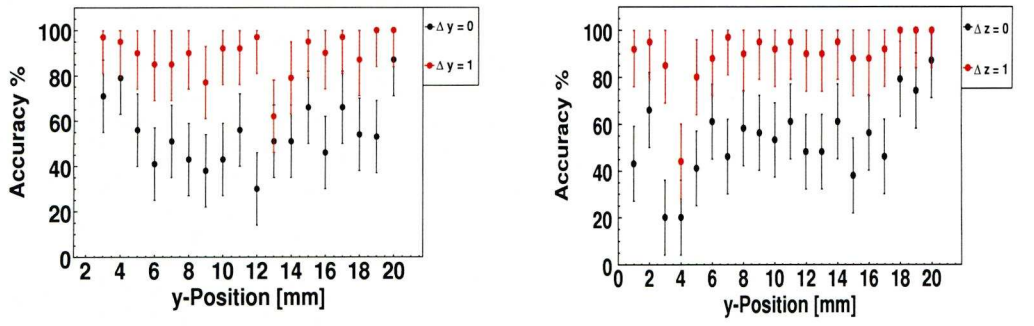

(a) Upper Layer (b) Lower Layer

Figure 6.21: The accuracy of the raw pulses when matched with the database across all available positions. The Gaussian properties of the beam spot are observed for most points. Approximately 55% of the data lie within 1 mm of the point, while over 90% lie within 2 mm.

points is indicative of the limitations in sensitivity being approached. Factors which contribute to these limitations are the overlap in shape of the pulses due to noise and the spot size of the beam incident upon the detector.

Overall ~55% of events are matched to the exact position ($\Delta y = 0$) in the upper layer and ~53% of events for the lower layer. For the Δy= 1 mm tolerance level the accuracy improves to 91% (upper layer) and 90% (lower layer). This implies that although the combination of beam spot size (1-2 mm), noise level on the pulses and detector sensitivity struggles to reliably identify pulses to the 1 mm level, an average 90% of pulses are matched within one millimetre of their correct position. No reduction in accuracy is observed due to the larger spot size in the upper depths. This indicates that the limit in accuracy for both $\Delta y = 0$ mm and $\Delta y = 1$ mm is dominated by resemblance of pulse shapes at neighbouring positions and their overlap due to noise. Because of this increased similarity between the pulses separated by 1 mm, an interpolation between the pulses to 0.5 mm spacing was not performed.

Figure 6.22 depicts 20 histograms of the difference between the position of the collimator and the position of best fit as retrieved by the database matching for the data

from the lower secondary collimator layer. The majority of histograms have a mode of zero, supporting earlier statements that any error is evenly distributed around the collimator position. The FWHM of the position spectra in Figure 6.22 varies between 1 mm ($y = 20$ mm) and 3 mm ($y = 15$ mm). With the exception of one histogram ($y = 4$ mm) all positions have the highest number of entries in the correct bin. These observations promote the applied method and reinforce the postulate that position resolution has been accurately improved compared to earlier studies [Coo07a, Gri09]. As a majority of events are matched to the correct millimetre and any discrepancies are consistent with uncertainties introduced by the spot size, it shall be claimed that a position resolution of 1 mm in the depth dimension has been obtained for single site events.

6.9.2 Accuracy across a SmartPET Strip

Using the processing stages described above, the pulse shape database was expanded to include pulses from lines running across strips perpendicular to the segment boundaries. As with the pulses running through the depth of the crystal, the coincident single site pulses were compared with the database to evaluate its performance. In this section a line of collimator positions which ran across AC05 in 1 mm steps shall be discussed. The primary aim of these scan points was to investigate the image charge behaviour, as a function of position across the strip. Due to experimental time constraints, only selected lines in the strip were scanned (as in Figure 6.4). These were positioned:

- 5 mm away from the DC contact ($y = 5$ mm)
- in the centre of the strip ($y = 10$ mm)
- 5 mm away from the AC contact ($y = 15$ mm).

As with the real charges, it was imperative to derive the most efficient and accurate means of matching pulses to the database. The methods investigated included a calculation of the parametric *image charge asymmetry* (*ICA*) with

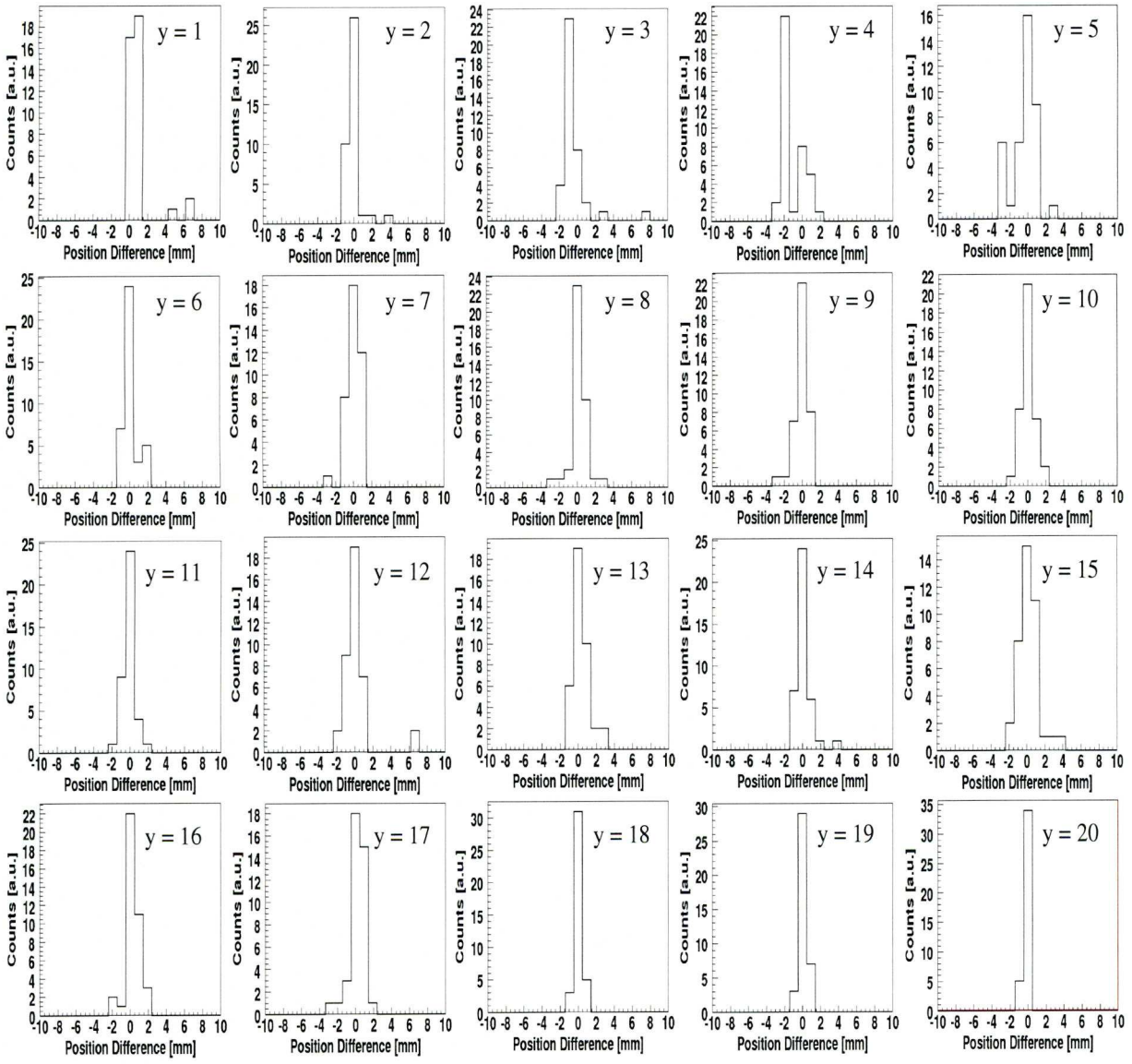

Figure 6.22: A histogram of the distance between an event's position of minimum χ^2 and the collimator position for each point through the depth of the detector.

$$ICA = \frac{A_{left} - A_{right}}{A_{left} + A_{right}}, \tag{6.3}$$

where A_{left} and A_{right} correspond to the absolute area underneath the left and right image charges respectively. Position matching with the image charge asymmetry has been applied in earlier studies e.g. [Mat06, Coo07a, Coo09] to obtain a single value representative of the lateral distance of the γ-ray interaction from the AC or DC strip boundaries. The position was determined by matching the ICA of a single event to the ICA values of the database. This figure of merit shall be compared with the more detailed method executed for real charges in Section 6.9.1, where a χ^2 value is calculated using the entire pulse. In this approach, the image charges are time aligned (TA) parametrically to their maxima and a χ^2 parameter is calculated. It was also investigated whether the image charge accuracy is increased by scaling the image charges (Scale), to ensure their maximum height matches that of the database pulse [3]. Table 6.3 summarises the accuracy values for both Δy=0 mm and Δy=1 mm for the data across the strip close to the AC face. Results for the three discussed methods are presented. The first observation is that the scaling function significantly reduces the accuracy of the matching process. This is most probably due to the scaling being applied to one value i.e. the maximum and therefore being very sensitive to noise.

Secondly, unlike the real charges, a clear position dependence is observed in the accuracy. A plausible explanation for this is the reduced magnitude of the image charges in the central regions of the strips and the subsequent decrease in signal to noise ratio. A further contributing factor is the bipolar nature of the image charges, resulting in time alignment inaccuracies. Having dismissed the image charge scaling, both the time alignment with χ^2 matching and the ICA produce very reliable results at Δx=1. The Δx=0 accuracy average is over 10% higher for the χ^2 data and on average 35% higher near the measured strip boundaries. It shall also be noted that the performance at Δx=1 is identical, within

[3] Although the charges are already of similar height, there is some uncertainty in the gainmatching process and in the exact interaction position due to the spot size. Therefore a pulse-by-pulse scaling was investigated.

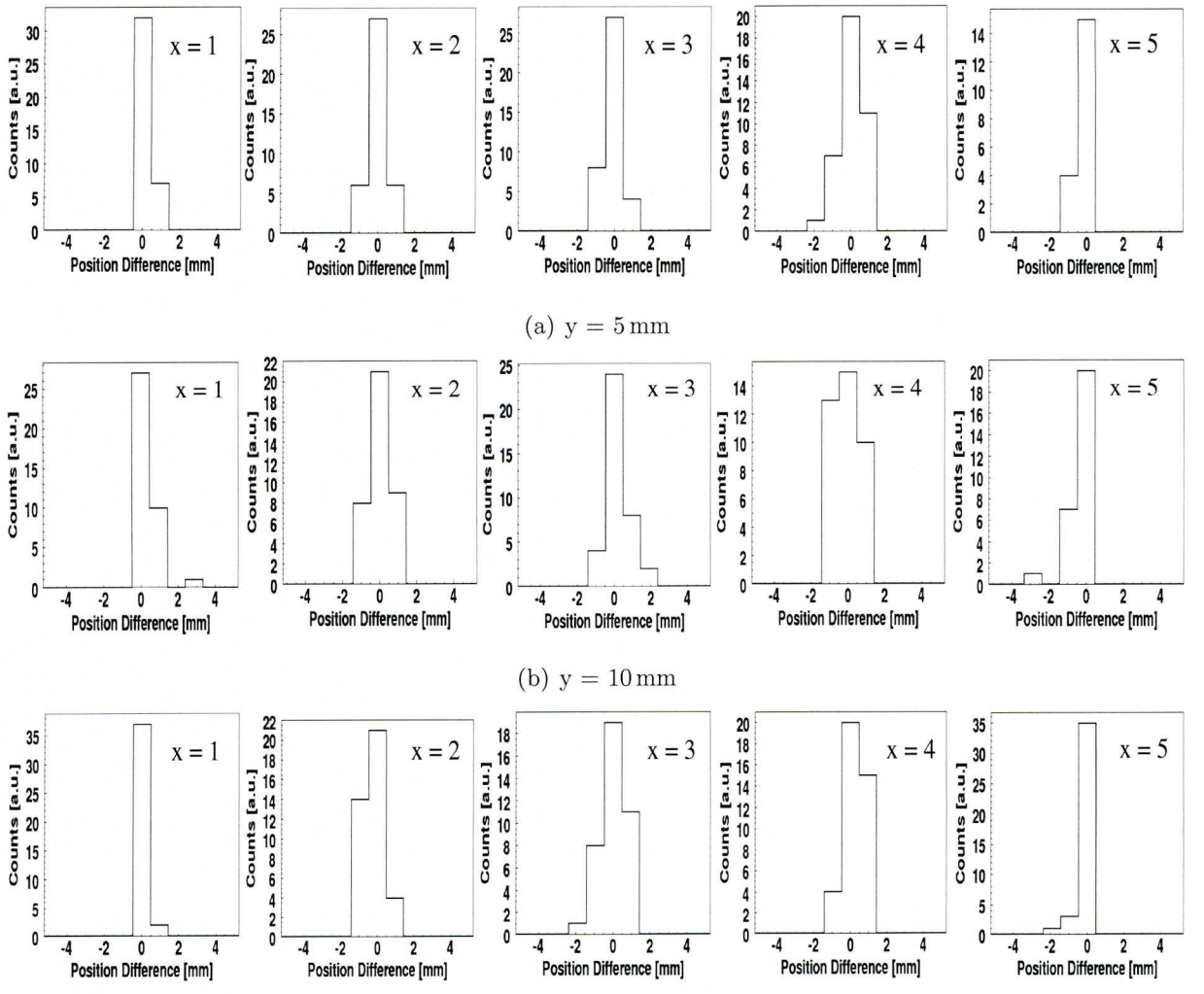

(a) y = 5 mm

(b) y = 10 mm

(c) y = 15 mm

Figure 6.23: Histograms of the distance between the γ-ray interaction position as determined by the pulse matching process and the true collimator position. Histograms are presented for all five positions scanning across a strip near (a) the DC side , (b) in the centre of the strip and (c) near the AC side

Position	Accuracy %					
	TA + Scale + χ^2		TA + χ^2		ICA	
	Δx=0	Δx=1	Δx=0	Δx=1	Δx=0	Δx=1
1	66	95	94	100	66	100
2	30	95	53	100	71	100
3	28	79	48	97	51	97
4	30	77	51	100	33	100
5	8	72	89	97	53	95
Average	32	83	67	99	55	98

Table 6.3: A depiction of the accuracy of the match of collimated data to the database for positions moving across the centre (y=10 mm) of AC05. Three different methods are presented. Reduced accuracy is observed in the centre of the strips, yet the Δx=1 accuracy is very high for both a parametric and the full pulse comparison based approach.

errors, between the simplified parametric ICA figure of merit and the more complex χ^2 value. This implies the simple parametric approach may suffice for resolution of ~2 mm, whereas 1 mm position resolution can only be achieved using the full χ^2 comparison to a pulse shape database. Depending on the specific application of the detector, one approach may be chosen over the other.

6.9.3 Evidence of Weak Electric Field at Strip Boundaries

The behaviour of the average real charge pulses when scanning across the 5 mm dimension of an AC strip was also investigated. The AC and DC real charges from the scan line 5 mm away from the DC face are presented in Figure 6.24(a). The DC pulses are presented for comparison and are all near identical in shape, with no consistent difference observed between them. This is to be expected, as the interaction position is consistently aligned centrally in the DC strip. On the AC side, charge collection properties toward the strip boundaries are pronounced. The charge is collected slightly faster in the centre of the

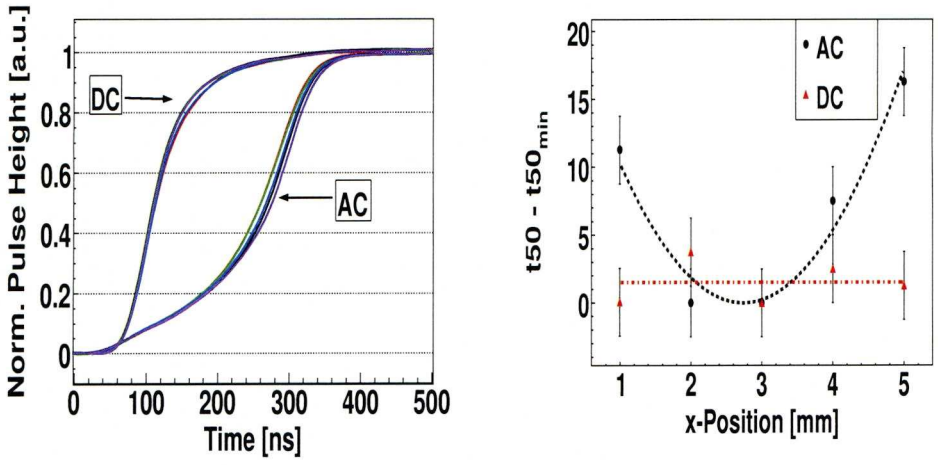

(a) (b)

Figure 6.24: (a) Average pulse shape sampling across the strip 5 mm away from the DC side. The AC pulses are marginally slower toward the boundaries of the strip. (b) The $t50$ - $t50_{min}$ values for both the AC and DC pulse shapes. The t50 values highlight the reduced charge collection time close to strip boundaries on the AC side.

strip, than it is toward the strip boundaries. To emphasise this trend, the difference between each $t50$ value and the fastest of all five $t50$ values ($t50_{\text{min}}$) have been plotted as a function of position across the strip in Figure 6.24(b) for both the AC (red triangles) and DC (black dots) pulses. Although the error bars of ± 2.5 ns (one sample) are relatively large in comparison, it is argued that these values follow a trend indicating slower charge collection toward strip boundaries on the AC side, particularly as this effect is also found for scans across the strip at the centre of the crystal (10 mm depth) and 5 mm from the AC contact (Figures 6.25(a) and 6.26(a)). The presence of this feature, independent of position within the depth of the crystal, suggests this is not an artifact introduced by poor time alignment of pulses with an initially slow rise, but a genuine characteristic of the charge collection at strip boundaries.

Although extensive electric field simulations and experimental data across the DC strip would be required to fully explain this feature, some speculative arguments shall be

discussed here.

As described in Section 4.1, the majority charge carriers on the AC (DC) contacts are the holes (electrons). The bias voltage is applied to the AC contacts, therefore the region of strongest electric field is in the vicinity of the DC contact. The observations imply that at least the holes migrate through the crystal with reduced velocity at strip boundaries. The possibility that the holes are becoming trapped in the crystal lattice, as is often seen in cadmium zinc telluride, is unlikely as this would not be dependent on the position across the strip. A more convincing hypothesis is that the applied electric bias is not sufficient to saturate the drift velocity of the holes throughout the width of the strip, but only (if at all) at the strip centre. As the electric field is understood to be weaker at strip boundaries, these would be the first crystal regions to demonstrate such effects. Furthermore, the extent by which the pulses are slower at strip boundaries is slightly reduced for positions

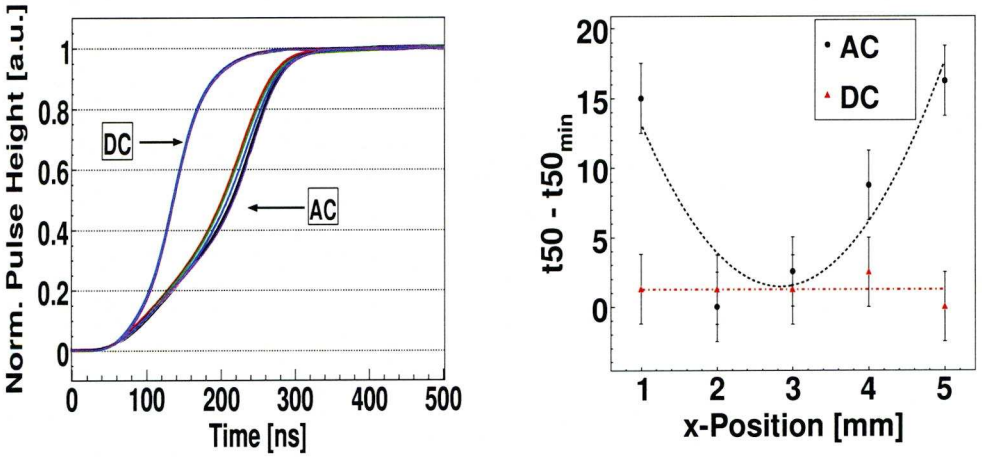

(a) (b)

Figure 6.25: (a) Average pulse shape sampling across the at the centre of the crystal. Slower risetimes are observed toward the boundaries of the strip for the AC pulses. (b) The $t50$ - $t50_{min}$ values for both the AC and DC pulse shapes as a function of lateral position. The $t50$ values highlight the reduced charge collection time close to strip boundaries on the AC side.

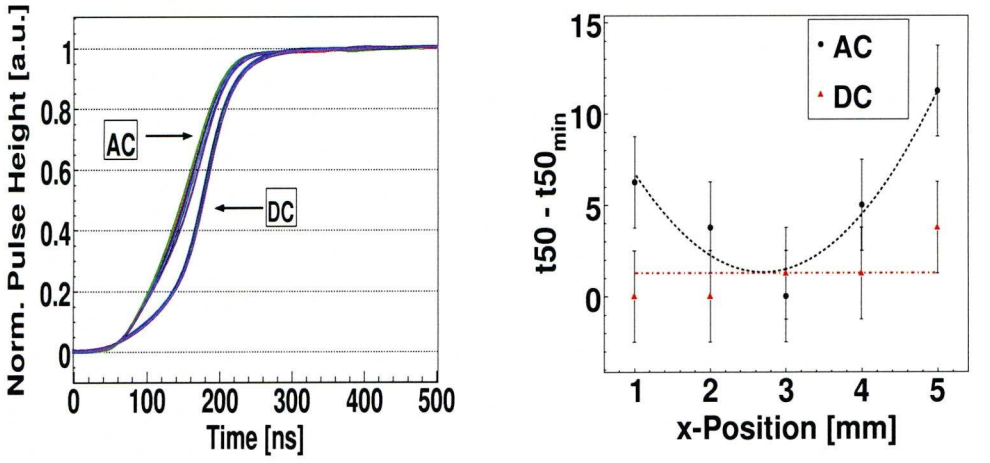

(a) (b)

Figure 6.26: (a) Average pulse shape sampling across the AC strip 5 mm away from the AC side. The AC pulses are marginally slower toward the boundaries of the strip. (b) The $t50$ - $t50_{min}$ values for both the AC and DC pulse shapes. The t50 values highlight the reduced charge collection time close to strip boundaries on the AC side.

close to the AC contact (Figure 6.26). The holes created at these positions would spend the least amount of time in the weaker field near the AC contact, therefore they are exposed to the possibly weaker field for shorter distances. This may explain why the effect is reduced at these positions. As mentioned above, further information could be gained from detailed studies of the electric field (whether experimental or simulated) focusing on the pulse shape properties at different bias strengths and with different contact geometries. For such work to take place in a model, a validated pulse shape simulation package is required. This issue shall be addressed briefly in Section 6.12, but a more thorough investigation is recommended in future.

6.9.4 Mean Position Error

As a final metric of the position accuracy, the *mean position error* is calculated by averaging the distance between the true collimator position and the position determined using the database's entry of minimum χ^2. Figure 6.27(a) is a plot of the mean position error in the depth dimension of the detector as a function of collimator position. The values lie between 0.1 (1) mm and 1.5 (1) mm; the average of the 20 results is 0.6(1) mm. Closer inspection of Figure 6.27(a) reveals a position dependence on the mean position error as has previously been indicated in the accuracy plots (Figure 6.21), the position histograms (Figure 6.22) and will feature in the sensitivity measurements (Section 6.11.1). The mean position error is slightly larger close to the DC face (Position 1) with the highest values between three millimetres and five millimetres away from the DC contact. The mean position error then follows a practically constant trend in the range between six millimetres and eleven millimetres only to indicate a linear decline from twelve millimetres onwards. This trend implies the ability to localise interactions accurately is enhanced when the interactions are near the AC contacts. A full explanation for this behaviour is discussed in Section 6.12 once further evidence has been presented. Briefly, it is believed that the observations due to the poor mobility of the hole in regions of the detector, where the electric field is weakest (near the AC face). If the drift velocity of the less mobile hole is not saturated, an insensitivity in the pulse shape to different positions may be present. This will have least effect close to the AC face, as the hole is collected quickly and removed from the charge induction process. This explains the improvement in position resolution. Figure 6.27(b) displays the mean position error measured laterally across the strip for three lines using the χ^2 closest match approach: 5 mm from the DC side (blue triangles), 10 mm from the DC side (red, open circles) and 5 mm from the AC side (black, closed circles). For these data, a position dependence can be observed close to the AC (black, open circles) and DC (blue triangles) faces, where the mean lateral position error increases in the centre of the strip. This corresponds to regions of low magnitude image charges on either side, which may explain the trend. Also, Figure 6.14 indicated that, in this region, the image charges are dominantly bipolar, especially on the AC face. This

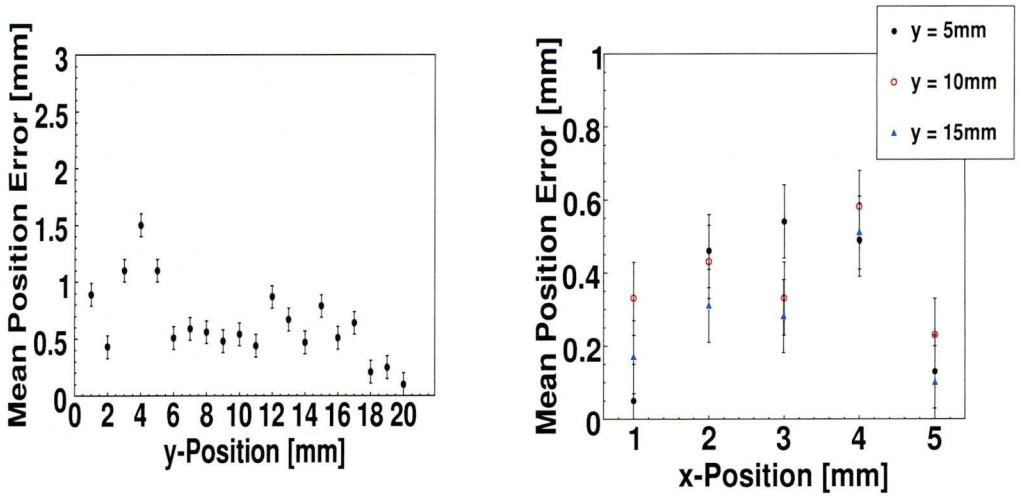

(a) (b)

Figure 6.27: (a) The mean depth position error in depth dimension for the 20 collimator positions. (b) The mean lateral position error for three sets of five data points across a strip. The three sets correspond to the lines across the AC strip 5 mm from the DC face (blue triangles), at the centre of the strip (red, open circles) and 5 mm from the AC face (black, filled circles).

makes not only their alignment, but also their matching process, more difficult. This lack of accuracy toward the centre of crystal segments is consistent with work presented in [Rad09]. The same trend is not found in the centre of the strip, most likely due to the bipolar nature of both image charges for these interaction positions.

6.10 Matching Uncollimated Data

The real challenge to the iterative data matching process and the accuracy of the pulse shape database lies in identifying the positions of uncollimated γ-ray interactions. To address this point, data were acquired using an uncollimated ^{137}Cs point source ($E_\gamma = 662\,\text{keV}$). The caesium isotope was selected for its monoenergetic decay chain and its relatively high energy. The energy ensures the γ rays bear enough momentum to penetrate significantly

into the germanium crystal. A fold <1,1> restriction was applied and the data were extracted from the MTsort analysis package [MTS] using the 3100 x N matrices discussed in Section 6.7. To avoid disturbing the setup, the source was placed in between the germanium detector and the secondary collimators. Regrettably, this has introduced artifacts through backscattered γ rays, which shall be discussed below.

6.10.1 Structure of the algorithm

Initially, a single site interaction was assumed and the real charges from both the DC and AC faces of the voxel were matched with each position in the database using the iterative time alignment procedure. The AC and DC waveforms were compared independently, producing a suggested position for both faces. Depending on the separation between these positions, the degree of confidence on the identification was assessed. Based upon the accuracy plots generated in Section 6.9.1, the database could be accountable for an uncertainty of ± 1 mm. Therefore a disagreement of between 1 mm and 4 mm (inclusive) was attributed to the general uncertainty within the matching process. In this case, the estimated position was constructed using an average between the depths, weighted according to the individual χ^2 parameters. An interaction where both AC and DC matching agreed on the interaction site was treated as correctly matched. Larger separations (>5 mm) qualified the pulse to be constituted of multiple interactions in which case a more sophisticated deconvolution section of the algorithm was activated (see Section 6.11).

6.10.2 Identification Performance

Figure 6.28(a) presents a spectrum obtained counting the positions of best match for fold <1,1> pulses in the voxel shared between AC05 and DC09, while Figure 6.28(b) is a Monte-Carlo prediction of the clustered γ-ray interaction position using the model described in Section 6.6. The first observation made when comparing the figures is that the experimental reading suffers from disappointingly low statistics. Regrettably this implies only speculative arguments can be made, however some trends will be discussed. Firstly, both figures demonstrate a consistent reduction in intensity from the positions

closest to the source at 0 mm (close to the DC face) into the 14 mm depth region. Only the simulated results have sufficient statistics to highlight the exponential nature of the distribution. Secondly, both position spectra show an unexpected increase in counts from ~15 mm onwards until the end of the crystal. Through the Monte-Carlo simulations, it was deduced that this trend is only present if the copper plate, on which the secondary collimators and the point source were positioned, is included. Large angle Compton scattering (backscatter) upward from the copper plate could explain this observation. In the experimental data, the increase in counts toward to 20 mm deep region (near the AC face) of the crystal is higher than in the simulation. Although a statistical nature cannot be ruled out, it is possible that unmodelled materials from which backscatter can occur (e.g. tables, metal holding structures) could be responsible for this. Overall the agreement is encouraging, yet data with higher statistics are required to add weight to the discussed arguments.

Figure 6.28(c) summarises the separation between the lowest χ^2 match from the AC and DC faces respectively. The figure conveys that the matching process results in an agreement of 2 mm or better between the faces for the majority of events (76%). As mentioned above, only the events with a separation of five or greater were classed as convolved interactions and excluded from Figures 6.28(a) and 6.28(d). A more sophisticated method for identifying convolved interactions is discussed in Section 6.11.

6.10.3 Two-dimensional Identification Performance

The matching process of uncollimated data as explained in Section 6.10.1 was combined with the lateral position determination algorithm described in Section 6.9.2 to generate a two-dimensional map of the γ-ray interaction site. The three-dimensional positions were projected through the DC strip plane for two-dimensional plotting. The intensity of interactions as a function of two-dimensional position is displayed in Figure 6.28(d). The zero coordinate in the y-axis corresponds to the DC face. The effects discussed above are visible along the depth of the crystal (y-axis). Furthermore, intensity reduces towards the edges of the strip. This feature is introduced by the fold <1,1> condition. As the AC

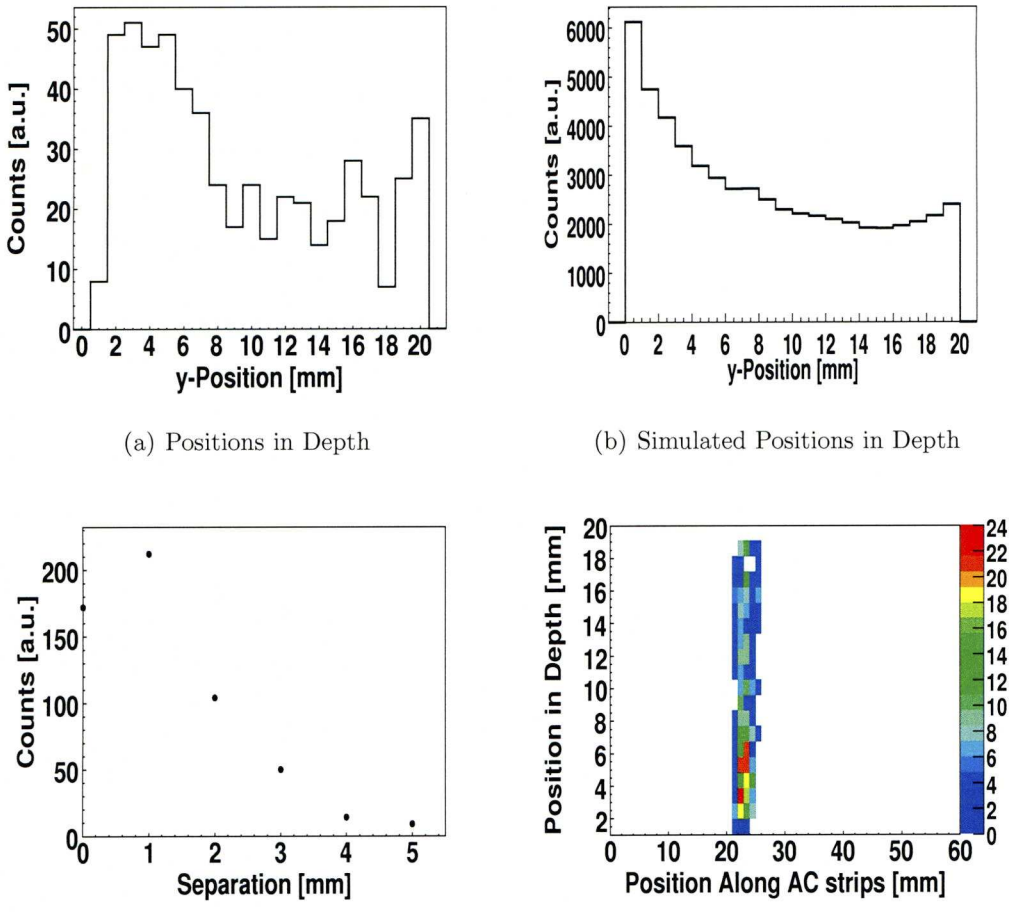

(a) Positions in Depth

(b) Simulated Positions in Depth

(c) AC and DC Difference

(d) Two-dimensional Positions

Figure 6.28: The weighted depth position calculated by comparing the match between AC and DC pulse shapes with the database (a) and the positions predicted by a Monte-Carlo model (b). The frequency of the separations between AC and DC position is presented in (c), while (d) represents a two dimensional histogram of the positions of the uncollimated data as determined by the database. For this plot, the real charges were employed to match the depth while the lateral coordinate was extracted from comparing the image charges.

side is approached the intensity of interactions are distributed more uniformly. This is again believed to be due to the reduction of the backscattered γ rays in this region of the crystal. The lack of increments in some pixels and an increased intensity in some edge pixels close to the AC side may be genuine artifacts, but a statistical origin is a more obvious explanation, given the available data, and cannot be ruled out.

6.11 Pulses Containing Multiple Interactions

To gain a more detailed understanding of the charge pulse induced by multiple interactions within a segment, a set of *convolved* pulses (P_C) were produced from the pulse shape database. In this process, two pulses (P_1 and P_2) were summed according to

$$P_C = \frac{E_1 * P_1 + E_2 * P_2}{E_1 + E_2}, \tag{6.4}$$

where E_1 and E_2 are weighting factors to represent the energy deposited by the two interactions. For example in the hypothetical case of both interactions depositing equal energy, E_1 and E_2 would equate. The energy weighting parameters E_1 and E_2 will later often be quoted as a ratio E_1:E_2. After summation, the pulses were re-normalised to range from zero to unity by dividing by $(E_1 + E_2)$. Convolved pulse shapes were generated for all 390 $(20^2 - 20)$ combinations of interaction positions with energy ratios of 1:1, 3:1, and 9:1. Figure 6.29 illustrates the convolved AC real charges from a set of pulses with $E_1 = E_2 = 1$. In the figure, P_1 was the position closest to the DC face at 1 mm depth and was convolved with all remaining pulses at depths 2 mm-20 mm. This set of pulses will sometimes be referred to as *artificially convolved interactions.*

In the following sections of this document, a high frequency sine wave has been added to oscillate around the pulse to model the effects of electronic noise.
Initial assessment implies that a minimum distance between the interactions is required before the presence of both sites is clear from the leading edge of the waveform. Key parameters in the ability to identify multiple sites are therefore:

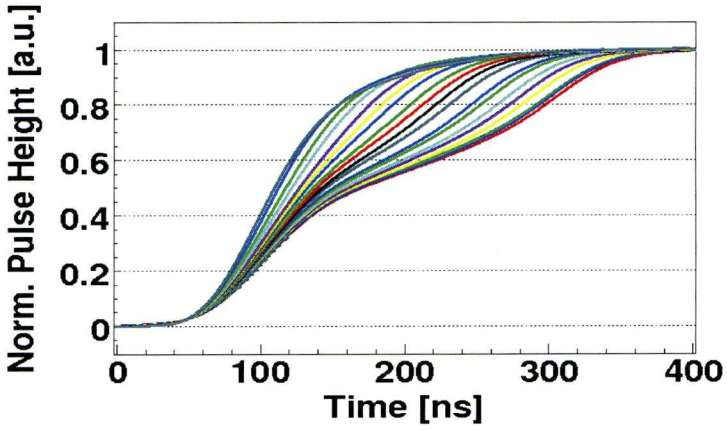

Figure 6.29: Samples of convolved pulse shapes produced using Equation 6.4. Weighting factors of E_1=E_2=1 were used. The twenty displayed pulses are the AC responses from position 1 mm from the DC contact convolved with the twenty other depth positions.

- the sensitivity of the pulse shapes as defined by the weighting field,
- the energy ratio between the two interactions (E_1 and E_2),
- the separation between the two interaction sites.

In this discussion, the sensitivity of the pulse shapes is constant as it is defined by the contact design and applied electric field. This section will therefore aim to establish the limitations of the sensitivity of the SmartPET detector by quantifying conditions required for a convolved interaction to be identified. Pulse shapes produced by more than two interactions have not been considered in this work.

6.11.1 Sensitivity to Convolved Interactions

As with the single site interactions above, the convolved AC and DC pulses (P_C) were iteratively time aligned to each database pulse and the best χ^2 match was obtained using Equation (6.2). In Figure 6.30, the lowest χ^2 value for AC pulse and DC pulse were plotted against each other. This procedure was conducted both for a range of single site pulses from different positions across the coincidence scan (black circles) and for the convolved

pulses calculated with Equation (6.4) (red triangles). For significant fractions of the P_C data, the single site pulse and convolved pulse entries fall into separate regions of the plot for the 1:1 and 3:1 energy ratio. This observation cannot be made for the 9:1 energy ratio parameters in Figure 6.30(c). As the energy imbalance increases, one interaction dominates the pulse shape. The convolved shape closely resembles the dominant single site interaction pulse and the convolution is unidentified. Nevertheless, the regions of the plot can be exploited to define a threshold, representing the worst accepted parameters for an event to still be classed as a single site interaction. In this case, this threshold has been defined as a line $\chi^2_{AC}+\chi^2_{DC} < 20$.

To understand the separation required for multiple interactions to be identified based on the pulse shape, the convolved pulses, which lie outside of the single site acceptance criterion, have been examined more closely. Subfigures 6.31(a), 6.31(b) and 6.31(c) are histograms of the separation between the artificially convolved interactions that were identified by applying this method. Obviously, the convolved data sets contain a larger number of pulses separated by small distances. For example, there are only two available

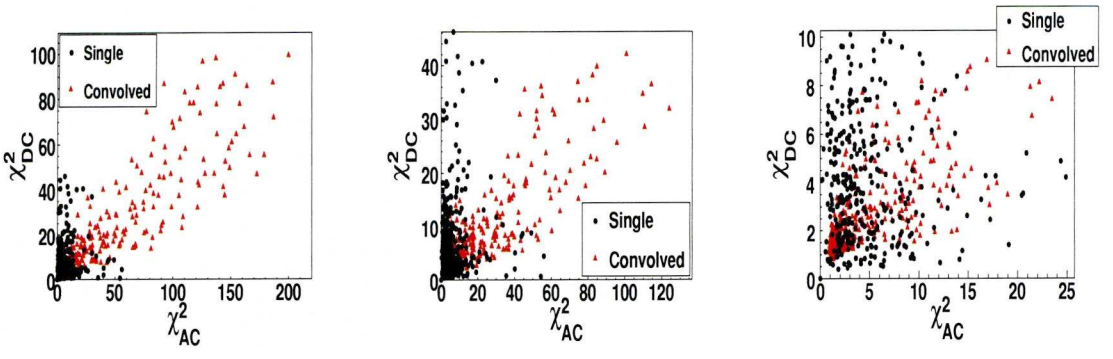

(a) 1 : 1 (b) 3 : 1 (c) 9 : 1

Figure 6.30: The χ^2 value of the best AC and DC matches plotted against each other for single site data (black dots) and convolved data (red triangles). The figure illustrates how the best χ^2 values fall into separable regions of the plot for energy ratios of 1:1 and 3:1. In the 9:1 energy ratio data, one interaction dominates the pulse shape to the extent that the χ^2 parameter often implies a single site interaction.

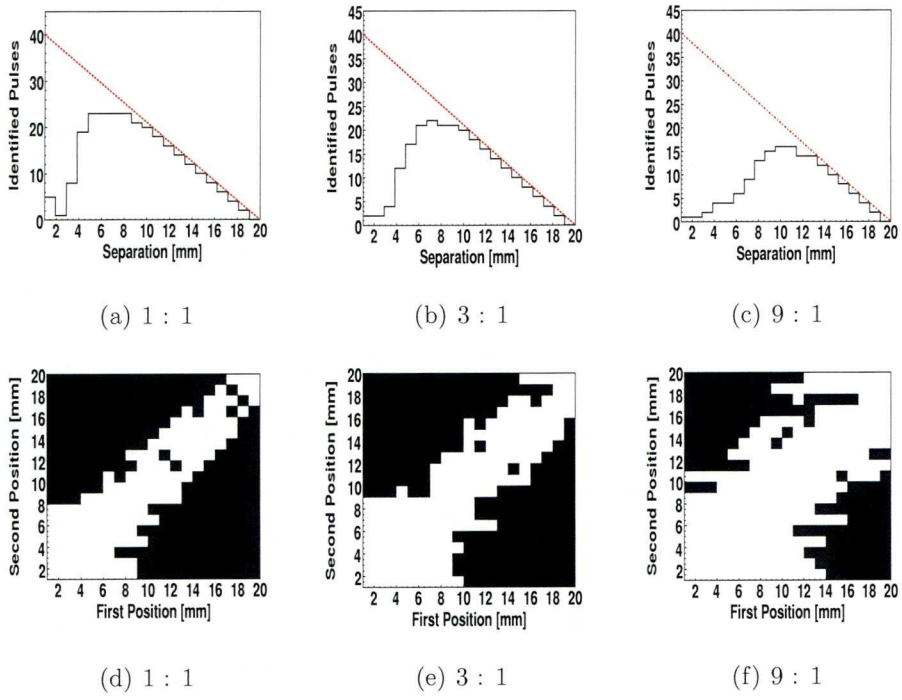

(a) 1 : 1 (b) 3 : 1 (c) 9 : 1

(d) 1 : 1 (e) 3 : 1 (f) 9 : 1

Figure 6.31: (a) - (c) are histograms of the separation between identified convolved interactions. The red line indicates the number of pulses which were available to be identified at that separation. These figures highlight that providing the interactions are separated by ~10 mm or more they should be identifiable with this approach. In (d) - (f) all combinations of convolved pulses are represented by P_1 plotted on the x-axis and P_2 on the y-axis. The matrix entries have been set to unity (black) if the event was successfully identified and to zero (white) if the pulse was treated as a single site interaction. Subfigures (d) - (f) show evidence of an enhanced sensitivity toward the AC contact of the detector (Position 20).

pulses where the individual interactions were 19 mm apart: the two pulses produced by convolution of position 1 with position 20 and vice-versa. Whereas a range of combinations producing pulses 1 mm apart are possible. The number of pulses which were available to be identified at a certain separation is indicated by the dashed red line. The figures illustrate that the separation at which all of the possible events are no longer identified

is ~10 mm. At separations <10 mm, large amounts of the 1:1 and 3:1 energy ratio data (Figures 6.31(a) and 6.31(b) respectively) are still identified. Only at ~5 mm does the method fail to identify pulses at all as the entries in the histogram are around zero. For the 9:1 energy ratio data, this tendency begins at ~10 mm separation but is a more gradual process. In Subfigures 6.31(d), 6.31(e) and 6.31(f), graphical representations of matrices of P_2 vs P_1 are presented. The matrix has been filled with unity if the method was able to identify the pulse as convolved (black) and with zero (white) if the pulse would have been declared a single site interaction. As in the subfigures 6.31(a), 6.31(b) and 6.31(c), it is demonstrated that if one interaction deposits sufficient energy to dominate the pulse shape, a much larger separation is necessary between the interactions for the convolution to be detected. In all three data sets, the distance required between interactions is less when the interactions are close to the AC face (Position 20). Here further evidence is found that there is an enhanced sensitivity of the real charge pulses near the AC side. This is observed at both scan line positions in Figures 6.13 and 6.14 and in the mean position error plots in Figure 6.27. The reasons for these shapes are believed to relate to restricted hole mobility in regions of weak electric field, as touched upon earlier (Section 6.9.4). Extensive electric field simulations may offer a further insight into this issue. These simulations will only be touched upon briefly in this work (Section 6.12). A further investigation into this matter is recommended.

In summary, for multiple interactions in a single segment to be identified, two criteria must be met: both interactions must deposit sufficient relative energy to impact the leading edge of the pulse shape. At an energy ratio of 3:1 or less, this requirement is fulfilled. Secondly, a minimum separation in depth between the individual interactions is necessary. This value is dependent on the region of the crystal the interactions are in. Increased sensitivity is demonstrated near the AC face where a separation of only ~4 mm is needed. Near the DC face, interactions must be separated by ≥10 mm.

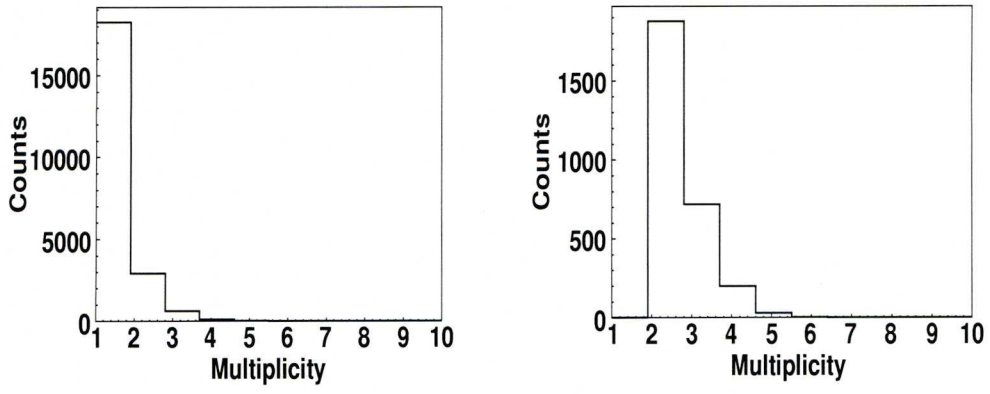

(a) Fold <1,1>

(b) Fold <2||1>

Figure 6.32: Histograms of the multiplicity - the true number of interactions - for both fold <1,1> (a) and fold <2||1> data as calculated in the simulation. (b) indicates that when studying fold <2||1> events, there is an increased risk of an interaction being convolved.

6.11.2 Identifiable Multiple Interactions in Simulated Data

With limiting factors on the ability to deconvolve interactions established, it is essential to quantify the fraction of uncollimated data which is convolved at 511 keV and the ability to identify these events given the sensitivity above. For this purpose, fold <1,1> and fold <2||1> data were extracted from the Monte-Carlo simulations discussed in Section 4.6. To remind the reader, these simulations modelled a monoenergetic (E_γ =511 keV), point source, 25 cm away from the aluminium can of a SmartPET detector. Only one detector was studied in these simulations. For additional details, please refer to Section 4.6. One crucial parameter to extract from these data was the *multiplicity* - the true number of interactions in the detector. The simulations reveal that the fraction of convolved data depends on the fold of the interaction. Figure 6.32 displays histograms of the multiplicity for fold <1,1> data (Figure 6.32(a)) and for fold <2||1> data (Figure 6.32(b)). It was calculated that when using fold <1,1> data - which constitute 62% of the total data - only 12% of the data contained a convolved interaction i.e. a multiplicity >1. This is an encouraging result for the use of the fold <1,1> data subset. The separation in

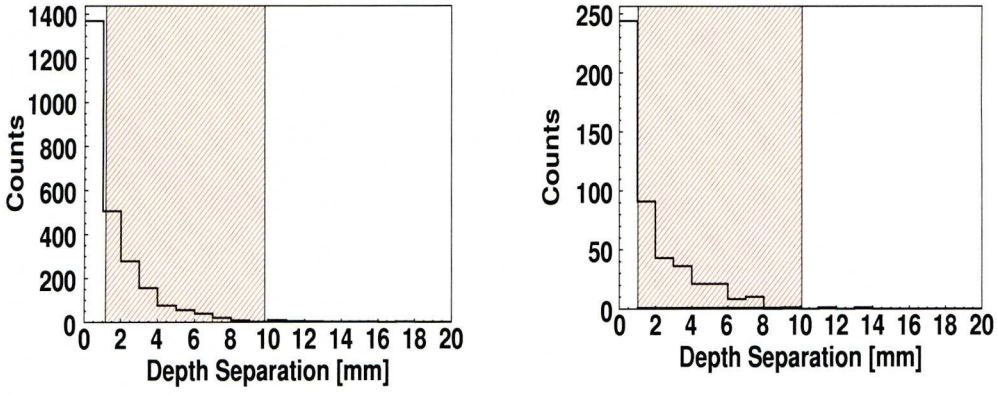

(a) Fold <1,1>

(b) Fold <2||1>

Figure 6.33: Histograms of the depth separation between two components which constitute a convolved interactions for both fold <1,1> (a) and fold <2||1> data as calculated in the simulation. The region shaded in red highlights the convolved interactions of most concern.

depth between the two interactions is the deciding factor in being able to identify the convolved interaction. The simulations indicate that 70% of convolved interactions fulfil the necessary energy ratio requirement, while only 16% are sufficiently separated in depth to be identified. Unfortunately, the two effects are also in competition with each other: only a small initial deposit leaves the original γ ray with sufficient momentum to travel a large distance through the crystal. Therefore if the energy ratio condition is met, it will reduce the likelihood of the separation requirement being fulfilled. The depth separation between the two interactions is presented in Figure 6.33(a) for the fold <1,1> data. The area shaded red highlights the region of interactions of most concern as these interactions have separations large enough to be detrimental to image reconstruction, but, currently, cannot be identified.

For fold <2||1>, the multiplicity values are presented in Figure 6.32(b). This subset consists to 28% of interactions which are in some way convolved. This fraction is over twice the value for the fold <1,1> data. The depth separation (Figure 6.33(b)) indicates

that the interactions are no easier to identify using the current method. The interactions inside the red shaded area result in a mean position error in three dimensions of 3.8 mm for fold <1,1> data and 4.4 mm for fold <2||1> data. For fold <2||1> the issue is further complicated by identifying the strip which contained the first interaction. If this is performed incorrectly, the average position error in three dimensions increases to ~6 mm. Although these statements are concerning, there is much useful information considering future PET system design to be taken from this knowledge. A thorough discussion is found in Section 6.13.

6.11.3 Deconvolving Experimental Convolved Interactions

Having identified a pulse as a candidate for a convolved interaction, the final challenge is to establish the two interaction sites which produced it. For this purpose, data were acquired using the SmartPET1 detector and an uncollimated ^{137}Cs source (E_γ =662 keV). Fold <1,2> events were selected in the MTsort environment [MTS] and analysed in the ROOT environment [ROO] as in Section 6.7. These fold <1,2> events must contain a pulse shape convolved from at least two interactions on the AC side as two hits were registered on the DC face. The methods described in Section 6.11 were applied and identified 20% of the data as convolved. Although 100% of the data must be convolved, a significantly lower fraction will be recognised due to insufficient separation of the interactions in depth. The 20% of events diagnosed as multiple site events is in reasonable agreement with Monte-Carlo simulations which indicate that 13% of fold <1,2> data are separated by 10 mm or greater. The additional fraction of interactions may arise from random coincidences between prompt γ rays, lead X-rays and/or γ rays which have backscattered off the secondary collimators.

To separate the individual interactions, which have resulted in the convolved pulse shape, these were compared with the database of convolved interactions produced using Equation 6.4 with energy ratios 1:1, 3:1 and 9:1. The best match was declared to contain the two combinations most likely to have produced the observed pulse shape. In Figure 6.34 two examples of the experimental, convolved AC pulses (black) are presented

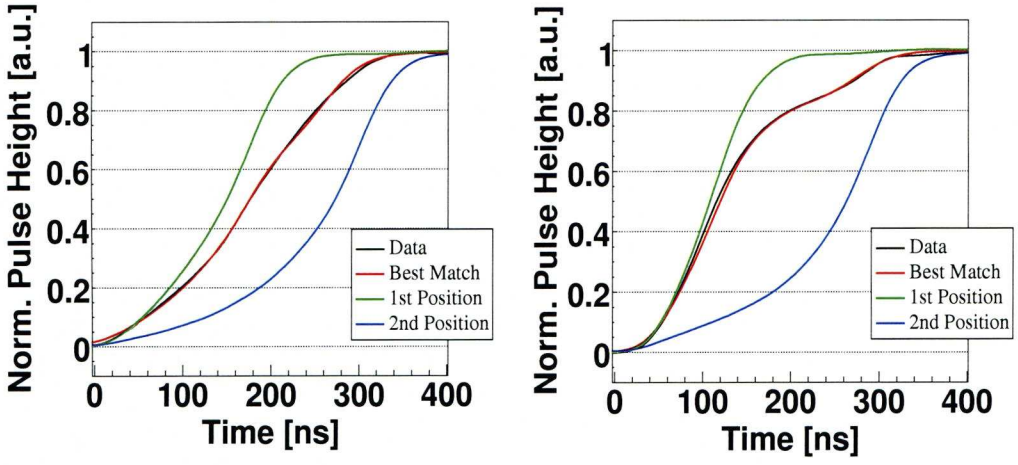

(a) (b)

Figure 6.34: Two examples of convolved experimental AC pulse shapes which were identified and separated (black). The best match with the convolved databases are also presented (red). (a) was determined to have an approx. 1:1 energy ratio between the interactions which were 10 mm apart. The AC response from the individual positions are shown in green and blue. The second example had an energy ratio of 3:1 in favour of the shallower interaction (green) and the positions were 13 mm distance from each other.

alongside the best AC match from the databases (red) and the two single site positions, which result in the convolved pulse (green and blue). The pulse in Figure 6.34(a) was determined to have an energy ratio of 1:1 between the two interactions and according to the matching process they were separated by 10 mm. For the pulse in Figure 6.34(b) the two interactions had an energy ratio of 3:1 in favour of the position closer to the DC side (green). The separation in depth between the two sites was calculated to be 13 mm.
Although this process appears to reproduce the shape of the real pulses accurately, it has speed limitations and would not be suited for online analysis. The least squares matching requires ~9 sec per event on a FUJITSU SIEMENS laptop with an Intel Centrino Duo dual core processor of 1 GHz and 1 GB of RAM. Further work will be required to develop the algorithm at both the identification stage and the pulse deconvolution stage. It is recommended a more sophisticated algorithm is generated in the future. One suggestion would be an adaptive grid search technique [Ven04] or a singular value decomposition [Dox07]. This shall be discussed in more detail in Chapter 7.

6.12 Charge Pulse Simulations

The characterisation measurements above and the pulse shapes presented in Figures 6.13 and 6.14 are also important in verifying waveforms from *electric field simulations*. A validated electric field simulation is a crucial tool in system modelling and design as it can predict the pulse shapes of an interaction, before the detector is assembled. This is necessary to anticipate position resolution performance (Section 6.9) and sensitivity limitations as discussed in Section 6.11. A dependable electric field simulation is also often utilised as an alternative to the characterisation methods outlined above, to reduce the time required to generate a pulse shape database.
In an electric field simulation, the pulse shape induced on a detector contact is calculated by applying the Schockley-Ramo theorem [Ram39] as described in Section 3.3.3. In this work, the Multi-Geometry Simulation (MGS) package [Med04] was employed to calculate the pulse shapes induced on the SmartPET contacts. The following calculation stages are

necessary for the software to produce the theoretical waveforms:

- *Geometry*

  The user must describe the detector geometry as a set of input parameters. Decisive factors in this stage include the size of the crystal, the operating bias voltage, the impurity concentration, the cryostat temperature, any spacing between the crystal and the cryostat, the inter-strip gap and the contact thickness. In the case of a coaxial detector, properties regarding the bore hole must also be entered.

- *Electric Potential*

  With this information the software calculates the magnitude and direction of the electric potential ($\psi(x, y, z)$) throughout the crystal by solving Poisson's equation

  $$\frac{\partial^2 \psi}{\partial x^2} + \frac{\partial^2 \psi}{\partial y^2} + \frac{\partial^2 \psi}{\partial z^2} = -\frac{\rho(x, y, z)}{\epsilon}, \tag{6.5}$$

  where $\rho(x, y, z)$ represents the volumetric charge density as calculated by the impurity concentration gradients.

- *Electric Field*

  The electric field $\vec{E}$ is then calculated according to

  $$\vec{E} = \vec{\nabla}\psi. \tag{6.6}$$

- *Charge Carrier Drift Velocities*

  The strength and vector of the simulated electric field is combined with knowledge of the crystal lattice to calculate the trajectory of the charge carriers. MGS applies mobility parameters for electrons and holes calculated in [Mih00] and [Bru06] respectively.

- *Weighting Field and Pulse Shapes*

  Finally, the weighting field as described in Section 3.3.3 is calculated from the electric field and combined with knowledge of the charge trajectory to obtain the current

  $$i(t) = q\vec{v_d}E_0(x, y, z), \tag{6.7}$$

where q is the charge carrier in the crystal, $\vec{v_d}$ is its drift velocity and E_0 is the weighting potential at a given coordinate. The charge pulse $Q(t)$ is calculated by summing the integrals of the current induced on a contact by both charge carrier species.

When simulating the SmartPET charge pulses, it was observed that the calculated pulses become unusable for significant regions of the crystal near the detector guard ring. If the interaction point is within 10 mm of the guard ring, the charge carriers are not drawn toward their respective contact but toward the guard ring itself. As part of this investigation, it was noticed that the default SmartPET parameters stored in the software do not agree with the values in the SmartPET data sheet [San05a]. Using the default parameters, the issue affects the two most outer strips on each face (AC01, AC02; AC11, AC12; DC01, DC02; DC11, DC12); entering the correct specifications improves this issue, yet does not resolve it completely as *boundary strips* (AC01, AC12, DC01, DC12) are still affected. The correct parameters entered into MGS from the SmartPET data sheet are documented in Table 6.4.

Figure 6.35 illustrates the pulse shapes calculated by MGS for the points which produced Figure 6.13. To aid the comparison, Figure 6.13 is repeated overleaf. A number of features are observed in the simulated pulses which do not agree with the experimental measurements. The first would possibly be rectified by the inclusion of some hardware effects, the others are more complicated:

- *Sharp and abrupt shape in simulation*
  The simulated pulse shapes have less rounded curves and the points at which the charge changes from being induced by the hole and electron current is clearly visible. This is not the case for the experimental shapes. Previous pulse shape simulations [Dim08, Kha08] indicate that this effect is at least reduced, if not removed, when including the response of the preamplifier. As the capacitor discharges, the escaping charge slows the pulse shapes delivering a more rounded shape. This feature may also be minimised when the sampling frequency of the GRT4 cards of 80 MHz is included.

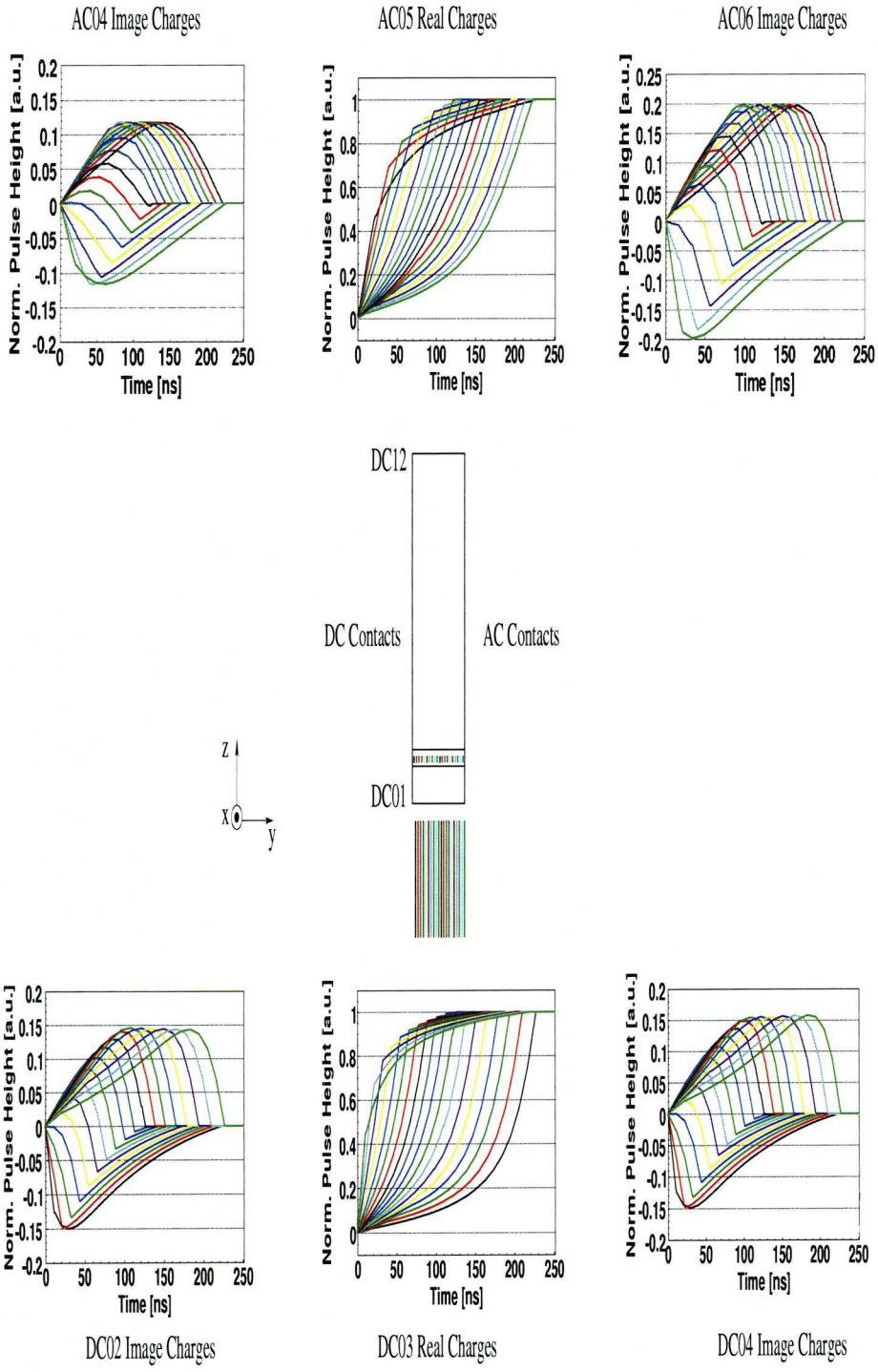

Figure 6.35: The simulated charge response as calculated by MGS for eighteen positions through AC05 and DC03.

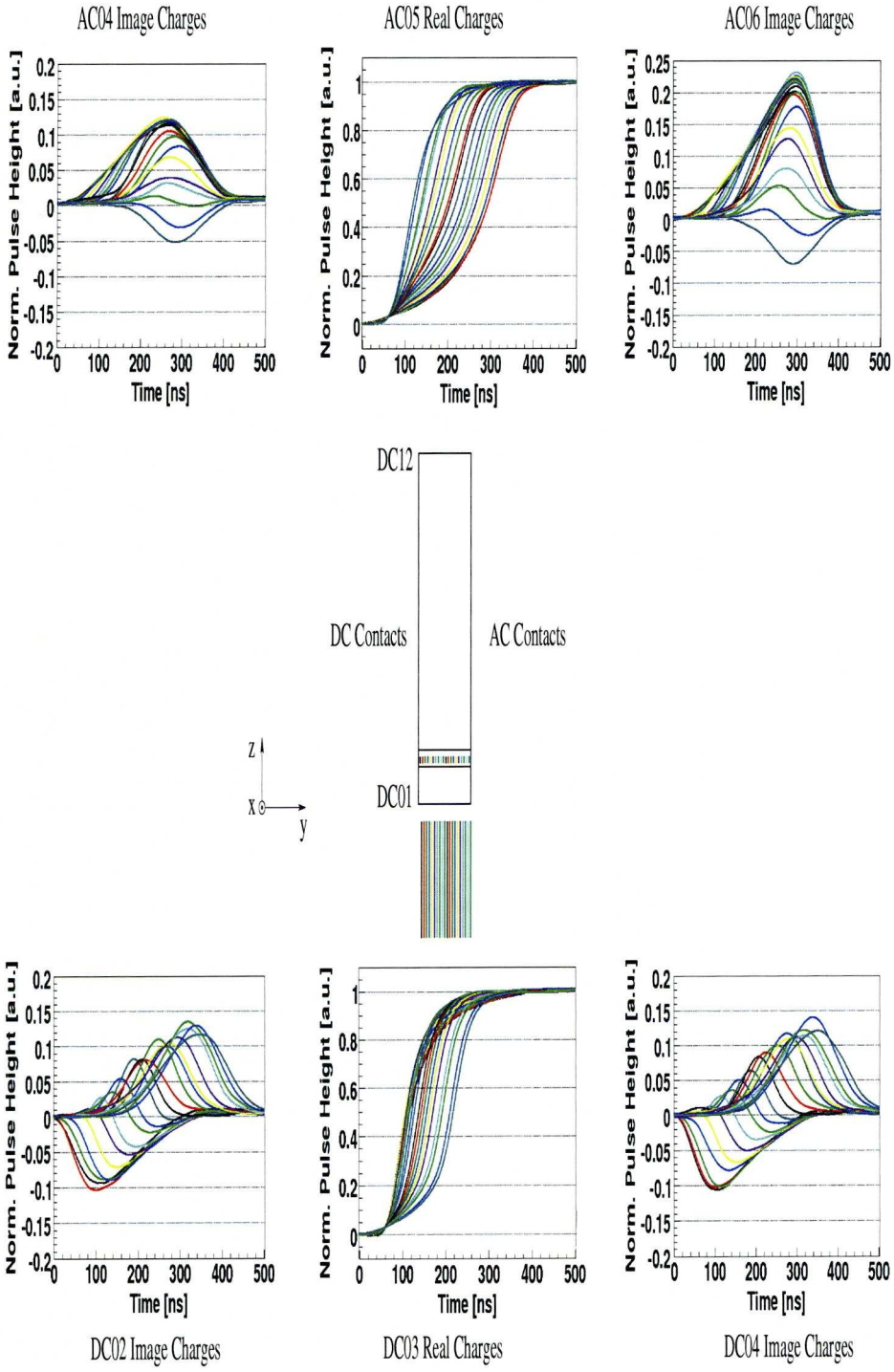

Figure 6.36: Experimental pulse shapes for the twenty interaction positions in the voxel shared between AC05 and DC03.

Parameter	Value
Active Width	60 mm
Guard Ring Width (each side)	7 mm
Active Length	60 mm
Guard Ring Length (each side)	7 mm
Active Depth	20 mm
Potential AC contact	-1800 V
Potential DC contact	0 V
AC Contact Thickness	0.3 μm
AC Contact Inter-strip Gap	180 μm
Distance to Front Window (AC)	15 mm
DC Contact Thickness	0.3 μm
DC Contact Inter-strip Gap	180 μm
Distance to Front Window (DC)	15 mm
Impurity Concentration	$\sim 6 \times 10^9$ per cc

Table 6.4: A table of the input parameters required by MGS taken from the SmartPET data sheet [San05a].

- *Difference in Risetime*

  The charge induced in the DC side of the pulses has an approximate full collection time ($t100$) of 200 ns. Due to the uncertainty in the beginning and end of the experimental pulses, the experimental $t100$s are harder to define, however an approximate observation shows reasonable agreement with the simulation. Despite uncertainties, it is undeniable that this is not the case for the AC pulses. They require at least 50% longer to reach full charge collection in experiment than in simulation. As the AC side collects the holes, this observation implies the holes are perhaps not migrating through the crystal as easily as in the model. This supports the postulate in Section 6.9.3 that the applied bias may be insufficient to fully saturate the hole drift velocities and that issues regarding their mobility are being discovered.

- *Image Charge Polarity*

  The magnitude and shape of the image charges also differs between simulation and real data for the AC responses. While the experimental DC image charges display approximately the same number of positive and negative image charges, the experimental pulses induced on the AC side are predominantly positive. This effect is highlighted in Figure 6.37 where the total, positive (+ve) and negative (-ve) image charge integrals are plotted as a function of depth position. These figures supply further evidence, that the point of symmetry in the electric field is around the centre, as would be expected. However, for the image charges on the AC side there are significantly more image charges of positive polarity than negative polarity. The point of symmetry in the electric field is very close to the AC side. This shape has previously been observed in experimental image charge pulses in SmartPET [Tur06], but only on the AC side. [Tur06] also demonstrates, that this phenomenon is only present in the AC nearest neighbour image charges. When examining the charge on next-to-nearest neighbouring segments (i.e. AC03 and AC07 in this case), the effect vanishes. This behaviour can be confirmed by this study. Further evidence is supplied in Figure 6.37(c), where similar behaviour is demonstrated in experimental $T90$ values for the AC and DC pulses. The shortest $T90$ on the DC side is approximately central; on the AC side this is not the case.

The differences in risetime and image charge behaviour between the two detector faces and the simulation model may offer the explanation into enhanced position resolution near the AC contact. The reader is reminded that the electrons - whose drift velocity is expected to be saturated - are collected on the DC contact. The holes - where evidence suggests their velocities may not be saturated - migrate toward the AC contact. Electron-hole pairs created near the AC face, where the field is weakest, have the shortest time of the pulse induced by the less mobile holes. Therefore a slight increase in sensitivity for these interactions can be explained.

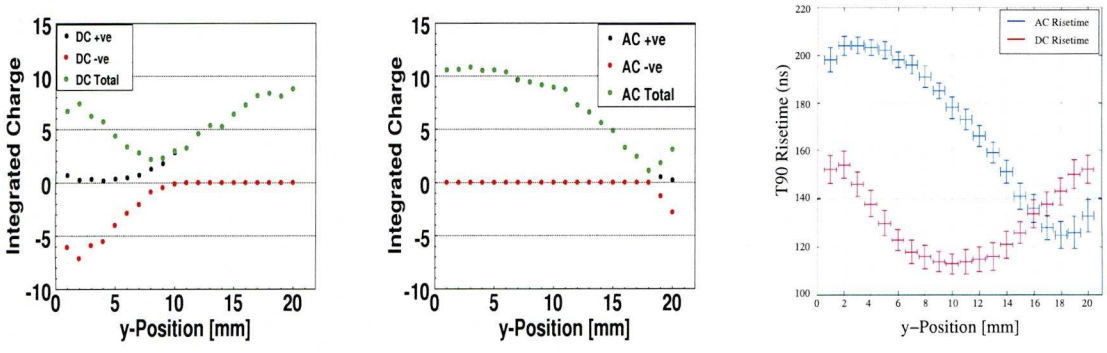

(a) DC Image Charges (b) AC Image Charges (c) Real Charges

Figure 6.37: The experimental positive (+ve) and negative (-ve) components of the image charge integral as a function of interaction position depth. The DC image charges (a) are near symmetrical around the centre of the crystal. This is not the case in the AC image charges (b). In previous characterisation work, similar effects have been observed in real charges on the AC face. An example (c) is taken from [Coo08].

6.13 Characterisation Discussion

The aims of this chapter were to enhance the overall position sensitivity of the SmartPET detector with particular regard to PET imaging. The ability to identify and potentially deconvolve multiple interactions within a voxel was also to be evaluated. Figures 6.27(a) and 6.27(b) contain values of the average error between the collimator position and the best match retrieved with the database. These values indicate that the matching process developed in this work accurately determines the interaction position down to the 1 mm level for single site interactions. These values are consistent with recent publications e.g. [Kha08]. A method for identifying convolved interactions has also been developed. This allows the majority of events which result in large position distortions to be identified. However, simulations indicate that the majority of convolved interactions are not separated by sufficient distance to be picked out using the current routine. This issue can be addressed in several ways. The first is to continue work on the identification and deconvolution routine. In [Kha08] a more sophisticated identification routine, developed as part of the DESPEC project [Pod05], is described for use with planar detectors. In

[Kha08], pulse shapes are converted into meta-signals and positions are retrieved by multiplying with a matrix of all possible database meta-signals. An additional option would be to investigate current pulses ($i(t)$), as they can be more sensitive to the presence of additional interaction sites. Looking further into the future, these considerations could be taken into account at the design stage of a new project, where again two schools of thought exist. One would aim to enhance the sensitivity of the pulse shapes and reduce the separation limit necessary for convolved hits to be identified. Many projects in the detection of neutrinoless double β decay ($0\nu\beta\beta$) operate along these lines, although they aim to detect much higher energy γ rays. Detectors with point-like contacts are often applied as the shape of their weighting field means most of the current is induced when the charge carrier is in close proximity of the contact. This allows the separation between interactions to be exaggerated in the leading edge of the pulse. The other would argue that the mean free path of the γ rays should be altered by choosing a different material. Either a lower Z material, to encourage γ ray scattering and ensure large, resolvable distances between interactions; or a higher Z to restrict the scattered distance so that single site or scatters within a small volume are maximised. A full discussion of these techniques and systems which apply them is featured in the next chapter.

Chapter 7

Conclusions & Discussion

The results presented in this study have demonstrated the potential abilities of a PET imaging system using high-purity germanium detectors. Experimental measurements have been carried out in parallel with a validated system model to approach the highest possible image quality. The model was experimentally validated over an energy range of 80 keV - 1408 keV, where an excellent agreement is presented. The simulation then acted as a platform for developing analysis techniques and sources of image resolution distortion. These results are interesting from both a system development/improvement and a fundamental point of view and concentrated on the positron range, detector position resolution, interaction clustering and first hit identification. The parameters with the largest impact on image resolution were the lateral position resolution in the detector and the correct ordering of the events. A γ-ray tracking algorithm was applied to aid in the problem of event ordering. Although the approach is reliable and, according to the simulation, retrieves the first hit for up to $\sim$80% of the data, it is limited by the clusterisation of interactions. Despite the fact that the clusterisation itself only introduces minor blurring to a reconstructed image, it reduces image quality indirectly, by distorting the parameters with which a tracking algorithm operates, most significantly the deposited energy.
The latter half of this work has addressed this issue by constructing a pulse shape database from an experimental detector characterisation. Using the pulse shape database, the position resolution for single site interactions has been reduced to around $\sim$1 mm in all three

dimensions with the magnitude of the mean position error equating to 0.78(1) mm. The database has also been employed to identify and deconvolve multiple interactions in a segment. With the currently presented algorithm, convolved interactions must be separated by ~8 mm before they are clearly distinguishable from single site events. However, this analysis stage is not yet perfected and will require further work. A discussion of the current status, limitations and potential improvements are provided below.

7.1 SmartPET Status & Further Work

Attention shall be drawn specifically to the following areas of the SmartPET project:

7.1.1 Efficiency

Using the current 2.5 D reconstruction algorithm, the efficiency of the detectors cannot be improved significantly without the inclusion of additional detector material. The rotation correction discussed in Section 5.3.3 allows LORs to be reconstructed independent of their angle of incidence. Further LORs could only be utilised in reconstruction with a 3 D algorithm. It is suggested that other areas of the project are the focus of more immediate investigation.

7.1.2 Position Resolution

Excellent position resolution has been demonstrated using the pulse shape database derived in Chapter 6. The use of the database has confirmed that sub-millimetre resolution can be achieved for single site interactions. The largest error in this process is a result of poor time alignment, which can be overcome by an iterative matching approach. Using the iterative time alignment (Section 6.8.3), over 95% of events were correctly positioned within 1 mm of the true interaction position and a mean position error of 0.78(1) mm is calculated. The database has also been applied to uncollimated data. Simulations indicate that the impact of the position resolution on a reconstructed image is most crucial,

therefore achieving this level of confidence at the millimetre level is therefore a highly encouraging result.

7.1.3 Sensitivity to Multiple Site Interactions

The pulse shape database has also been exploited to identify and separate multiple interactions which occur within the same detector voxel or segment. In this case, the summed pulse shape must be deconvolved to retrieve the true number of interactions and their original positions. An algorithm has been formed to address this issue by comparing artificially convolved pulses with the single site interaction pulse shapes. For a fixed weighting potential, the impact of the multiple interaction sites on the pulse shape depends on their separation and the energy ratio between the two interactions. Results depict that a separation of 8 mm is required to identify convolved pulses at a 3:1 energy ratio or less. For greater energy ratio values, the separation needed increases. For interactions in real data, where these conditions were met, interaction deconvolution has been demonstrated. Unfortunately, only few clustered interactions fulfil, these requirements as the separation at 511 keV is typically <4 mm. This leaves three options which should be investigated as part of further research:

- *Refinement of the algorithm*
  This research step is absolutely essential as a number of more complex avenues for pulse shape decomposition remain unexplored. Some examples include using a *folding algorithm* [Gat01] to reliably obtain the true multiplicity or a *singular value decomposition algorithm* [Dox07] to develop the χ^2 matching stage. An exploration into the use of current pulses (i(t)) is also highly recommended.

- *Optimisation of the pulse shapes*
  Dependent on the outcome of the bullet-point above, it may be necessary to redesign the contact geometry to produce pulse shapes more sensitive to clustered interactions. One option would be to implement a point-like contact, which is implemented in commercially available Broad Energy Germanium (BEGe) detectors.

These devices have demonstrated high sensitivity to convolved interactions [Bud08]. A disadvantage to this method is the prolonged charge collection, which would be coupled to count rate restrictions.

- *Investigation into other detector materials*
  Should it become apparent that deconvolving typical event clusters in germanium at 511 keV is unrealistic, then an evaluation of other detector materials may be advantageous. Replacing germanium with materials with a lower(higher) atomic number (Z) would lengthen(shorten) the absolute distance between interactions. For lower Z materials, this would ease their deconvolution and γ-ray tracking. It would reduce the need for tracking in higher Z materials as a larger fraction of the γ rays would be stopped in a single energy deposit.

7.1.4 Electric Field Simulations

Electric field simulations have been performed to produce the experimental response of the SmartPET detector. The applied software (MGS) still has many outstanding issues and, regrettably, its development is no longer being pursued [Dim08b]. One issue is the failure to produce sensible pulse shapes in boundary strips. A large dependence on the impurity concentration has already been demonstrated for this phenomenon. Once this problem is addressed, more subtle differences can be investigated.
Valid electric field simulations offer a vital insight into the performance of a detector without the need for detector manufacture, construction and characterisation. They also assist in explaining experimentally observed phenomena e.g. Section 6.9.3 and Figure 6.37 as parameters can individually be adjusted to reproduce a behaviour. A full validation and implementation of an electric field simulation is an imperative requirement, not only for the fundamental understanding of charge collection in planar detectors, but also for the design of a new system. Whether the simulated pulses are obtained using MGS or an alternative software package, is yet to be decided. Should the shortcomings of MGS prevail, either independently written software, as in [Kha08], or commercially available options, e.g. [Ans08], should be explored.

7.1.5 Lyrtech Electronics and Phantom Imaging

A final outstanding work package on the SmartPET project is the commissioning of the Lyrtech digital electronics (Section 4.2.2). The use of this hardware option has several advantages. First, the global clock would make the iterative time alignment redundant, drastically improving the pulse shape matching speed. More importantly, this would allow accurate time alignment of the image charges, mitigating their inclusion in the deconvolution routine.

The most critical reason for this hardware upgrade is the need to image isotopes with short half-lives as these are predominant in clinical use. In order to capture sufficient data within the available half-lives of the nuclide, a high data acquisition count-rate is necessary. SmartPET cannot fully demonstrate a proof-of-principle without imaging a clinically relevant PET isotope. Therefore, it is suggested the phantoms imaged in Section 5.7 should be reproduced experimentally with ^{18}F to verify that reconstructions of more challenging structures are achievable. Once this stage is completed, it is recommended that a characterisation of the full system according to commonly used literature metrics is performed. Although no official literature standard is defined, [Mye02] provides a review of many existing small animal PET systems and offers suggestions towards a literature standard. The SmartPET system must be evaluated in this way for its performance to be compared in similar metrics to its competitors.

7.2 Evaluation & Small Animal Imaging Field

Many small animal PET review papers exist which address commercial systems [Hum02, Lew02, Mye02, Web04]. Some of those most commonly discussed (commercial and research) and some of their properties are summarised in Table 7.1. The full width at half maxima for the reconstruction of a point source are quoted.

An examination of the values in Table 7.1 indicates the SmartPET parameters fall comfortably nicely within the range of commercial and research competitors. While direct comparison proves difficult, as no international standard metrics exist in the small

System Name	Detector Material	FWHM [mm]	Abs. Eff. [%]
MicroPET [Web04]	LSO	1.84	1.22
Quad-HIDAC [Web04]	Avalanche Chamber	~1.0	0.9
SHR-7700 [Mye02]	BGO	2.6	2.3
[Par07]	Si-BGO	1.1	1.0
eXplore VISTA [Wan06]	LYSO and GSO	1.4	4.0
YAP-PET [dGu97]	$YAlO_3$:Ce	1.6	730 cps/μCi
SmartPET	HPGe	1.4	0.97 [Coo07b]

Table 7.1: An overview of the FWHM and absolute efficiencies quoted for several PET systems.

animal imaging field [Mye02], sufficient evidence is provided to state that the SmartPET system certainly meets the standards required in the field. Even some of the highest resolution systems [Ish07, Par07] produce similar reconstructions of point sources to those produced both in this document and experimentally in [Mat06, Coo07b, Coo09]. [Mye02] quotes the size of a rat brain as ~10 mm and a mouse brain ~6 mm. SmartPET's image resolution performance is certainly within specification to image objects of these dimensions.

SmartPET efficiency has been calculated by simulations in this work to lie around 2% with a 13 cm detector separation. [Coo07b] quote a value of around 1%. The discrepancy between the two measurements is most likely to be due to energy gates/thresholds. This issue must be understood, and an experimentally measured efficiency should always be quoted over a simulated value. Either of these values still places the SmartPET performance comfortably amongst the figures quoted for other systems.

The only discouraging result so far remains the unsuccessful experimental imaging of a Jaszczak phantom in [Coo07b]. It shall be argued that this result should not necessarily be interpreted as an argument against SmartPET. The literature review conducted here has not discovered any published images of a Jaszczak phantom matching the measurement attempted in [Coo07b]. The closest is Figure 7 of [Par07], yet only partial volumes

of the phantom were filled with radioactive tracer. To confirm SmartPET's abilities, it is suggested such a partial phantom measurement is conducted as part of further research. These arguments emphasise the urgency of acquiring data with the Lyrtech electronics in order to evaluate SmartPET more thoroughly in a preclinical context.

7.3 Future System Design

Having assessed the potential impact of SmartPET when compared to existing systems, it is important to turn some attention to the future. The most important statements of this thesis shall be summarised and their implications for different materials presented. The conclusions most relevant to this discussion are:

- that image efficiency cannot be increased further without either a 3 D imaging algorithm or thicker germanium detectors.
- that with the current contact geometry and operational bias, evidence suggests the electric field is not saturating the velocity of the holes. This results in regions of the crystal where position resolution and sensitivity are compromised.
- the position resolution and the false ordering of events have the most detrimental effect on image quality.
- sub-millimetre position resolution has been demonstrated for single site interactions.
- position resolution and γ-ray tracking are limited significantly by convolved interactions.
- at 511 keV and in germanium, the distance between two, convolved interactions is $\approx$4 mm.

Germanium

The first two points alone suggest that a selection of several germanium stacks of $<$2 cm thickness, should be opted for over a thicker crystal.

From the point of view of image resolution, the later four observations are decisive. They imply that a system, where the single site interaction data sub-set is maximised, would deliver optimum performance. A system which eases γ-ray tracking, e.g. through encouraging many clearly-defined interactions, should not be discounted. It must be assessed whether a germanium system has the ability to deconvolve interactions separated by 4 mm, yet maintain position resolution of the order of 1 mm^3. Should this requirement not be realised, then germanium may not be the material of choice for small animal PET imaging.

Silicon

While these arguments may cast doubt over germanium's role in small animal PET, other semiconductor materials show more promise. A system based upon tracking clearly-distinguished, multiple-scatter interactions would be feasible with silicon detectors. Its lower Z reduces the effects of Doppler broadening and it can be operated at room temperature. The ability for fine segmentation and some pulse shape analysis would maintain the required high position resolution. Although efficiency would be sacrificed, the fact, that great confidence is ensured in the events which are present, may produce competitive images. Examples of some silicon based PET (and Compton assisted PET) systems are discussed in [dDo06, Par07].

Cadmium Zinc Telluride (CZT)

On the opposing side, cadmium zinc telluride (CZT) offers a higher Z material with greater stopping power than germanium. This will increase the fraction of single-site, full-energy absorptions and reduce the spacing between convolved interactions. The efforts invested into event deconvolution and γ-ray tracking would be spared. The difficulty to manufacture large crystals and limited PSA potential (due to poor charge collection) will be significant issues. The only option to maintain high position resolution may be to produce many, small crystal segments as in [Ish07] at great financial expense.

Fast Scintillator Detectors

It must also be highlighted that the scintillator-field is progressing rapidly and *position-sensitive photomultipliers* (*PS-PM*s), *avalanche photodiodes* (*APD*s) are making great advancements. Recent literature suggests the feasibility of millimetre or sub-millimetre resolution in scintillators [Vin08]. These systems also offer timing resolution of several hundred picoseconds permitting time-of-flight (TOF) PET [Kar08]. Providing this time resolution can be preserved in the electronics, this is a very significant advantage over semiconductors. Should sub-millimetre position resolution and pic-second timing resolution be realised in these devices, semiconductor systems will struggle to compete. The main issue with these systems is the large scale fabrication of the PS-PMs.

7.3.1 Summary

Overall the role of SmartPET in PET imaging will be dictated by the commissioning of the Lyrtech electronics and the success of imaging a clinically relevant isotope, preferably a phantom analogous to those in Section 5.7 or a living organism. It shall be stressed that a high resolution image is not necessarily essential as PET remains a functional imaging modality. An investigation into improving the ability to identify multiple interactions is also encouraged. The role of semiconductor detectors in small animal PET should most certainly not be dismissed as some of the highest quality images so far were produced with these systems [Ish07, Par07]. Germanium, but also silicon and cadmium zinc telluride offer many advantages and their full potential in producing high-resolution images from their position sensitive response is yet to be realised.

Bibliography

[Act03] P. D. Acton & H. F. Kung,
Small animal imaging with high resolution single photon emission tomography,
Nucl. Med. and Bio. **30** 889 (2003)

[Ada94] S. Adachi et al.,
Precise measurements of e^+e^- annihilation at rest into four photons and the search for exotic particles,
Phys. Rev. A **49** 3201 (1994)

[Ago03] S. Agostinelli et al.,
GEANT4 - A simulation toolkit,
Nucl. Instr. and Meth. A **506** 250 (2003)

[Alb08] D. Albani,
Constrained Positron Flight in PET Imaging via Strong Magnetic Fields,
A Senior Honors Thesis, Ohio State Univeristy, (2008)

[Amm08] M. Amman *private communication*

[Ang58] H. O. Anger,
Scintillation Camera,
Rev. Sci. Instrum. **29** 27 (1958)

[Ans08] *http://www.ansoft.com/products/em/maxwell/*

[Aur05] N. Aurichio et al.,
SiliPET: design of an ultra high resolution small animal PET scanner based on stacks of semiconductor detectors,
IEEE Nucl. Sci. Symp. **5** 3010 (2005)

[Bar95] H. H. Barrett,J. D. Eskin and H. B. Barber,
Charge Transport in Arrays of Semiconductor Gamma-Ray Detectors,
Phys, Rev. Lett. **75** 156 (1995)

[Bar04] H. H. Barrett and K. J. Myers,
Foundations of Image Science,
Wiley (2004)

[Bea00] C.W.Beausang et al.,
The YRAST Ball array,
Nucl. Instr. and Meth. A **452** 431 (2000)

[Bea03] C.W.Beausang et al.,
GRETA: the gamma-ray energy-tracking array. Status of the development and physics opportunities,
Nucl. Instr. and Meth. A **204** 666 (2003)

[Bev07] T.E. Beveridge et al.,
Multiple occupancy considerations for the SmartPET imaging system,
Nucl. Instr. and Meth. A, **573** 68 (2007)

[Bil67] H. R. Bilger,
Fano Factor in Germanium at 77K,
Phys. Rev. **163** 238 (1967)

[Blo95] P. M. Bloomfield et al.,
The design and physical characteristics of a small animal positron emission tomograph
Phys. Med. Bio. **40** 1105 (1995)

[Bog00] S.E. Boggs and P. Jean,
Event reconstruction in high resolution Compton telescopes,
Astron. Astrophys. Suppl. Ser. **145** 311 (2000)

[Bos07a] H. C. Boston et al.,
Characterisation of the SmartPET planar Germanium detectors,
Nucl. Instr. and Meth. A **579** 104 (2007)

[Bos07b] H. C. Boston et al.,
Orthogonal strip HPGe planar SmartPET detectors Compton configuration,
Nucl. Instr. and Meth. A **580** 929 (2007)

[Bos07c] A.J. Boston, *oral presentation*,
AGATA: Advanced Gamma Tracking Array,
Gretina Physics Workshop, Richmond Virginia, 2007

[Bru75] N. Bruening, E. Fretwurst and G. Linstroem,
Detailed Investigations on Abnormal Pulse Shapes in Ge(Li)-Detectors
IEEE Trans. Nuc. Sci. **22** 173 (1975)

[Bru06] B. Bruyneel et al.,
Characterization of large volume HPGe detectors Part I: Electron and hole mobility parameterization,
Nucl. Instr. and Meth A **569** 764 (2006)

[Bud08] D. Busdjas, M. Barnabe, O. Chkvorets, S. Schönert, and N. Khanbekov,
Pulse Shape Analysis with a Broad-Energy Germanium Detector for the GERDA experiment,
http://arxiv.org/pdf/0812.1735

[Car66] M. Carona and F. H. Pollak,
Energy-Band Structure of Germanium and Silicon: The k.p Method
Phys. Rev. **142** 530 (1966)

[Cha99] A. F. Chatziioannou et al.,
Performance Evaluation of microPET: A High-Resolution Lutetium Oxyorthosilicate PET Scanner for Animal Imaging
J. Nucl. Med. **40** 1164 (1999)

[Cha01] M. Charlton,
Positron Physics,
Cambridge University Press (2001)

[Cha02] A. F. Chatziioannou,
Molecular imaging of small animals with dedicated PET tomographs,
Eur. J. Nucl. Med **29** 98 (2002)

[Cha04] S. Chauvie et al.,
Geant4 low energy electromagnetic physics,
IEEE Trans. Nucl. Sci. **3** 1881 (2004)

[Che01] S. R. Cherry and S. S. Gambhir,
Use of Positron Emission Tomography in Small Animal Research,
ILAR Journal **42** 219 (2001)

[Chi07] P.W. Chin, N.M.Spyrou,
Monte Carlo investigation of positron annihilation in medical positron emission tomography,
Nucl. Instr. and Meth. A **580** 481 (2007)

[Chi08] M. Chin et al.,
In Search of Exotic Events for PET: A Gammasphere Experiment,
oral contribution, Position Sensitive Detectors 8 (PSD8), University of Glasgow, Glasgow, UK (2008)

[Cho75] Z. H. Cho et al.
Positron Ranges from biomedically important positron-emitting radionuclides
J. Nucl. Med. **16** 1174 (1975)

[Coo07a] R. J. Cooper et al.,
SmartPET: Applying HPGe and pulse shape analysis to small-animal PET,
Nucl. Instr. and Meth. A, **579** 313 (2007)

[Coo07b] R. J. Cooper,
Performance of the SmartPET Positron Emission Tomography System for Small Animal Imaging,
PhD Thesis, University of Liverpool, Liverpool, UK (2007)

[Coo08] R. J. Cooper et al.,
Charge collection performance of a segmented planar high-purity germanium detector,
Nucl. Instr. and Meth. A, **595** 401 (2008)

[Coo09] R. J. Cooper et al.,
Positron Emission Tomography imaging with the SmartPET system,
Nucl. Instr. and Meth. A **606** 523 (2009)

[Dah85] M. Dahlbom et al.,
Hybrid Mercuric Iodide (HgI_2) - Gadolinium Orthoscillate (GSO) Detector for PET
IEEE Trans. Nucl. Sci. **32** 533 (1985)

[Del87] M. A. Deleplanque,
Gammasphere proposal Preprint
LBNL-5202

[Del99] M. A. Deleplanque et al.,
GRETA: utilizing new concepts in γ-ray detection,
Nucl. Instr. Meth. A **430** 292 (1999)

[dDo06] G. Di Domenico et al.,
SiliPET: An ultra-high resolution design of a small animal PET scanner based on stacks of double-sided silicon strip detector,
Nucl. Instr. and Meth. A **571** 22 (2007)

[dGu97] A. Del Guerra et al.,
YAP-PET: a small animal positron emission tomograph based on YAP:Ce finger crystals,
IEEE Nucl. Sci. Symp.**2** 1640 (1997)

[dGu99] A. Del Guerra et al.,
First in vivo studies on rats with YAPPET scanner,
IEEE Nucl. Sci. Symp.-Med. Im. Conf. (1999)

[Der79] S. E. Derenzo, R. R. Hasiguti and K. Fujiwara,
Precision measurement of annihilation point spread distributions for medically important positron emitters,
(Sendai, Japan: The Japan Institute of Metals) 819 (1979)

[Der86a] S. Derenzo,
Mathematical Removal of Positron Range Blurring in High Resolution Tomography,
IEEE, Trans. Nucl. Sci. **33** 565 (1986)

[Der86b] S. Derenzo and T. F. Budinger,
Recent Developments in Positron Emission Tomography (PET) Instrumentation,
SPIE Phys. and Eng. of Comp. Multidimen. Im. and Pro. **61** 232 (1986)

[Dia84] R. M. Diamond and F. S. A. Stephens,
Proposal for the high resolution ball,
LBNL unpublished, (1981)

[DIm00] *Siemens and GE buy into CZT producer Imarad*,
http://www.diagnosticimaging.com
21st June 2000

[Dim08] M. R. Dimmock, *private comunication*

[Dim08b] M. R. Dimmock, *private comunication*

[Dim08] M. R. Dimmock,
Characterisation of AGATA Symmetric Prototype Detectors,
PhD Thesis, University of Liverpool, Liverpool, UK (2008)

[Dir30] P. A. M. Dirac,
A theory of electrons and protons,
Proc. Roy. Soc. Lond. A **126** 360 (1930)

[Doe93] *DOE Fundamentals Handbook: Nuclear Physics and Reactor Theory*,
Volume 1 of 2, U.S. Department of Energy, Washington, D.C. 20585, U.S.A.(1993)

[Dox07] I. Doxas, C. Nieter, D. C. Radford, K. Lagergren, and John R. Cary,
An approximate method for linear signal decomposition in -ray tracking detectors,
Nucl. Instr. and Meth. A **580** 1331 (2007)

[DRU] *http://www.drugs.com/mmx/fludeoxyglucose-f-18.html*

[Eis88] R. Eisner et al.,
Quantitative Analysis of the Tomographic Thallium-201 Myocardial Bullseye Display: Critical Role of Correcting for Patient Motion,
J. Nucl. Med **29** 91 (1988)

[Eva55] R. D. Evans,
The Atomic Nucleus,
McGraw-Hill, New York (1955)

[Ewa64] G. T. Ewan and A. J. Tavendale,
High-Resolution Studies of Gamma-Ray using Lithium-Drift Germanium Gamma-Ray Spectrometers,
Can. J. Phys. **42** 2286 (1984)

[Fan47] U. Fano,
Ionization Yield of Radiations. II. The Fluctuations of the Number of Ions,
Phys. Rev. **72** 1 (1947)

[Far07] M. Farahmand et al.,
Detection of explosive substances by tomographic inspection using neutron and gamma-ray spectroscopy,
Nucl. Instr. and Meth. A **261** 396 (2007)

[Fre62] D. V. Freck & J. Wakefield,
Gamma-Ray Spectrum obtained with a Lithium-drifted p-i-n Junction in Germanium,
Nature **193** 669 (1962)

[Gas78] J. D. Gaskill,
Linear Systems, Fourier Transforms and Optics,
John Wiley & Sons, New York (1978)

[Gar07] P. E. Garrett et al.,
The TRIUMF nuclear structure program and TIGRESS,
Nucl. Instr. and Meth. A **261** 1084 (2007)

[Gat01] E. Gatti et al.,
Spatial localization of multiple simulataneous hits in segmented HPGe detectors: a new algorithm,
Nucl. Instr. and Meth. A **458** 738 (2001)

[Geo94] A. Georgiev, W. Gast and R. M. Lieder,
An Analog-to-Digital Conversion Based on a Moving Window Deconvolution,
IEEE Trans. Nucl. Sci **41** 1116 (1994)

[Gil06] J. Gillam et al.,
Effect of position resolution on LoR discrimination for a dual-head Compton camera,
Nucl. Instr. and Meth. A **573** 76 (2007)

[Gri64] R. Grigorovici et al.,
Band structure and electrical conductivity in previous termamorphous germanium,
Proceedings of the Seventh International Conference on the Physics of Semiconductors, Paris, France, p. 423 (1964)

[Gri09] A. N. Grint,
A semiconductor Compton camera investigation,
PhD Thesis, University of Liverpool, Liverpool, UK (2009)

[Hal52] R. N. Hall et al.,
Electron-Hole Recombination in Germanium,
Phys. Rev. **87** 387 (1952)

[Hal71] R. N. Hall and T. J. Soltys,
High Purity Germanium for Detector Fabrication,
IEEE Trans. on Nucl. Sci., **18** 160 (1971)

[Hal03] C. J. Hall et al.,
A nuclear medicine gamma-ray detector based on germanium strip detector technology,
Nucl. Instr. and Meth. A **513** 47 (2003)

[Han71] W. L. Hansen,
High-Purity Germanium Crystal Growing,
Nucl. Instr. and Meth. **94** 377 (1971)

[Han77] W. L. Hansen & E. E. Haller,
Amorphous Germanium as an Electron or Hole Blocking Contact on High-Purity Germanium Detectors,
IEEE Trans. Nucl. Sci. **24** 61 (1977)

[Har04] M. D. Harpen,
Positronium: Review of symmetry, conserved quantities and decay for the radiological physicist,
Med. Phys. **31** 57 (2004)

[Har09] L. J. Harkness et. al,
Optimisation of a dual head semiconductor Compton camera using Geant4,
Nucl. Instr. and Meth. A *In Press*

[He00] Z. He,

Review of the Shockley-Ramo theorem and its applications in semiconductor gamma-ray detectors,

Nucl. Instr. and Meth. A **463** 250 (2000)

[Hof76] E. J. Hoffman et al.,

Design and performance characteristics of a whole-body positron transaxial tomograph,

J. Nucl. Med. **17** 493 (1976)

[Hof86] E. Hoffman and M. Phelps,

Positron Emission Tomography and Autoradiography: Principls and Application for the Brain and Heart, (1986) 237-286

[Hum02] S. P. Hume and R. Myers,

Dedicated Small Animal Scanners: A New Tool for Drug Development?,

Current Pharmaceutical Design **8** 1497 (2002)

[Ish07] K. Ishii et al.,

First achievement of less than 1 mm FWHM resolution in practical semiconductor animal PET scanner,

Nucl. Instr. and Meth. A **576** 435 (2007)

[JAS] *http://www.spect.com/pub/Flangedjaszczakphantoms.pdf*

[JAV] *http://java.sun.com/*

[Jea99] A. P. Jeavons et al.,

A 3D HIDAC-PET Camera with Sub-millimetre Resolution for Imaging Small Animals,

IEEE Trans. Nucl. Sci. **16** 468 (1999)

[Jen99] R. Jenkins, *X-ray fluoresence spectrometry*, (1999)

[Kac04] K. Kacperski et al.,

Three-gamma annihilation imaging in positron emission tomography,

IEEE Trans. on Med. Im., **23** 525 (2004)

[Kar08] J. S. Karp et al.,
Benefit of Time-of-Flight in PET: Experimental and Clinical Results,
J. of Nucl. Med. **49** 462 (2008)

[Kas02] G. A. Kastis et al.,
Tomographic Small-Animal Imaging Using a High-Resolution Semiconductor Camera,
IEEE Trans. Nucl. Sci. **49** 172 (2002)

[Kha08] A. Khaplanov, B. Cederwall, S. Tashenov,
Position sensitivity of segmented planar HPGe detectors for the DESPEC project at FAIR,
Nucl. Instr. and Meth. A **592** 325 (2008)

[Kle29] O. Klein and Y. Nishina,
Ueber die Streuung von Strahlung durch freie Elektronen nach der neuen relativistischen Quantendynamik von Dirac,
Z. Phys. **52** 853 (1929)

[Kno99] G. Knoll,
Radiation Detection and Measurement, (1999)

[Kro99] R. A. Kroeger et al.,
Charge spreading and position sensitivity in a segmented planar germanium detector,
Nucl. Instr. and Meth. Phys. Res. A **422** 206 (1999)

[Krö96] Th. Kröll et al.,
Analysis of simulated and measured pulse shapes of closed-ended HPGe detectors,
Nucl. Instr. and Meth. A **371** 489 (1996)

[Laz03] I. H. Lazarus et al.,
The GRT4 VME pulse processing card for segmented germanium detectors,
IEEE Nucl. Sci. Symp. **2** 1165 (2003)

[Lee03] I. Y. Lee et al.,
Developments of large gamma-ray detector arrays,
Rep. Prog. Phys. **66** 1095 (2003)

[Lev99] C. S. Levin et al.,
Calculation of the positron range and its effect on the fundamental limit of positron emission tomography system spatial resolution,
Phys. Med. Bio. **44** 781 (1999)

[Lew02] J. S. Lewis et al.,
Small animal imaging: current technologies and perspective for oncological imaging,
Eur. J. of Cancer **38** 2173 (2002)

[Lil01] J. S. Lilley,
Nuclear Physics: Principles and Applications,
J. Wiley and Sons Ltd, (2001)

[Lio93] J. S. Liow and S. C. Strother,
The convergence of object-dependent resolution in maximum likelihood based tomographic resolution,
Phys. Med. Biol. **38** 55 (1993)

[Lop04] A. Lopez-Martens et al.,
γ-ray tracking algorithms: a comparison,
Nucl. Instr. and Meth. **533** 454 (2004)

[Luk95] P. N. Luke,
Unipolar Charge Sensing with Coplanar Electrodes-Application to Semiconductor Detectors,
IEEE Nucl. Sci. **42** 207 (1995)

[LYR] *http://www.lyrtech.com/*

[Mac94] A. O. Macchiavelli et al.
Proc. Conf. on Physics from Large γ-ray Detector Arrays (Berkeley) LBL 35687, CONF 940888 UC413 pp 149-53 (1994)

[Mat06] A. R. Mather,
Evaluation of the Planar Germanium SmartPET system for use in Positron Emission imaging,
PhD Thesis, University of Liverpool, Liverpool, UK (2006)

[Med04] P. Medina et al.,
A simple method for the characterization of HPGe detectors,
IMTC (2004)

[Mih00] L. Mihailescu et al.,
The influence of anisotropic electron drift velocity on the signal shapes of closed-end HPGe detectors,
Nucl. Instr. and Meth. A **447** 350 (2000)

[Mih07] L. Mihailescu et al.,
SPEIR: A Ge Compton camera,
Nucl. Instr. and Meth. A **570** 89 (2007)

[Mil03] L. Milechina and B. Cederwall,
Improvements in γ-ray reconstruction with positive sensitive Ge detectors using the backtracking method,
Nucl. Instr. and Meth. A **508** 394 (2003)

[MIN] *MINUIT Fit Package*,
CERN *http://www.root.cern.ch/root/html/Minuit.html*

[MNT08] *First Semiconductor-Based PET Scanner Demonstrates Potential To Aid In Early Diagnosis Of Disease*,
http://medicalnewstoday.com 19th June 2008

[Mog95] O. E. Mogensen,
Positron Annihilation in Chemistry,
Springer-Verlag Berlin, **58** (1995)

[Mos93] W. W. Moses & S. Derenzo,
Empirical Observation of Resolution Degradation in Positron Emission Tomographs utilizing Block Detectors,
J. Nucl. Med. **34** 101 (1993)

[MTS] *http://ns.ph.liv.ac.uk/software.html*

[Mye02] R. Myers and S. Hume,
Small animal PET,
Euro. Neuropsychopharmacology **12** 545 (2002)

[Nol94] P. J. Nolan et al.,
Large Arrays of Escape-Suppressed Gamma-Ray Detectors,
Annu. Rev. Nucl. Part. Sci. **45** 561 (1994)

[0re49] A. Ore and J. L. Powell,
Three-photon annihilation of an electron-positron pair,
Phys. Rev. **75** 1696 (1949)

[ORT] *http://www.ortec-online.com*

[Osm03] M. M. Osman et al.,
Respiratory motion artifacts on PET emission images obtained using CT attenuation correction on PET-CT,
E. J. of Nucl. Med. and Mol. Im. **30** 603 (2003)

[Pap04] T. Papp, M.-C. Lpy, J. Plagnard, G. Kalinka, E. Papp-Szab,
A new approach to the determination of the Fano factor for semiconductor detectors,
X-Ray Spectrom. **34** 106 (2004)

[Par04] G. Parker,
Introductory Semiconductor Device Physics,
Taylor & Francis First Edition (2004)

[Par05] S. J. Park,
A very high resolution small animal PET based on the Compton PET concept,
Ph.D. Thesis, University of Michigan, USA (2005)

[Par07] S. J. Park,
Performance evaluation of a very high resolution small animal PET imager using silicon scatter detectors,
Phys. Med. Bio. **52** 2807 (2007)

[Par08] *Parker, Motion and Control Technology Company*,
http://www.parker.com/portal/site/PARKER (2008)

[Pau30] W. Pauli,
Offener Brief an die Gruppe der Radioaktiven der Gauvereine-Tegung zu Tübingen (1930)

[Peh68] R. H. Pehl et al.,
Accurate determination of the Ionisation Energy in Semiconductor Detectors,
Nucl. Instr. and Meth. **59** 45 (1968)

[Pel60] E. M. Pell,
Ion Drift in an n-p Junction,
J. Appl. Phys. **31** 291 (1960)

[Phe75] M. E. Phelps et al.,
Effects of positron range on spatial resolution,
J. Nucl. Med. **16** 649 (1975)

[Pod05] *HISPEC/DESPEC Technical Proposal*,
http://www-linux.gsi.de/~wwwnusta/tech_report/09-hispec_despec.pdf

[QIN] *http://reat.space.qinetiq.com/gps/*

[Rad09] D. C. Radford GRETINA Seminar, University of Liverpool, Liverpool, UK (2009)

[Rad17] J. Radon,
On determination of functions by their integral values along certain multiplicites,
Ber. d. Sachische akademie der Wissenschaften Leipzig, (Germany), **69** 262 (1917)

[Ram39] S. Ramo,
Currents Induced by Electron Motion,
Proc. of the Institute of Radio Engineers, **27** 584 (1939)

[Rea01] A. J. Reader et al.,
Regularized One-Pass List-Mode EM Algorithm for High Resolution 3D PET Image Reconstruction into Large Arrays,
IEEE Nucl. Sci. Symp. **4** 1853 (2001)

[Rea07] A.J. Reader,
Image Reconstruction for Positron Emission Tomography,oral contribution,
Mayneord-Phillips Summer School on Molecular Imaging with Positron Emission Tomography (2007)

[Rig06] S. V. Rigby et al.,
Characterisation of Pixellated CdZnTe dectectors for Use in a Portable Gamma-Ray Spectrometer,
IEEE RTSD Conf. Rec. San Diego, USA (2006)

[Rol07] P. Sempre Roldan,
Raytest ClearPET, a new generation small animal PET scanner,
Nucl. Instr. and Meth. A **571** 498 (2007)

[ROO] Root Analysis Package, CERN,
http://www.root.cern.ch/root/doc/RootDoc.html

[Row03] D. J. Rowland, J. S. Lewis and M. J. Welch,
Molecular imaging: The application of small animal positron emission tomography,
J. of. Cell. Bio. **87** 110 (2003)

[San05a] P. Sangsingkeow, *SmartPET Data Sheet*, ORTEC (2005)

[San05b] P. Sangsingkeow, *private communication*, ORTEC (2005)

[Sas07] *The Physics of Medical Imaging: Module 5*,
Course coordinator: S. Sassil (2007)

[Sch78] V. Schönfelder et al.,
Measurement of 1-30 MeV celestial γ-rays with an imaging Compton telescope COMPTEL,
Proposal for a GRO experiment. MPI f. extraterr. Physik, Garching

[Sch99] G. J. Schmid et al.,
A γ-ray tracking algorithm for the GRETA spectrometer,
Nucl. Instr. and Meth. A **430** 69 (1999)

[Sch03] K. P. Schäfers,
Imaging small animals with positron emission tomography,
Nuklearmedizin **42** 86 (2003)

[She82] L. A. Shepp and Y. Vardi,
Maximum Likelihood Reconstruction for Emission Tomography,
IEEE Trans. Med. Imag. MI-1 2 (1982)

[Sho38] W. Shockley,
Currents to Conductors Introduced by a Moving Point Charge,
J. Appl. Phys. **9** 635 (1938)

[Sho50] W. Shockley,
Energy Band Structures in Semicondcutors,
Phys. Rev. **78** (1950) 173

[Sho52] W. Shockley and W. T. Read,
Statistics of Recombination of Holes and Electrons,
Phys. Rev. **87** 835 (1952)

[Sim49] J. H. Simpson,
Charge distribution and energy levels of trapped electrons in ionic solids,
Proc. R. Soc. Lond. 197 **1049** 269 (1949)

[Sim97] J. Simpson,
The Euroball Spectrometer,
Z. Phys. A **358** 139 (1997)

[Sim03] J. Simpson and R. Krücken,
AGATA:The advanced gamma tracking array,
Nuclear Physics News **13** 15 (2003)

[Sim06] J. Simpson,
The AGATA project,
J. Phys. **41** 72 (2006)

[Sin83] M. Singh,
An electronically collimated gamma camera for single photon emission computed tomography. Part I: Theoretical considerations and design criteria,
Med. Phys. **10** 421 (1983)

[Ste83] E. G. Steward,
Fourier Optics: An Introduction,
Ellis Horwood Physics Series (1983)

[Sze02] S. M. Sze,
Semiconductor Devices Physics and Technology,
John Wiley & Sons, 2nd Edition, (2002)

[Tai05] Y.-C. Tai and R. Laforest,
Instrumentation Aspects of Animal PET,
Ann. Rev. of BioMed. Eng. **7** 255 (2005)

[Tak05] T. Takahashi et al,
Application of CdTe for NeXT emission,
Nucl. Instr. and Meth. A **541** 332 (2005)

[Tar03] G. Tarantola et al.,
PET Instrumentation and Reconstruction Algorithms in Whole-Body Applications,
J. of Nucl. Med. **44** 756 (2003)

[Tav63] A. J. Tavendale and G. T. Ewan,
A high-resolution lithium-drifted Germanium Gamma-Ray Spectrometer,
Nucl. Instr. and Meth. **25** 185 (1963)

[Tea50] G. K. Teal & J. B. Little,
Growth of germanium single crystals,
Phys. Rev. C. **78** 647 (1950)

[Tod74] R. W. Todd, J. M. Nightingale & D. B. Everett,
A proposed γ camera,
Nature **251** 132 (1974)

[Tur06] G. H. B. Turk,
The characterisation of the first SmartPET HPGe planar detector,
PhD Thesis, University of Liverpool, Liverpool, UK (2006)

[Twi81] P. Twin,
Workshop on Nuclear Structure at High Spin,
(Risø, Denmark) 135 *unpublished*

[vdM99] J. van der Marel and B. Cederwall,
Backtracking as a way to reconstruct Compton scattered γ-rays,
Nucl. Instr and Meth. A **437** 538 (1999)

[vdM02] J. van der Marel and B. Cederwall,
γ tracking in germanium: the backtracking method,
Nucl. Instr. and Meth. A **477** 391 (2002)

[Ven04] R. Venturelli and D. Bazacco,
Adaptive Grid Search as Pulse Shape Analysis Algorithm for -Tracking and Results,
LNL Annual Report (2004)

[Vet00] K. Vetter et al.,
Three-dimensional position sensitivsity in two-dimensionally segmented HP-Ge detectors,
Nucl. Instr. and Meth. A **452** 223 (2000)

[Vet04] K. Vetter, M. Burks and L. Mihailescu,
Gamma-ray imaging with position-sensitive HPGe detectors,
Nucl. Instr. and Meth. A **525** 322 (2004)

[Vin08] R. Vinke et al.,
Optimizing timing resolution for TOF PET detectors based on monolithic scintillation crystals using fast photosensor arrays,
IEEE Nucl. Sci. Symp. 3954 (2008)

[Wat97] M. Watanabe,
A high resolution animal PET scanner using compact PS-PMT detectors,
IEEE Trans. Nucl. Sci. **44** 1277 (1997)

[Wat06] S. Watanabe,
Development of CdTe pixel detectors for Compton cameras,
Nucl. Instr. and Meth. A **567** 150 (2006)

[Wan06] Y. Wang et al.,
Performance Evaluation of the GE Healthcare eXplore VISTA Dual-Ring Small-Animal PET Scanner,
J. of Nucl. Med. **47** 1891 (2006)

[Web98] S. Webb,
The Physics of Medical Imaging,
Taylor & Francis (1998)

[Web99] S. Weber et al.,
Evaluation of the TierPET system,
IEEE Trans. Nucl. Sci. **46** 1177 (1999)

[Web04] , S. Weber and A. Bauer,
Small animal PET: aspects of perfromance assessment,
Euro. Jour. of Nucl. Med. and Mol. Im. **31** 1545 (2004)

[Yan01] Y. F. Yang et al.,
A Compton camera for multitracer imaging,
IEEE Trans. Nucl. Sci. **48** 656 (2001)